Figures and Text Withheld Under 10 CFR 2.390

Chapter 1 General Information

1-1 Revise the drawings of the transfer cask to show:

a. Either section A-A and associated material dimensions, whose slice is shown on Drawing No,, 10494-72-19, or specify the location of section A-A on another drawing,

b. The thickness of the resin in the bottom of the transfer cask,

c. The thickness of the radial neutron shield and the stainless steel enclosing the water,

Section A-A is needed in order to be able to determine the thickness of lead shield. Additionally, the dimensions of the resin material in the bottom of the transfer cask as well as the neutron shield thickness and steel casing are not specified in the drawings.

Response:
Drawing 10494-72-19 and 10494-72-21 have been revised to show the requested information. The nominal lead thickness is 3.60", the resin thickness in the cask bottom is 1.25", the radial neutron shield (water) is 5.06" thick and reduces to 4.56" thick at the transition from 1.50" to 2.00" thickness of the structural shell. The stainless steel enclosure is 3/16" thick.

1-2 Clarify Drawing No. 10494-72-19, which appears to show lead shielding in the base of the transfer cask instead of the borated resin material, The application does not indicate that lead is contained in the transfer cask anywhere else except as radial shielding.

Response:
Drawing 10494-72-19 has been revised to correctly show resin material in the base of the transfer cask.

1-3 Revise the application to provide a material specification for the Vyal B resin material in the DSC.

Response:
The Vyal B resin material is being replaced by a borated polyester resin which is installed in the bottom and top of the transfer cask, not the DSC. The polyester resin is the same resin material utilized in the Transnuclear TN-40, TN-32 and TN-68 dry storage casks. It is a proprietary material consisting of mainly polyester resin, styrene, aluminum hydrate and zinc borate. The composition is shown below. SAR Tables 5-17 and 5-18 will be revised to show the composition of the borated polyester resin.

Borated Polyester Resin

Element	% wt
H	5
B	1
C	35
O	42
Al	15
Zn	2
TN Resin Density = 1.58 g/cm^3	

1-4 Revised Table 1-1 to indicate the name(s) and the technical specifications to indicate the name of the Metal Matrix Composites to be used for criticality control.

Response:
The metal matrix composites (MMCs) are specified in Chapter 9, which is intended to be consistent with the ASTM committee C26 work item WK936. There are no specific intended trade names. Table 1-1 will be revised to reference the materials specification in Chapter 9.

1-5 In Drawing Nos. 10494-72-1 and 10494-72-15, justify the use of Non Code,(i.e.., commercial grade) material for the many components of the DSC and TC.

The specification for the plates, bolts, and pipes is shown in the PART LIST but the material is Non Code.

Response:
The column Code Classification on the drawings refers to the ASME Code. For the DSC (10494-72-1), components that are not part of the containment, i.e. washers, siphon and vent components, spacers and shielding, are classified as "non-code". Also, aluminum plates used in the basket are not "code" materials and are procured under ASTM material specifications.

The transfer cask (10494-72-15) is not used as a containment vessel because the DSC is the containment. However, the ASME code, Section III, Subsection NC is used for main body assembly. Components that are not part of the body assembly or do not provide a confinement function for the cask cavity are designated as "non-code" and in many cases are procured under an ASTM material specification.

1-6 Editorial: Drawing No 10494-72-10, it appears that Section U - U should have been Section Y-Y,
Drawing No. 10494-72-19, Section AA - AA is not shown on the drawing,
Section 1.1 - should be OS187H TC, not OS817H.

Response:

The appropriate page and drawings will be corrected in the revised SAR.

Chapter 2 Principal Design Criteria

2-1 Justify the assumption for calculating the maximum internal pressure in the NUHOMS 32PTH DSC, that 1 % of the fuel rods are damaged for normal conditions and up to 10% of the fuel rods are damaged for off-normal conditions.

Conservatively, the basis for calculating the maximum internal pressure of the DSC should be based on 32 intact assemblies.

Response:
Consistent with NUREG 1536, 1% and 10% of all the fuel rods (32 assemblies) are assumed failed for normal and off-normal conditions, respectively. In accordance with NUREG 1536, the maximum internal pressure is calculated, in Section 4.6, by including the released gas from the damaged fuel rods into the DSC.

2-2 Revise Section 2.1.1 to provide a definition(s) of damage fuel that is consistent with the guidance in Interim Staff Guidance -1, Revision 1 (ISG-1, rev 1),

In accordance with 10 CFR 72.236(c), the spent fuel must be maintained subcritical under credible conditions. Further, 10 CFR 72.236(m) seeks to ensure safe fuel storage and handling and to minimize post-operational safety problems with respect to retrievability of the fuel from the storage system.

Response:

The definition of damaged fuel in Section 2.1.1 is actually a subset of the damaged fuel defined in ISG-1, Rev 1. At this time, Transnuclear is only requesting to store "damaged fuel" so defined which has been evaluated to remain subcritical under credible conditions and can be handled with respect to retrievability. Transnuclear is not requesting approval for storage of damaged fuel assemblies which can not be handled using normal (i.e. crane and grapple) handling methods. The third paragraph in SAR Section 2.1.1 will be revised as follows:

The 32PTH DSC can accommodate up to 16 damaged fuel assemblies which include assemblies with missing or partial fuel rods, or fuel rods with known or suspected cladding defects greater than hairline cracks or pinhole leaks. The extent of the damage is to be limited such that a fuel pellet is not able to pass through the damaged cladding during handling and retrievability is assured following normal and off-normal conditions. Damaged fuel assemblies shall be placed into the sixteen inner most basket fuel compartments, as shown in Figure 2-2, which contain top and bottom end caps that confine any loose material and gross fuel particles to a known, sub-critical volume during normal, off-normal and accident conditions and to facilitate handling and retrievability. Reactor records, visual/videotape records, fuel sipping, ultrasonic examination, and radio chemistry are examples of techniques utilized by utilities to identify damaged fuel.

2-3 Revise the table in Chapter 2, entitled, "Minimum ^{10}B areal density" to include the volume percent of boron carbide in all of the neutron absorbers.

The high loadings of boron carbide in the aluminum may cause the absorbers to become brittle, similar to a ceramic, and thus, affect the durability of the Metal Matrix Composites (MMCs) neutron absorber.

Response:
The requested data will be provided in Table 9-1, and referenced in a footnote to the table in Chapter 2.

2.4 Revise Section 2.1.2 (and Chapter 4, Thermal) to state that the number of thermal cycles that the cladding experiences is less than 10,

Thermal cycling (repeated heatup/cooldown cycles) can enhance the amount of hydrogen that eventually re-precipitates in the form of radial hydrides, The extent of the formation of radial hydrides is dependent on many factors including the maximum temperature, change in temperature, number of thermal cycles, applied stress, hydrogen concentration, and solubility of hydrogen in the material. As stated in ISG-1 1, Rev. 3, the formation of radial hydrides in spent fuel cladding can be minimized by restricting the change in cladding temperatures to less than 65°C and minimizing the number of cycles to less than 10.

Response:
Page 2-2 will be revised to limit the number of thermal cycles to less than 10. SAR page 4-34 states that the drying procedures preclude any thermal cycling.

2-5 **Editorial: Verify the statement on page 2-9, Section 2.2.9, "Ambient Variations (including solar insulation)."**

It appears that the bullet should read "Ambient Variations (including solar insolation)."

Response:

Page 2-9 will be revised to show "solar insolation".

Chapter 3 Structural Evaluation

3-1 The 32PTH DSC stability criteria (I e., allowable buckling loads) stated in Section 3.1.2.1.2 are not acceptable. Revise the application to calculate the critical loads for buckling of the DSC shell and the basket structure. The buckling evaluation should consider elastic, plastic, and local buckling, if applicable. Reasonable safety factors for the allowable buckling loads should be provided to take into account material and geometrical imperfections.

The application stated that: "The acceptance criteria (allowable buckling loads) are taken from ASME Code, Section III, Appendix F, paragraphs F-1341.3, Collapse Load." Buckling is a stability consideration. Collapse load evaluation for a given combination of loads on a given structure is to ensure the strains or deflections of the structure are acceptable for load carrying purposes. Thus, collapse load evaluation is a strength consideration and cannot be used to substitute a buckling evaluation.

Response:

The critical loads for buckling of the DSC shell, basket, and transfer cask shell were recalculated using ANSYS finite element Nonlinear Buckling Analysis. This technique employs a nonlinear static analysis with gradually increased loads to seek the load level at which the structure becomes unstable. In a nonlinear analysis, the model can include features such as plastic material behavior, gaps and large-deflection response.

The material nonlinearities and gaps were included in the above structural buckling analyses. In addition, the large displacement option (geometric nonlinearities) of ANSYS [3-1] is also used in all the analyses. This option will use deflections at each load step to continuously update the geometry of the structure, thus producing a revised stiffness matrix. The ANSYS automatic time stepping program option "Autots" was activated. This option lets the program decide the actual size of the load-substep for a converged solution. The program stops at the load substep when it fails to result in a converged solution. The last load step with a converged solution is the buckling load for the structures. Chapter 3, Section 3.1.2.1.2 will be revised to reflect this change.

Canister Shell Buckling Analysis

The following three hypothetical accident load cases for the canister are considered in this buckling analysis.

Buckling Load Case 1: Corner drop + 15 psig external pressure

Buckling Load Case 2: Corner drop + 0 psig internal pressure

Buckling Load Case 3: Corner drop + 30 psig internal pressure

The two-dimensional axisymmetric finite element model of the canister described in Appendix 3.9.1, Section 3.9.1.3.2.D.2 (page 3.9.1-39) for the DSC canister stress analysis is used for this analysis. The gap element real constants, node couplings and displacement boundary conditions are also the same as those used in Section

3.9.1.3.2.D.2 (page 3.9.1-39). The weight of canister's outer top cover plus the top shield plug and its support ring is 12,847 lb, and the bottom shield plug is 9,420 lb (Chapter 3, page 3-14). Since the top end of the canister is heavier than the bottom end, it is a more severe case when the canister drops on its bottom end. A drop on the bottom end is therefore chosen for analysis in this calculation.

For storage application, the end drop is not a creditable event. The transfer cask is transferred in a horizontal position held by the transfer trailer. In the axial direction it is possible to slide into the ground and incur a corner drop. The maximum corner drop g load calculated by the LS-DYNA including dynamic load factor as described in Appendix 3.9.11 is 21 g (page 3.9.11-6). For conservatism, 75g end drop is used for canister buckling analysis.

For load case with external pressure or internal pressure, a quasi-static plastic analysis consisting of two load steps is performed to monitor the buckling of canister. The first load step applies external pressure or internal pressure alone. A subsequent inertial load of 300*g* is added in the second load step. The outer surface of the canister bottom is held in order to simulate the case that the canister drops on a rigid cask bottom face.

In the load step 1, the stepped external or internal pressure is applied as a static load.

In the load step 2, the weight of the canister internals (basket and fuel assemblies) is accounted for by applying an equivalent internal pressure on the canister bottom. The actual total weight of the canister internals is 80,574 lb (basket 29,854 lb + fuel assemblies 50,720 lb) (Chapter 3, page 3-14). A total weight of 81,500 lb for the canister internals is conservatively used in this analysis. This inertial load is uniformly distributed over the bottom surface of the canister cavity with a radius of 34.375 in. This equivalent uniform pressure, P_{in}, exerted on the canister bottom by the weight of the internals under a 1*g* load is calculated as follows.

$$P_{in} = [81{,}500 / (\pi \times 34.375^2)] = 21.954 \text{ psi.}$$

An equivalent pressure of 6586.2 psig on the canister bottom corresponding to the 300*g* load (P_{in} = 300 × 21.954 = 6586.2psi) is therefore applied to the canister bottom along with the 300*g* acceleration load in the load step 2.

A stress-strain relationship (with kinematic hardening) is used to obtain stresses and deflections beyond the elastic limit of the material. The large displacement option in ANSYS is activated to monitor the buckling response.

The following table summarizes the last converged load for the two load cases:

Load Case	Last Converged Load (g)	G load calculated From Appendix 3.9.11 Analysis (page 3.9.11-6)	G Load Used For Basket Structural Analysis	Factor of Safety
1	175	21	75	2.33
2	176	21	75	2.35
3	177	21	75	2.36

Appendix 3.9.1.3.3 DSC buckling evaluation was revised to reflect this analysis.

Basket Buckling Analysis

The detail of basket buckling analysis is described in the response to the question 3-4 of RAI.

Transfer Cask Buckling Analysis

The detail of transfer cask buckling analysis is described in the response to the question 3-5 of RAI.

3-2 Provide the basis and justification for applicability of the temperature dependent material properties shown in Table 3-6 and Table 3-7

The maximum temperature of the HSM-H concrete surface exceeds the temperature limits in the ACI 349, A.4.2. The temperature dependent material properties of the HSM-H concrete are provided in Tables 3-6 and 3-7. Provide relevant information or the pages of the references to show applicability to the HSM-H concrete.

Response:

The basis for temperature dependent material properties shown in Table 3-6 and Table 3-7 of Chapter 3 are taken from reference [3-26].

As reported in Table 3-6, a reduction of 10% is taken in the 28 day concrete compressive at a temperature of 500°F. This 10% reduction bounds test data for concrete compressive strength versus temperature for various concrete types provided in Figure 7-7of reference [3-27, page 216]. Similarly, the concrete modulus of elasticity and the coefficient of thermal expansion are taken from reference [3-27, pages 216 and 156, respectively].

The maximum concrete temperature of 364°F obtained from the thermal analysis of the HSM-H stored with a 32PTH DSC is bounded by the maximum concrete temperature used for the design of the HSM-H as reported in reference [3-26]. As reported in Reference [3-26], the concrete compressive strength is verified by testing for temperatures exceeding 350°F.

The reinforcing steel material properties reported in Table 3-7 are based on Figures 7-3 and 7-5 of reference [3-27, pages 216]. These figures show the range of yield strengths and modulus of elasticity of structural grade steel at high temperatures, which the reference indicates may be used for reinforcing bars. For ASTM A615, Grade 60

reinforcing steel, the yield strength and modulus of elasticity at 100°F are 60 ksi and 29000 ksi, respectively. The yield strength and modulus of elasticity of the reinforcing steel at high temperatures are obtained from these initial values and the reduction of the initial values with temperature from the curves shown in Figures 7-3 and 7-5 of Reference [3-27], respectively.

The concrete properties at temperatures will be qualified by testing (see response to RAI 12-5).

3-3 Justify in Appendix 3.9,1, Table 3.9.1-7, why the allowable stress intensities for the end closure welds were based on the material tensile stress, when the end closure welds are partial penetration welds and the allowable stresses should be based on the material shearing stresses. In addition, on page 3.9.1-55, Lifting Block Weld Stresses, allowable stresses appear to be based on the material yield stresses when it should be revised to be based on the shearing stresses.

Response:

A. Canister Structural Analysis

The allowable stresses table shown on Table 3.9.1-7 of Appendix 3.9.1 are based on Subsection NB [3-3] and are used to compare with the calculated maximum stress intensities. The allowable shear stresses at the closure welds based on Subsection NB and Appendix F [3-4] are listed in the following table and are used to compare with the calculated maximum shear stresses.

ASME Code Allowable for Weld Stresses (304 SS 500°F)

Loading Condition	Stress Type	Stress Limits	Allowable Stress (ksi)
Normal	Shear	$(0.6\ S_m)^{(1)} \times 0.7^{(3)}$	$(0.6 \times 17.5) \times 0.7 = 7.35$
Accident	Shear	$(0.42 S_u)^{(2)} \times 0.7^{(3)}$	$(0.42 \times 63.4) \times 0.7 = 18.64^{(4)}$ $(0.42 \times 59.2) \times 0.7 = 17.4^{(5)}$

Notes:
1. Shear allowable from Subsection NB, NB-3227.2 [3-3].
2. Shear allowable from Appendix F, F-1341.2 [3-4].
3. The allowables were reduced (x 0.7) to include the quality factor from Code Case N-595-3 [3-5] based on PT or MT of root and final layers.
4. For SA-240, Type 304
5. For SA-182, F304

Loading Conditions

The canister structural analyses are described in Appendix 3.9.1, Section 3.9.1.3 (page 3.9.1-36). The canister end closure welds are included in the ANSYS [3-1] finite element models and described in Appendix 3.9.1, Section 3.9.1.3.2 (pages 3.9.1-39 and 40). These finite element models are shown on Figure 3.9.1-17 for 2-D Axisymmetrical Canister Model and Figure 3.9.1-19 for 3-D model.

A total of of 24 transfer load cases (Appendix 3.9.1, Section D.3, page 3.9.1-43) and 8 storage load cases (Appendix 3.9.1, Section E.3, page 3.9.1-58) are analyzed using these two models. The maximum stress intensity for these analyzed load cases are reported in Appendix 3.9.1, Tables 3.9.1-11 to 3.9.1-35.

The most critical shear stress at the end clousure welds for these analyzed load cases occurs for the 75g side drop + 30 psi internal pressure and the 75g side drop + 15 psi external pressure cases. The ANSYS result files for these two load cases are postprocessed to get the maximum shear stresses at the canister end closure weld locations. These shear stresses are compared with the above ASME code shear stress criteria.

The weld stresses at outer top cover and inner top cover plates are summarized and compared with code allowables in the following table.

Summary of Weld Shear Stresses and Allowables

Weld	Load	Stress Type	Maximum Stress (ksi)	Allowable (ksi)	Factor of Safety
Between Outer Top Cover and Shell	75g Side Drop + 30 psig Internal Pressure	Shear	13.78	18.64	1.35
	75g Side Drop +15 psig External Pressure	Shear	13.68	18.64	1.36
Between Inner Top Cover and Shell	75g Side Drop + 30 psig Internal	Shear	13.30	17.4	1.31
	75g Side Drop +15 psig External Pressure	Shear	13.38	17.4	1.30

B. Canister Corner Drop Analysis

The canister corner drop load case is analyzed as follows.

- Finite Element Model

The 3D canister finite element model as described in Appendix 3.9.1, Section 3.9.1.3.2, page 3.9.1-40) is used for calculating the canister corner drop. The finite element model is shown on Figure 3-1.

- Loading and Boundary Conditions

The transfer cask cavity length is 186.6" and the canister length is 185.75". The gap between the inside surface of the transfe cask lid and outer surface of the canister outer top cover is 0.85". For storage the end drop is not a creditable event. The transfer cask is transferred in a horizontal position held by the transfer trailer. In the axial direction it is possible to slide into the ground and incur a corner drop. During the corner drop, the canister is supported by the cask body in the horizontal position and the top end of the canister will slide into the cask lid and supported by the lid. However, for weld shear stress calculation it is conservatively assumed that the internal weight (basket + fuel assemblies) will impact the inner surface of the canister inner top cover without any support from transfer cask lid.

The maximum axial G load calculated from LS-DYNA [3-2] as described in Appendices 3.9.10 and 3.9.11 is 21 g (Appendix 3.9.11, page 3.9.11-6). For conservatism an axial g load of 22g is used for the analysis.

This inertial load is uniformly distributed over the inner surface of the canister inner top cover with a radius of 34.375 in. This equivalent uniform pressure, P_{in}, exerted on the canister inner top cover by the weight of the internals under a 22g load is calculated as follows.

$$P_{in} = [(81{,}500 \times 22) / (\pi \times 34.375^2)] = 483 \text{ psi.}$$

The canister internal pressure of 30 psi is also added to the above calculated 22g inertial pressure, therefore the total pressure used for the analysis is 513 psi.

The loading and boundary condition plots are shown on Figures 3-2 and 3-3, respectively. This boundary condition shows that all the internal loads impact to the inner surface of the canister inner top cover without any support from the transfer cask lid.

- Analysis Results

The results of the analyses are summarized in the following tables.

Summary of Weld Shear Stresses and Allowables

Load Case	Weld	Stress Type	Maximum Stress (ksi)	Allowable (ksi)	Factor of Safety
Canister Corner Drop + 30 psi Internal Pressure	Between Outer Top Cover and Shell	Shear	9.60	18.64	1.94
	Between Inner Top Cover and Shell	Shear	9.66	17.4	1.80

Summary of DSC Component Maximum Stress Intensities and Allowables

Load Case	Component	Stress Type	Calculated Max. Stress Intensity (Ksi)	Allowable Membrance Stress Intensity (Ksi)[1]	Factor of Safety
Canister Corner Drop + 30 psi Internal Pressure	Canister Shell	$P_L + P_b$	20.46	44.38	2.17
	Canister Ourt Top Cover	$P_L + P_b$	16.39	44.38	2.71
	Canister Inner Top Cover	$P_L + P_b$	15.83	41.44	2.62

Note:
1. Allowable stresses are taken from Appendix 3.9.1, Table 3.9.1-7. Since the calculated maximum membrane plus bending stress intensity ($P_L + P_b$) is less than the allowable membrane stress intensity (P_m), therefore only maximum membrane plus bending stress intensity ($P_L + P_b$) is reported.

The ANSYS maximum stress intensity plots for canister shell, canister outer top cover, and canister inner top cover are shown on Figures 3-4, 3-5 and 3-6, respectively.

C. Lifting Block Weld Stresses

The lifting blocks are used to lift the empty canister into the transfer cask and is a non critical lift. ANSI N14.6 [3-6] is used as a guide for evaluation of the canister lifting blocks. It requires that the combined shear stress or maximum tensile stress at any point in the device shall not exceed the material minimum tensile yield strength and the material ultimate tensile strength for 6*g* and 10*g* lifting loads, respectively (ANSI N14.6 Section 4.2.1.1-1993). Since the ultimate tensile strength of the canister and its lifting block material exceeds 10/6 of their minimum tensile yield strength (i.e. $S_u / S_y > 10/6$), the 6*g* lifting load is the critical load for stress evaluation.

The same Section of ANSI N14.6 also states that the shear stress shall be taken as an average value over the cross section. Therefore, the maximum shear stress at the lifting block weld is calculated in Appendix 3.9.1 (page 3.9.1-55) by dividing the total load over the weld throat area and is compared with the material tensile yield stress.

3-4 The collapse load approach to evaluate buckling loads of 32PTH DSC fuel basket plates and support rails is not acceptable (See Chapter 3, RAI 1). Given the fact that the fuel basket plate supports are fusion welded to the stainless steel fuel compartments, it is not clear why a small three-dimensional ANSYS finite element model is needed to calculate the buckling load., (Section 3..7.1,1 2) In addition, the drawing shows the basket plates are aluminum (B209) not SA-240 Type 304 stainless steel. However, the application stated that a buckling analysis of the full size basket was conducted for a 45degree azimuth basket orientation drop (Page 3.9.1-29).. The inelastic finite element analysis converged up to a load of 86,,4g. The design g-load is 75g and thus the safety factor is approximately 86.4g/75g=1.15. Please justify that this small safety factor is adequate to

prevent buckling of the basket components during a 75g side drop of the transfer cask. Confirm that the buckling analysis was preformed based on the correct materials and material properties.

Response:

Methodology

As stated in RAI 3-1 the critical loads for basket buckling are recalculated by using ANSYS Nonlinear Buckling Analysis.

Geometry

The details of the 32PTH DSC basket are shown in drawings 10494-72-8 through 10494-72-12 on Chapter 1, Section 1.5. The 32PTH DSC basket is a welded assembly of thirty-two continuous stainless steel fuel compartment boxes (8.7" x 8.7" x 162" length, see Figure 3-7, item 1). These stainless steel fuel compartments are fusion welded to Type 304 stainless steel basket plates (item 3 in Figure 3-7 and Figure 3-8). The fusion welds are spaced intermittently along the box sections (total of 2,816 fusion welds are used for the 32PTH basket assembly) . Neutron poison plates, composed of a boron-aluminum alloy (or a boron carbide aluminum metal matrix composite), are sandwiched between the sections of the stainless steel walls of the adjacent boxes and the adjacent stainless steel plates (Figure 3-7, items 4 & 5). Figure 3-9 of this RAI shows the stainless steel fuel compartment assembly and Figure 3-10 of this RAI shows the fuel compartments with sandwiched boron aluminum alloy plates. The Type 304 stainless steel members are the primary structural components. The neutron poison plates provide criticality control and a heat conduction path from the fuel assemblies to the canister shell.

Stainless steel rails are oriented parallel to the axis of the canister and attached to the periphery of the basket to establish and maintain basket orientation and to support the basket. Figure 3-11 of this RAI shows the entire basket assembly with stainless rail.

Finite Element model

ANSYS 3D basket models used for stress analyses as described in Appendix 3.9.1.2.3 (page 3.9.1-7) are used for computing the buckling loads.

Material Nonlinearities

The basket fuel compartments, structural plates, peripheral rails and canister shell are constructed from SA-240, type 304 stainless steel. A bilinear stress-strain relationship, with kinematic hardening, was used for each component to simulate a correct nonlinear material behavior at the maximum operating temperature.

Geometric Nonlinearities

Since the structure experiences large deformations before buckling, the large displacement option of ANSYS is used for all the analyses.

Loadings

The basket is analyzed for 0°, 30°, and 45° side drop loads. The weight of boron-aluminum alloy plate is distributed on all four sides of stainless steel boxes, and the fuel assembly weights are distributed on the top panel of the SST-ALUM-SST sandwich for the 0° side drop load orientation and proportionally distributed on the top & side panels for the 30° and 45° side drop load orientations.

Maximum load of 120g was applied in 0° drop and 100g in 30° and 45° drop analyses. The ANSYS automatic time stepping program option "Autots" was activated. This option lets the program decide the optimal size of the load-substep for a converged solution. The program will stop at the load substep which fails to result in a converged solution. The last load step with a converged solution is the buckling load for the structure.

Result

The following table summarizes the last converged load for all three load cases:

Basket Drop Orientation	Last Converged Load (g)	G load calculated From Appendix 3.9.11 (page 3.9.11-6)	G Load Used For Basket Structural Evaluation	Factor of Safety
0°	110	64	75	1.47
30°	95	64	75	1.27
45°	99	64	75	1.32

In this analysis the calculated buckling load in 45° drop orientation is higher than the g load calculated in the SAR-Rev. 0 (86.4g) is due to the following reasons:

1. The g load calculated in SAR is based on all material properties at a uniform temperature of 612°F. The new analysis is based on true temperature distribution (canister at 500°F, basket rail at 550°F, basket compartment from 600°F at peripheral and 700°F at center).

2. The total fuel assembly weight of 1585 lb divided by the active fuel length of 144" (actual basket length is 162") is conservatively used in the SAR. The weight of active fuel length is recalculated to be 1,460 lb. The new anslyses are based on the 1,460 lb divided by the active fuel length.

The ANSYS displacement plots for the last converged load steps for the 0°, 30°, and 45° drop orientations are shown on Figures 3-12, 3-13, and 3-14, respectively.

These results are conservative because the ½" aluminum plates sandwiched between the fuel compartments are not included in the model while their weight are accounted in the analyses. The ½ " thick aluminum plate would provide additional safety margin if they were included in the analyses.

Appendix 3.9.1, Section 3.9.1.2.4 basket buckling analysis is revised to incorporate this new analysis.

3-5 Provide justification for a concurrent 30 psig internal pressure in the evaluation of the structural adequacy of the OS187H Transfer Cask inner shell with respect to buckling.

Section 3..7.3,4, Transfer Cask Inner Containment Buckling Analysis, stated that: the loads considered for buckling analysis includes an internal pressure of 30 psig and a 75g top and bottom drop load in both hot (115 F) and cold (-20 F) ambient environments, The Tech Spec only specifies a helium backfill pressure of 2 ±1.0 psig, Resolve the discrepancy and evaluate the effects of internal pressure on buckling loads for the shell.

Response:

The transfer cask inner shell buckling analyses were rerun using the same finite element model as described in Chapter 3, Section 3.7.3.4 (page 3-51) and Appendix 3.9.4, Section 3.9.4.3 (page 3.9.4-6). The following loadings are considered in the analyses.

1. Top end drop with lateral pressure of lead in hot ambient (115°F)
2. Bottom end drop with lateral pressure of lead in hot ambient (115°F)

ANSYS nonlinear buckling analysis was performed. Maximum loads of 200g were applied in all load cases. The automatic time stepping program option "Autots" was activated. This option lets the program decide the actual size of the load-substep for a converged solution. The program stops at the load substep when it fails to result in a converged solution. The last load step, with a converged solution, is the buckling load for the structure.

The following table summarizes the last converged load for all two load cases:

Load Cases	Last Converged Load (g)	G load calculated From Appendix 3.9.10 LS-DYNA CG Over Corner Analysis(1)	G Load Used For Cask Structural Evaluation	Factor of Safety
Top End Drop (Hot)	189	15.5	75	2.52
Bottom End Drop (Hot)	178	15.5	75	2.37

Note:

1. For storage the end drop is not a creditable event. The transfer cask is transferred in the horizontal position held by the transfer trailer. In the axial direction it is possible to slide into the ground and incur a corner drop. The maximum corner drop g load calculated by the LS-DYNA as described in Appendix 3.9.10 is 15.5g. For conservatism 75g is used for inner shell buckling analysis.

The ANSYS displacement plots for the last converged load steps for the above two load cases are shown on Figures 3-15 and 3-16, respectively.

The lateral pressure of the lead vs. g load at a typical location in the middle section of the cask during the top and bottom end drops are shown in Figures 3-17 and 3-18, respectively. These figures show that the pressure load increases as the g load increases.

Chapter 3, Section 3.7.3.4 and Appendix 3.9.4 will be revised to incorporate these new analyses.

3-6 The OS187H transfer cask impact analysis presented in Appendix 3.9.7 is based on the Reference: "Structural Design of Concrete Storage Pads for Spent Fuel Casks," EPRI Np-7551. NRC has not endorsed the EPRI report and the analysis results (e.g., g-loads and damages to the cask) may be unacceptable.. The transfer cask dynamic impact analysis should be revised and performed using an approach such as the nonlinear finite element code DYNA3D on a cask-pad-soil finite element model as described in NUREG/CR-6608., Note that the g-loads probably will be different as the result of the revised evaluation and the cask closure bolt analysis will have to be redone.

Response:

The cask impact analysis was redone using the LS-DYNA program following the same methodology from LLNL reports NUREG/CR-6608 [3-7] and UCRL-ID-126295 [3-25]. The detail analysis and results are included in Appendix 3.9.10.

3-7 Perform a top end corner drop dynamic impact structural analysis of the transfer' cask to show the adequacies of the top inner shell weld to the top forging.

The inner shell is attached to the top flange (forging) by fillet welds (Drawing No, 10494-72-19)., It is unclear whether the welds have adequate strength to prevent separation of the inner shell from the top flange for a top end corner drop of the transfer cask.

Response:

The inner shell is full penetration welded to the transfer cask bottom plate (see TN drawing 10494-72-19, right side of inner shell assembly view) and also full penetration welded to the transfer cask top flange (left side of the inner shell assembly view). In addition to the full penetration welded to the flange a fillet weld is added to the joint. An enlarge detail of this weld is shown on Figure 3-19 for information. Both weld symbols are called out on the drawing.

As stated in RAI 3-1, for storage application (Part 72) [3-8], the transfer cask is transferred in a horizontal position held by the transfer trailer. In the axial direction it is possible to slide into the ground and incur a corner drop. The maximum axial g load calculated by the LS-DYNA as described in Appendix 3.9.10 is 15.5g.

Since the top end vertical drop will induce much higher stress than the top end corner drop at this weld location, therefore a 75g top end drop is conservatively used to calculate the weld stresses. This load case has been analyzed in Appendix 3.9.2, Load Case # 8 (page 3.9.2-25). The maximum stress intensities for different components are

reported in Table 3.9.2-1. The ANSYS result file from this load case is post processed to get the maximum shear stress at this weld location.

The maximum shear stress is 5,034 psi

The allowable shear stress is 0.42 S_u, for 304 SS at 400°F,

$\tau_w = 0.42\ S_u = 0.42 \times 64{,}000 = 26{,}880$ psi

Factor of safety = 26,880/5,034 = 5.34

Appendix 3.9.2, Section 3.9.2.2.4 Load Case #8 (page 3.9.2-25) will be revised to include this analysis.

3-8 Perform structural analysis to demonstrate the canister rails (3.0 inches wide and 0. 12 inches thick) are adequately strong to support the DSC canister without significant deflections,

The canister rails are supported by the cask inner shell which is in turn supported by chemical lead shield, Appendix 3.9.2, page 3.9.2-19, stated that: " Pressures applied in the radial direction in the 3-dimensional finite element model are based on cosine distributions These pressure distributions simulate the internal cask contents applying pressure to the inner cask wall." This pressure distribution may not be conservative for the canister rails because the applied loads are rather concentrated and the lead backed inner shell may not have sufficient stiffness to prevent significant deflection of the rails along the length of the cask.

Response:

The 3D finite element model used for side drop analyses as described in Appendix 3.9.2, Section 3.9.2.2.3B (page 3.9.2-13) was modified as follows and used to calculate the stresses and deflections of the transfer cask inner shell along the support rail locations.

Finite Element Model Modifications

1. Including the 3" wide x 0.12 thick rails (SHELL 43 element) in the 3D transfer cask inner shell.
2. Including canister shell (SOLID 45 element) in the 3D model.
3. Gap element (CONTACT 52) is used between the canister shell and transfer cask inner shell and between the canister shell and cask inner shell rail.

Radial gap elements (CONTACT 52) are used to simulate the interface between the outer radius of the canister and inner radius of the cask inner shell. Each gap element contains two nodes; one on each surface of the structure. The gap size at each gap element is determined by the difference between the canister outer radius and the inside radius of the cask (canister outer radius = 34.875" and cask inner radius = 35.25" to give a 0.375 inch mean gap). Radial gap elements are generated using an ANSYS macro. Actual gap sizes for the gap element, at each radial location, were determined and input into the model as real constants using another ANSYS macro. This macro accepts the drop orientation and model geometry as inputs and determines the circumferential

position of each gap element. The macro then computes the real constants and applies to appropriate gap elements.

During drops on cask rails (180° side drop), the initial gaps between the canister and the cask are modified using the ANSYS macro. Two 3 inch wide and 0.12 inch thick rails are welded to the cask inner shell at 12° on both sides of the vertical center line of the model and another set of two rails are welded at 38° on both sides of the same vertical center line. For the 180° side drop onto the rails, the initial gaps at the two inner rail locations are assumed closed (0 gap). In-between these two rail locations, the initial gaps are set to 0.12 inches. On the other two rail locations, the gaps are initially set open all gap sizes are generated by macro with consideration of the rail thickness.

The ANSYS 3D finite elememt models including cask shell, lead, rails, canister, and gap elememts are shown on Figures 3-20 to 3-24.

Loadings

Pressures applied in the radial direction to the inner surface of the canister in the 3-dimensional finite element model are based on a cosine distribution. This pressure distribution simulates the load which the internal canister contents exert on the inner canister wall. Two drop orientations are analyzed.

1. The canister initial impacts on two rails (168° and 192°). See Figure 3-25.
2. The canister initial impacts on one rail (168°). See Figure 3-26.

Materials

In order to properly calculate the deflections of the rails, elastic and inelastic material properties of the canister and cask, at temperatures, are used for the analysis.

Results

The following table summarizes the maximum stress intensities at the transfer cask inner and outer shells for the above two drop load cases.

Summary of Maximum Stress Intensities and Allowables

Load Case	Component	Stress Category	Calculated Max. Stress Intensity (Ksi)	Allowable Membrance Stress Intensity (Ksi)[1]	Factor of Safety
Impact on Two Rails	Inner Shell	$P_L + P_b$	40.35	44.8	1.11
	Outer Shell	$P_L + P_b$	37.54	46.34	1.23
Impact on One Rail	Inner Shell	$P_L + P_b$	36.11	44.8	1.24
	Outer Shell	$P_L + P_b$	38.41	46.34	1.21

Note:

1. Allowable stresses are taken from Appendix 3.9.2, Section 3.9.2.2, page 3.9.2-8. Since the calculated maximum membrane plus bending stress intensity ($P_L + P_b$) is less than the allowable membrane stress intensity (P_m), therefore only maximum membrane plus bending stress intensity ($P_L + P_b$) is reported.

All the calculated stresses are less than the code allowables and the maximum calculated rail deflection is 0.02", this deflection is small and will not affect the retrieving of the canister from the transfer cask after an accident drop.

The maximum stress intensity plots of the cask inner shell and outer shell for the impact to the two rails load case are shown on Figures 3-27 and 3-28, respectively. The maximum stress intensity plots of the inner shell and outer shell for the impact to the one rail load case are shown on Figures 3-29 and 3-30, respectively.

Appendix 3.9.2, Section 3.9.2.5 was added to include this new analysis.

3-9 Section 3.7.3.4, revise the buckling analysis of the transfer cask inner shell by including the lateral pressure of the lead on the inner shell in an end drop impact condition.,

The lateral pressure of the lead on the inner shell is significant at the impacted end and thus must be considered for the shell buckling analysis.

Response: See response in RAI 3-5.

3-10 Justify the handling loads used for the structural analysis of the transfer cask trunnions (e.g., DW+0.5g axial+0.5g transverse+0.5g vertical, Appendix 3.9.5, page 3.9.5.1).,

The handling loads for the transfer cask trunnions should include the loads during TRANSFER OPERATIONS. Provide the references for the loads assumed in analysis.

Response:

The cask Transfer Operations and handling loads described in Appendix 3.9.5.1.B were developed to envelope all possible events that are postulated to occur during the DSC loading, draining, drying and sealing operations, and movement of a loaded cask onto the transfer trailer and insertion of the DSC into an HSM.

Handling loads associated with the vertical lifting of the cask and down-ending onto the trailer prior to transfer to the ISFSI are enveloped by the 6 and 10 g vertical analyses performed for a cask weight of 250,000 lbs shown in Sections 3.9.5.2, 3.9.5.3 and 3.9.5.6.1.

As listed in 3.9.5.1.B four separate Transfer Operations load cases are postulated. These were developed considering the maximum capabilities of the transfer equipment and ensuring that the design load cases enveloped each case as follows:

1. DW (dead weight) +/- 1g Axial – This load combination considers the maximum acceleration and braking capability of the tractor vehicle and trailer at the

maximum permitted speed of 5 mph. This would result in a longitudinal load of significantly less than 1g. Therefore; a design basis load of dead weight +/-1g longitudinally will envelope the maximum straight line handling experienced by the transfer cask and DSC.

2. DW +/- 1g Transverse (lateral) - During transit of the loaded cask from fuel building to ISFSI the cask will have to negotiate a number of corners. The extreme load enveloping this case is to assume a transverse acceleration of +/- 1g combined with the loaded cask dead weight. Based upon the 10'-6" width of the transfer trailer and a cask cg of 8'-0" a transverse acceleration of 0.66g (= 5.25/8) would overturn the rig. Therefore; a handling load of DW +/- 1g is a conservative envelop for this condition.

3. DW +/- 1g vertical – This is an unrealistically high estimate to cover the case of the transfer trailer running over a very large pothole. A drop of this magnitude is not possible as it would require a vertical discontinuity in the road surface and for the whole trailer to traverse the drop before any of the wheel sets react to the surface profile. Given the design of the hydraulic trailers used where each wheel set is designed to follow the road profile this load case will easily envelop anything that could reasonably happen during the transfer.

4. DW +/- 1/2g Axial +/- 1/2g Transverse +/- 1/2g Vertical – This load case was generated to evaluate the system for simultaneous application of loads in all 3 directions and to provide assurance that the system had been evaluated for a seismic event should such occur during the transfer from fuel building to ISFSI.

5. Transfer of a DSC from Cask to HSM – for this case the HSM cask restraint is used to tie the upper trunnions to the front face of the HSM. The maximum load postulated to occur in each restraint is ½ the maximum ram load or 55,000 lbs on each trunnion as described in Appendix 3.9.1, Section 3.9.1.3 (Load case #23, page 3.9.1-53). This is enveloped by the handling load analysis described above.

3-11 Appendix 3.9.8, page 3.9.8-1, stated that: "Damaged fuel assemblies may be only stored in the peripheral compartments of the NUHOMS 32PTH DSC." However, Chapter 2, page 2-1, stated that: "Damaged fuel assemblies shall be placed into the sixteen inner most basket fuel compartments, as shown in Figure 2-2, which , Resolve the apparent contradiction,. Also, the temperatures effects should be considered on the allowable stresses of the cladding.

Response:

The damaged fuel assemblies shall be placed into the sixteen inner most basket fuel compartments, as shown on Chapter 2, Figure 2-2. The typo on Appendix 3.9.8, page 3.9.8-1 has been corrected.

The maximum fuel cladding temperature during the transfer condition based on the above assumption has been calculated in Chapter 4, and the results are listed in Table 4-1. Based on results shown in this table, the maximum fuel cladding temperature is 723°F. The allowable stress of the fuel cladding for the drop load is taken at 725°F (see

response to RAI 3-17).

3-12 Justify that the maximum g-load acting on the damaged fuel rod subjected to 1 foot end drop is 30g

The basis for the 30g end drop g-load is not clear. If this is the design basis loading considered for the NUHOMS HD System, please clearly state it in the SAR

Response:

The handling loads for the damaged fuel inside the DSC in the Part 72 (storage) application during the transfer operation are as follows:

DW (Dead Weight) + 1g Axial
DW + 1g Transverse
DW + 1g Vertical
DW + ½*g* Axial + ½*g* Transverse + ½*g* Vertical

Since the 32PTH DSC is also intended to be used for off-site transportation, the Part 71 [3-9] normal transportation loads are therefore considered here for damaged fuel structural analysis. During the off-site transportation, the transport cask is attached with impact limiters at both ends.

The transport cask and impact limiters for 32PTH DSC have not been designed yet. However, similar package such as NUHOMS-MP197 Multi-Purpose Cask [3-10] with impact limiters has been designed and licensed for transporting NUHOMS-61BT canister. The maximum g load for one foot drop is about 10g.

The 30g is not a design basis load for PART 72 application. It is conservatively used to bound the PART 72 handling loads for damaged fuel cladding structural evaluation and also to bound the future Part 71 normal transport loads.

3-13 Justify the fuel rod moment of inertia (MI) used for the side drop fuel rod structural integrity evaluation. The fuel rod moment of inertia has been assumed to be equal to the net tube MI plus net fuel MI.

The application stated that: "Where it is conservatively assumed that the net tube MI is equal to one half of the total tube MI, and the net fuel MI is equal to one half of the total fuel MI The basis to include fuel MI in the stress calculation is not conservative and subject to challenge. Please provide the justification for the assumption.

Response:

Typical cladding and fuel pellet dimensions as a function of exposure [3-11] are shown on Figure 3-31 of this RAI for information. This figure shows that during operation, the cladding ID will gradually reduce and touch the pellet OD during operation cycle 2 (ID of cladding = OD of pellet = 0.3245"). In starting cycle 3, the pellet and clad ID will expand as a unified piece through the remaining cycle life (OD of pellet = 0.3248").

The radial Interference between ID of cladding and OD of pellet at end of cycle life is calculated as follows.

Cladding inside radius during cycle 2 = 0.3245"/2 = 0.16225"
Pellet outside radius at end of cycle 3 = 0.3248"/2 = 0.16240"

Radial Interference = (0.16225"- 0.16240") = - 0.00015"

Inorder to visualize the magnitute of the contact forces between cladding and pellets, the contact pressure between the ID of cladding and OD of the pellet due to this interference is calculated using the formula of [3-12, page 59]. This calculation assumes same E for cladding and pellets.

Pressure = P = $(E\ \delta/b)\ [(b^2-a^2)\ (c^2-b^2)]/\ [(2b^2)\ (c^2-a^2)]$

Where

a = pellet inside radius at end of life cycle = 0
b = pellet outside radius at end of life cycle = 0.1624"
c = cladding outside radius at end of life cycle = 0.1822"
δ = -0.00015"
E = Young's Modulus of cladding (725°F) = 10.6×10^6 psi

$P = (10.6 \times 10^6 \times 0.00015/0.1624)\ [(0.1624^2-0^2)\ (0.1822^2-0.1624^2)]/\ [(2x0.1624^2)\ (0.1822^2-0^2)]$ = 1,006 psi

With this kind of pressure bond between the ID of cladding and OD of the pellets, the cladding and pellets will act together as a solid rod. In the damaged fuel side drop analysis, a simplified hand calculation using classic formula of MC/I is used for maximum bending stress calculation. The moment of inertia (I) used for calculating the bending stress is assumed as follows:

$$I = \tfrac{1}{2}\ (I_{tube} + I_{pellet})$$

A 3D finite element model of tube cladding and pellets is constructed to simulate this bounding effect between the tube cladding and fuel pellets and to compute cladding stresses to bench mark the simplified hand calculation.

Approach

i) An ANSYS finite element model of one span (between two support grids of WE 17 x 17 OFA) is created to simulate an interaction effect of cladding and pellets in a fuel rod. Only a half-length span is modeled due to symmetry.

ii) The suitability of cladding boundary conditions for the above model is verified by computing stresses in cladding tube model (without pellets and gap elements) and comparing the results with hand calculated stresses.

iii) The stresses from combined cladding and pellet model are compared to the hand calculated stresses in cladding as a beam with summed moment of inertia for cladding and pellets.

Finite Element Model

ANSYS element Shell63 is used to model the cladding tube (Figure 3-32). The cladding tube outer diameter and wall thickness are 0.3573" and 0.0198, respectively. The tube model is constructed of 6,600 elements of Shell63. ANSYS element Solid45 is used to simulate the fuel pellets. The pellet size is 0.3088" OD and 0.4629" length. A total of 27 full and one half pellets are modeled. Each pellet consists of 1,200 Solid45 elements and thus 33,000 solid elements for the entire model. All the fuel pellets are connected together with axial CONTACT 52 elements with zero gaps. Figure 3-33 shows the pellet model. The pellet and cladding are connected together by radial CONTACT 52 elements with interference gaps shown in Figure 3-34. The radial interference is calculated to be 0.00015" based on the data shown in Figure 3-31. However, a much smaller interference value of 0.00002" is conservatively used in radial gap real constants.

Material properties (at 725 °F)

a) Fuel Cladding (Zircalloy)

Young's Modulus, $E = 10.6 \times 10^6$ psi [3-13]
Yield Strength, $S_y = 69{,}500$ psi (see response in RAI 3-17)
Poisson Ratio, $\upsilon = 0.3$
Density[(1)] = 0.234 lb/in^3 x 0.8464 = 0.198 lb/in^3

b) Fuel Pellets (UO_2)

Young's Modulus, $E = 27.8 \times 10^6$ psi [3-14]
Poisson Ratio, $\upsilon = 0.316$
Density[(1)] = 0.384 lb/in^3 x 0.8464 = 0.325 lb/in^3

Note:
1. Densities are modified to take into account the actual end conditions of a fuel rod span as a continuous beam (Maximum Bending Moment = 0.1058 wL^2) [3-13, page 23]. Since the ANSYS model is simply supported (Maximum Beam Bending Moment = 0.125 wL^2), its densities are modified by a factor of 0.1058/0.125 = 0.8464 to match the maximum bending moment in the actual continuously supported cladding tube.

Boundary Conditions

The fuel cladding is modeled as a simply supported shell at two ends. Symmetry boundary conditions are applied at right end. The shell model is supported at two (diametrically opposite) nodes in X direction and two nodes in Y direction at its left end. The pellet is supported at two nodes in Z direction in such a way that their rotation is not constrained. These boundary conditions are shown in Figure 3-35.

Structural Analysis of Cladding Model - Boundary Condition Verification

The suitability of shell boundary conditions is validated by applying the above boundary conditions to the cladding shell model only (pellet is not included) (Figure 3-36) and

making an ANSYS run for 5g (arbitrary) acceleration. The resulting bending stress (SZ) distribution in shell is shown in Figure 3-37. The maximum shell bending stress (1,017 psi) is compared to the following hand computed beam stress:

Maximum Beam Bending Moment (for uniformly distributed load), $M = 0.125wL^2$

Weight /unit length, $w = \pi/4\ (0.3573^2 - 0.3177^2) \times 1.0 \times 0.198 = 0.0041568$ lb/in

Span, L= 25.46 in.

$M = 0.125 \times 0.0041568 \times 25.46^2 = 0.3368$ in. lb.

Moment of inertia, $I = \pi/64\ (0.3573^4 - 0.3177^4) = 0.0002999$ in^4

Max. Bending Stress (for 5 g)
$= \pm 5MC/I$
$= \pm (5 \times 0.3368 \times 0.3573/2)/ (0.0002999) = \pm 1{,}003$ psi $\approx$ 1,017 psi (from computer run)

Beam stresses are very close to the shell model stresses, hence shell model and boundary conditions are validated.

Structual Analysis of Combined Cladding and Pellets Model

A nonlinear structural analysis of the fuel cladding and the pellet model (combined cladding and pellets) is conducted for a 5g vertical load. The maximum load is applied as acceleration in Y direction in small sub-steps. The automatic time stepping program option "Autots" is activated. This option lets the program decide the actual size of the sub-step load for a converged solution. Displacement, Stresses and Forces at each node of model (for each converged sub step load) are written on ANSYS result files.

The axial stress (SZ) distribution in cladding is shown in Figure 3-38. It is seen that maximum tensile stress of 1,923 psi occurs near the tube center (at symmetry boundary condition end). Local maximum stress occurs at the tube bottom due to small gap opening between the pellets. At cladding top, the gaps between the pellets remain closed and the maxim compressive stress (-513 psi) is much lower than the bottom tensile stress.

Damaged Fuel Hand Computed Stress Comparison with Computer Stresses

In Appendix 3.9.8, Section 3.9.8.11 (page 3.9.8-18) the damaged fuel cladding stress is computed using the following assumption.

$I_{\text{used for stress calculation}} = \frac{1}{2}\ (I_{\text{tube}} + I_{\text{pellet}})$

Maximum Beam Bending Moment (for uniformly distributed load), $M = 0.125wL^2$

(Cladding + Pellet) weight,

$w = (\pi/4)\ (0.3573^2 - 0.3177^2) \times 1.0$ in. $\times 0.234 \times 0.8464$ (factor for continuous support beam) + $(\pi/4)\ (0.3088^2) \times 1.0$ in. $\times 0.384 \times 0.8464$ (factor for continuous support beam) = 0.028497 lb/in

Span, L = 25.46 in.

$M = 0.125wL^2 = 0.125 \times 0.028497 \times 25.46^2 = 2.309$ in. lb.
(½)(Cladding + Pellet) moment of inertia,

$I = (½)\ [\pi/64\ (0.3573^4 - 0.3177^4) + \pi/64\ (0.3088^4)] = 0.00037\ in^4$

Max. Bending Stress (for 5 g) = ± 5MC/I = ± 5 (2.309 x 0.3573/2)/0.00037 = ± 5,574 psi

This hand computed beam maximum stress (5,574 psi) with half of summed moment of inertias is 289% (5574/1923= 2.89) of the computer composite model of cladding and pellets maximum stress (1,923 psi).

Conclusions

The results of analysis indicate that the methodology of evaluating structural integrity of damaged fuel cladding by using half of the summed moment of inertia of cladding and pellets is reasonable and conservative (with 2.89 factor of conservatism).

The maximum stress calculated from cladding and pellets composite model (1,923 psi) is much lower (less than half) than the hand calculated stress [5,574 psi using ½ (I_{tube} + I_{pellet})]. This is because the pellet material ($E = 27.8 \times 10^6$ psi) has higher stiffness than that of cladding material ($E = 10.6 \times 10^6$ psi). The interference forces between cladding and pellets result in a stiffer composite structure than a zircalloy homogeneous structure. The hand calculation is based on a zircalloy homogeneous structure.

This fact is also verified by a computer run of model by using same E (of cladding) for the cladding and pellet materials. The resulted stresses (2,613 psi) are higher than those in above composite model (with actual E of cladding and actual E of pellets in the model) and are shown in Figure 3-39.

3-14 Describe the controls during LOADING OPERATIONS and TRANSFER OPERATIONS, such that the fuel rods will either accelerate from 0 initial velocity to a maximum velocity of 5 MPH, or decelerate from a maximum velocity of 5 MPH to 0 final velocity.

Under normal conditions, the structural integrity of the fuel assemblies is calculated based on the kinetic energy of the mass and the velocity.. It is thus important to ensure the maximum velocity of the fuel assemblies does not exceed the 5 MPH limits as assumed.

Response:

During loading operations the movement of fuel assembly is either by the fuel handling bridge or within the cask. The bridge is already limited in travel speeds as part of the Part 50 [3-15] license, and integrity of the fuel is maintained, as the same methods used during refueling outages are used to load the canister. Once the fuel is placed in the canister, the movement of the canister is controlled by the movement of the transfer cask. The lift speeds for moving the cask (typically a heavy lift, within the plant procedures) limit the travel speeds to less than 5 mph. Crane travel speeds are typically 5-15 FPM (ft per minute), which is far less than 5 mph (more than 400 ft per minute).

During Transfer operations, the transfer trailer speed shall be less than 5 MPH when loaded with fuel assemblies. The transfer trailer speed is dictated by operating procedures.

3-15 Demonstrate that the Vyal B resin used in the transfer cask is non-reactive with cask internal components and will remain adherent when exposed to the various environments during loading operations, The manufacturer's data/specification should be submitted to support your argument.

Response:

The resin material is not exposed to the environment. It is completely enclosed by stainless steel both in the cask lid and the cask bottom. Note that the cask lid is not placed into the spent fuel pool.

3-16 Provide a brittle fracture analysis to evaluate the fracture toughness of the transfer cask bolts,

The statement concerning brittle fracture is not a concern because all the components comprising the transfer cask are all stainless steel, is not a true statement. As stated in 3.1.1.3 of the SAR, non-stainless steel members include the carbon steel closure bolts. The SAR does not have any supporting analysis or evaluation to demonstrate that these bolts will not fracture while in-service.

Response:

The transfer cask and its attachment bolts are designed and fabricated per ASME Subsection NC Code [3-16]. The fracture toughness requirements for the bolting material are specified in Section NC-2332.3. This section indicates that in order to meet the fracture toughness requirements, a Charpy V-notch test shall be performed. The test shall be performed at or below the Lowest Service Metal Temperature, and all three specimens shall meet the requirements of Table NC-2332.3-1. The size of lid bolt is 1.5" diameter, based on Table NC-2332.3-1 the required C_v value is 25 mils (lateral expansions).

In addition to the above Charpy V-notch test, a brittle fracture evaluation is performed to demonstrate that the brittle fracture is not a concern for the lid bolts.

The lid bolts are fabricated from SA-540 Gr. B24 Cl. 1 and have the following material properties:

Material Grade	Yield Strength, ksi (Room Temperature)	Ultimate Tensile Strength, ksi (Room Temperature)
SA-540 Gr. B24 Cl. 1	150	165

In accordance with the ASME Code, Section II, Part A [3-17], the bar stocks of these materials are quenched and fully tempered (1000 – 1100°F or higher) to produce a strong and tough microstructure.

ASM Metal Handbook (Volume 1) [3-18], Figure 26 (reproduced here in Figure 3-40) shows that a 4340 steel tempered at 1035°F for 1 ½ hours to produce a yield strength of 158 ksi exhibits a very low Charpy impact transition temperature (< -20°F) and an upper shelf energy of about 45 ft-lbs at –20°F.

Figure 31 (reproduced here in Figure 3-41) shows that a medium carbon low alloy steel tempered to a yield strength of 107 ksi (like SA-197, Grade B7) would have an upper shelf energy of about 52 ft-lbs and absorb about 48 ft-lbs at –20°F while material at a yield strength of 149 ksi (like SA-540 Gr. B24 Cl. 1) would have an upper shelf energy of 35 ft-lbs and absorb about 30 ft-lbs at –20°F.

The following table summarizes the equivalent impact energy of the SA-540 Gr. B24 Cl. 1 at –20°F and the Charpy values used for the brittle fracture evaluation performed as part of this submittal.

Material Grade	Yield Strength (ksi)	Charpy Value, -20°F (Ft-lbs)	Charpy Value Used for Brittle Fracture Evaluation (Ft-lbs)
4340 Steel Tempered at 1035°F for 1 ½ Hours (Fig. 3-40)	158	45	
Medium-Carbon Low Alloy (Fig. 3-41)	149	30	
SA-540 Gr. B24 Cl. 1	150		20**

** By comparaison with the similar yield strength materials, lower values are conservatively used for SA-540 Gr. B24 Cl.1 brittle fracture evaluations.

Brittle fracture evaluations of the lid bolt is performed based on a service temperature of –20°F. The work includes the following:

- Methodology
- Stress
- Material fracture toughness
- Fracture toughness criteria
- Allowable flaw calculations
- NDE Inspection Plan

Methodology

The allowable flaw size is calculated using the Singular Integral Equation and Asymptotic Approximation [3-19] (see Figure 3-42). The total applied stress intensity $K_{applied}$ is calculated based on the following equations.

$\sigma = P/(\pi a^2)$

$K_{applied} = \sigma (\pi a)^{1/2} F_1(a/b)$ (see Figure 3-42 for definitions)

Stress

The maximum tensile stress for the lid bolt is 106.6 ksi and is calculated in Appendix 3.9.3 Section 3.9.3.5 (page 3.9.3-13).

Material Fracture Toughness

The Charpy impact value may be transformed into a fracture toughness value by using the empirical relation developed in Section 4.2 of NUREG/CR-1815 [3-20] as follows:

$K_{id} = [5E(C_v)]^{1/2}$

Where

K_{id} = Dynamic Fracture Toughness, psi -$(in)^{1/2}$
E = Modulus of Elasticity, 26.7×10^6 psi
C_v = Charpy Impact Value, 20 ft-lbs

Substituting the values given above,

$K_{id} = [5E(C_v)]^{1/2} = [5 \times 26.7 \times 10^6 (20)]^{1/2} = 51{,}672$ psi-$in^{1/2}$

Fracture Toughness Criteria

Using the method described in the ASME Code, Section XI, IWB-3613 [3-21], the limiting fracture toughness values are reduced by a factor of $\sqrt{2}$ for the accident condition and are calculated as follows:

$K_{allowable} \leq 51{,}672/\sqrt{2} = 36.54$ ksi-$\sqrt{in}$

Allowable Flaw Size Calculation

Using the above load definitions, fracture toughness values and assumed flaw size (0.0625"), the total applied stress intensity K_1 (applied) is calculated based on the Singular Integral Equation and Asymptotic Approximation (see Figure 3-42).

$K_{applied} = \sigma (\pi a)^{1/2} F_1(a/b) = 15.74 (\pi \times 0.125)^{1/2} (0.5) = 4.93$ ksi--$\sqrt{in} \leq 36.54$ ksi-$\sqrt{in}$

NDE Inspection Plan

The results of the fracture toughness analysis show that the flaws in the attachment bolts which would result in unstable crack growth or brittle fracture are larger than those generally observed in the bolt and bar stock.

The allowable flaw size for the attachment bolts and tie rods is 0.0625 in. In addition to the visual inspection, A PT or MT will be performed to ensure that defects of the maximum flaw sizes calculated are detected and repaired prior to use.

The liquid penetrant or magnetic particle method will be used in accordance with Section V, Article 6 of ASME Code [3-22].

3-17 Provide correct irradiated material properties; in particular, the ultimate strength, yield strength, and oxide thickness used for the fuel rod integrity during drop scenario at 750°F. Additionally, show that they are bounding for the irradiated fuel type chosen for the analysis. Further, clarify if an extrapolation was done to obtain the mechanical properties at 750°F, and if so, provide the calculations to obtain the mechanical properties.

The staff has reviewed a data-base of properties, EPRI reports, and technical papers that do not agree with the properties used for the applicant's inputs for the structural analysis on rod integrity in Section 3.5.3. Furthermore, the estimate of the cladding corrosion and corresponding wall thinning computed should be approximately a wall thinning of -120/1.76 =-77 microns, using a conservative value for the pilling-bedworth ratio. Based on data, the 77 microns could be low for high burnup Zircaloy-4 fuel cladding that has absorbed up to 600 ppm (total hydrogen content) of hydrogen during reactor operation. The properties in Section 3.5.3 appear to be acceptable for low burnup fuel, but not for high burnup fuel cladding

In accordance with 10 CFR 72.236(c), the configuration of the spent fuel geometry should be maintained to assure subcriticality under all credible normal and design basis events of storage. Further, 10 CFR 72.236(m) seeks to ensure safe fuel storage and handling and to minimize post-operational safety problems with respect to retrievability of the fuel from the storage system.

Response:

The material strength properties for cladding of low burnup and high burnup fuels are described as below:

Material property for low burnup fuel

The material properties used for the fuel cladding structural analysis are based on the LLNL report "Dynamic Impact Effects on Spent Fuel Assemblies" [3-13] and are for low burnup fuel. The material properties used for the drop analysis at elevated temperature are obtained from the following methodology.

Yield Strength of cladding: The yield stress vs. temperature is taken from Table 5 of [3-13, page 12] and is depicted in Figure 3-43. Since the relation between the yield strength vs. temperature is linear, the yield strength at higher temperature is obtained by extending the curve.

S_y = 81,500 psi (725°F)
S_y = 80,500 psi (750°F)

Tensile Strength of cladding: The tensile strength corresponding to the yield strength at the temperatures is obtained from Figure 5 of [3-13, page 17] and is also depicted in

Figure 3-43.

S_u = 92,000 psi (725°F)
S_u = 91,800 psi (750°F)

Material property for high burnup fuel

The following material properties for high burnup fuel are obtained from EPRI technical report "Hot Cell Examination of ZIRLO PWR Fuel, Irradiated to 70 GWG/MTU" [3-23].

Hot Cell Oxide Thickness: The oxide thickness, hydrogen concentration, and burnup are obtained from Table 3-1 of [3-23, page 3-1] and are listed in the following table.

Overall Hot Cell Results Summary

Gamma Scan Burnup GWd/MTU	70.3	68.3	72.9	70.9	72.6	71.3	71.0	70.3
Hot Cell Max Average Oxide Thick, μm	54	71	62	66	71	60	63	44
Maxi. Hydrogen Concentration, ppm	569		976			585		

Based on the results shown on this table, the expected oxide thicknesses are in the range of 44-71 micrometers for the high burnup fuel. In the SAR, Chapter 3, Section 3.5.3, the fuel cladding thickness is based on an oxide thickness of 120 micrometers. This assumption is considered to be conservative.

In order to calculate the actual thickness of the cladding needed to be reduced, the oxide thickness accumulation needed to be corrected. A Pilling-Bedworth factor of 1.75 [3-24, page 426] is used in Chapter 3 calculation and is repeated as follows.

$(120/1.75) \times 10^{-6} \times 39.372 = 0.0027$ in.

Yield and Tensile Strength: The test data for the yield and tensile strengths are summarized in Table 3-9 of the EPRI report [3-23, page 3-31]. The tests are performed at 25°C (77°F) and 350°C (662°F). The test data are copied and listed in the following tables. For conservatism, only test data with oxide thickness equal to or greater than 42 micrometers are listed.

Test Data of Yield and Tensile Strengths - 350°C (662°F)

Oxide Thickness (μm)	Test Temperature	Yield Strength (psi)	Tensile Strength (psi)
45	350°C (662°F)	519 MPA (75,282)	583 MPA (84,566)
60	350°C (662°F)	541 MPA (78,474)	629 MPA (91,238)
42	350°C (662°F)	536 MPA (77,748)	614 MPA (89,062)
53	350°C (662°F)	495 MPA (71,801)	581 MPA (84,276)
Average		75,826	87,285

Test Data of Yield and Tensile Strengths - 25°C (77°F)

Oxide Thickness (μm)	Test Temperature	Yield Strength (psi)	Tensile Strength (psi)
48	25°C (77°F)	846 MPA (122,715)	945 MPA (137,075)
61	25°C (77°F)	798 MPA (115,752)	889 MPA (128,952)
Average		119,234	133,013

Since the relations of the yield and tensile strength vs. temperatures are linear (see Figure 3-43 of low burnup fuel), therefore the above calculated average yield and tensile strengths at 25°C (77°F) and 350°C (662°F) are used to develop the strength vs. temperature curves. In the laboratory strength test, the test results will be affected by a lot of factors, such as size of test specimen, specimen selection, instrument calibration, etc.. Therefore it is reasonable to utilize average test strength because it is a representative of the data. These two curves are depicted in Figure 3-44. The values at higher temperatures are obtained by extending the curves.

S_y = 69,500 psi (725°F)
S_y = 67,500 psi (750°F)

S_u = 81,000 psi (725°F)
S_u = 79,000 psi (750°F)

The maximum fuel cladding temperature is calculated to be 723°F during the cask transfer operation (Chapter 4, Table 4-1). Therefore, the cladding material strength properties at temperature of 725°F will be used for structural integrity evaluations. It may be pointed out that the calculated cladding stresses reported in the SAR are all below the above yield strength of 69,500 psi.

Chapter 3, Section 3.5.3 and Appendix 3.9.8 are revised to incorporate these high

burnup material properties.

3-18 Verify the statement in Tables 3.9.2-2 to 3.9.2-7 which reads "Allplied Loads,." It appears that the heading should read "Applied Loads."

Response:

The typo in Appendix 3.9.2, Tables 3.9.2-2 to 7 has been corrected.

References

3-1 ANSYS User's Manual, Rev 6.0.

3-2 LS-DYNA3D User's Manual (Nonlinear Dymamic of Structures in Three Dimensions) Livermore Software Technology Corporation. August 1, 1995, Version 936.

3-3 American Society of Mechanical Engineers, ASME Boiler and Pressure Vessel Code, Section III, Division 1, Subsection NB, 1998, including 2000 Addendum.

3-4 American Society of Mechanical Engineers, ASME Boiler and Pressure Vessel Code, Section III, Appendix F, 1998 with 2000 Addenda.

3-5 ASME B&PV Code Case N-595-3 "Requirements for Spent Fuel Storage Canisters Section III, Division 1"

3-6 American National Standard ANSI N14.6 – 1993, "American National Standard for Radioactive Materials – Special Lifting Devices for Shipping Containers Weighing 10000 pounds (4500 kg) or More"

3-7 NUREG/CR-6608 "Summary and Evaluation of Low-Velocity Impact Tests of Solid Steel Billet Onto Concrete Pads", Lawrence Livermore National Laboratory, February 1998.

3-8 U.S. Government, "Licensing Requirements for the Storage of Spent Fuel in an Independent Spent Fuel Storage Installation (ISFSI)," Title 10 Code of Federal Regulations, Part 72, Office of the Federal Register, Washington, D.C.

3-9 U.S. Government, "Packaging and Transportation of Radioactive Material" Title 10 Code of Federal Regulations, Part 71, Office of the Federal Register, Washington, D.C.

3-10 NUHOMS-MP197 Packaging Safety Analysis Report.

3-11 North Anna Power Station UFSAR, rev. 40, 12/30/04.

3-12 John F. Harvey "Theory and Design of Modern Pressure Vessels" Second Edition.

3-13 UCID-21246 "Dynamic Impact Effects on Spent Fuel Assemblies" October 20,1987.

3-14 NUREG/CR-0497 "A Handbook of Materials Properties for Use in the analysis of Light Water Reactor Fuel Rod Behavior, MATPRO-Version 11". February 1979.

3-15 U.S. Government, "Domestic Licensing of Production and Utilization Facilities," Title 10 Code of Federal Regulations, Part 50, Office of the Federal Register, Washington, D.C.

3-16 American Society of Mechanical Engineers, ASME Boiler and Pressure Vessel Code, Section III, Division 1, Subsection NC, 1998, including 2000 Addendum.

3-17 American Society of Mechanical Engineers, ASME Boiler and Pressure Vessel Code, Section II, Part A, 1998, including 2000 Addendum.

3-18 ASTM Metal Handbook (Volume 1).

3-19 Singular Integral Equation (Bueckner) and Asymptotic Approximation (Benthem)

3-20 NUREG/CR-1815 "Recommendation for Protecting Against Failure by Brittle Fracture in Ferritic Steel Shipping Containers Up to Four Inches Thick" Liwrence Livermore National Laboratory, June 15, 1981.

3-21 American Society of Mechanical Engineers, ASME Boiler and Pressure Vessel Code, Section XI, 1989.

3-22 American Society of Mechanical Engineers, ASME Boiler and Pressure Vessel Code, Section V, Article 6.

3-23 EPRI Technical Report 1003218 "Hot Cell Examination of ZIRLO PWR Fuel, Irradiated to 70 GWd/MTU", December 2003.

3-24 an Swam, L.F., Strasser A.A., Cook J.D., Burger J.M., "Behavior of Zircaloy-4 and Zirconium Linear Zircaloy-4 Cladding at High Burnup" Proceedings of the 1997 International Topical Meeting on LWR Fuel Performance, Portland, Oregon March 2-6, 1997.

3-25 CRL-ID-126295 "Evaluation of Low-Velocity Impact Tests of Solid Steel Billet onto Concrete Pads, and Application to Generic ISFSI Storage Cask for Tipover and Side Drop" LLNL, March 1997.

3-26 mendment No. 8 to NUHOMS® COC 1004. Addition of 24PTH DSC to Standardized NUHOMS® System" (Tables P.3.3-7 and P.3.3-8).

3-27 Handbook of Concrete Engineering", edited by Mark Fintel, Van Nostrand Reinhold Company, September, 1974..

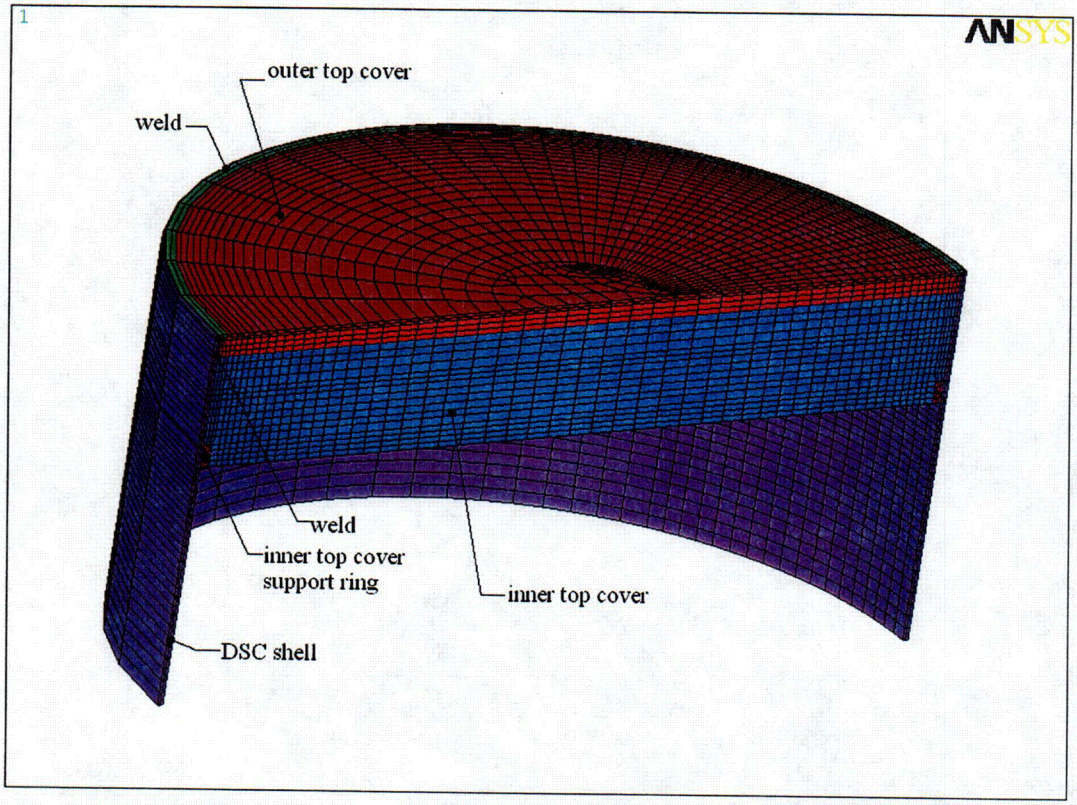

Figure 3-1
Canister Finite Element Model

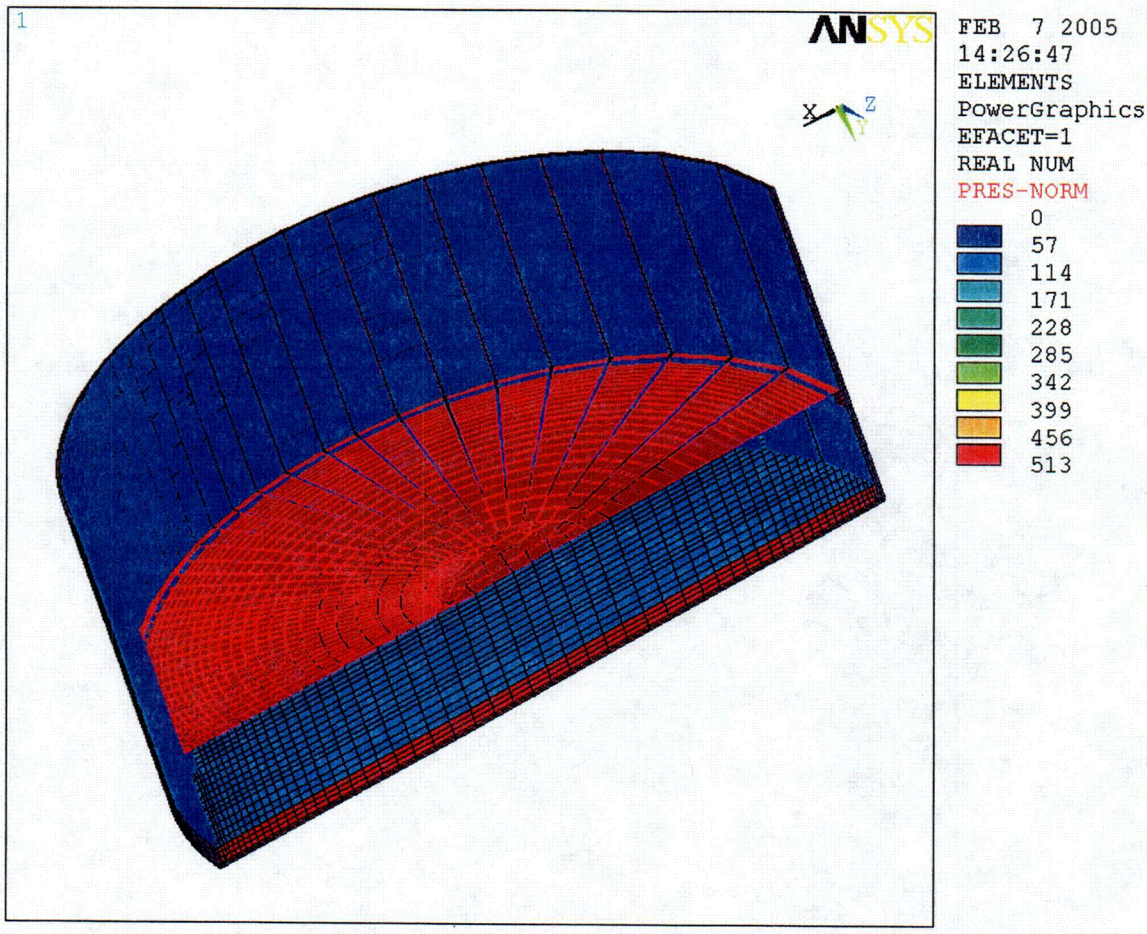

Figure 3-2
Loading Condition for DSC Corner Drop

C02

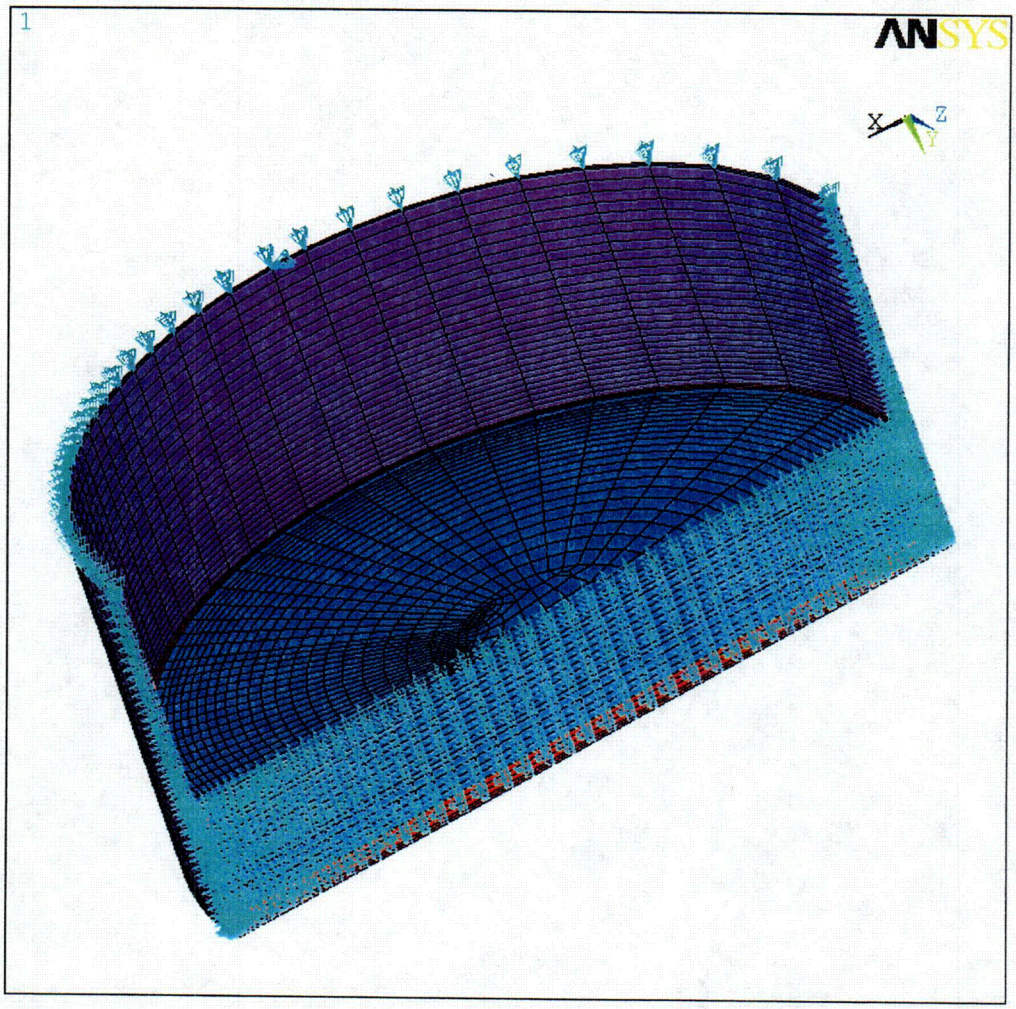

Figure 3-3
Boundary Condition for DSC Corner Drop

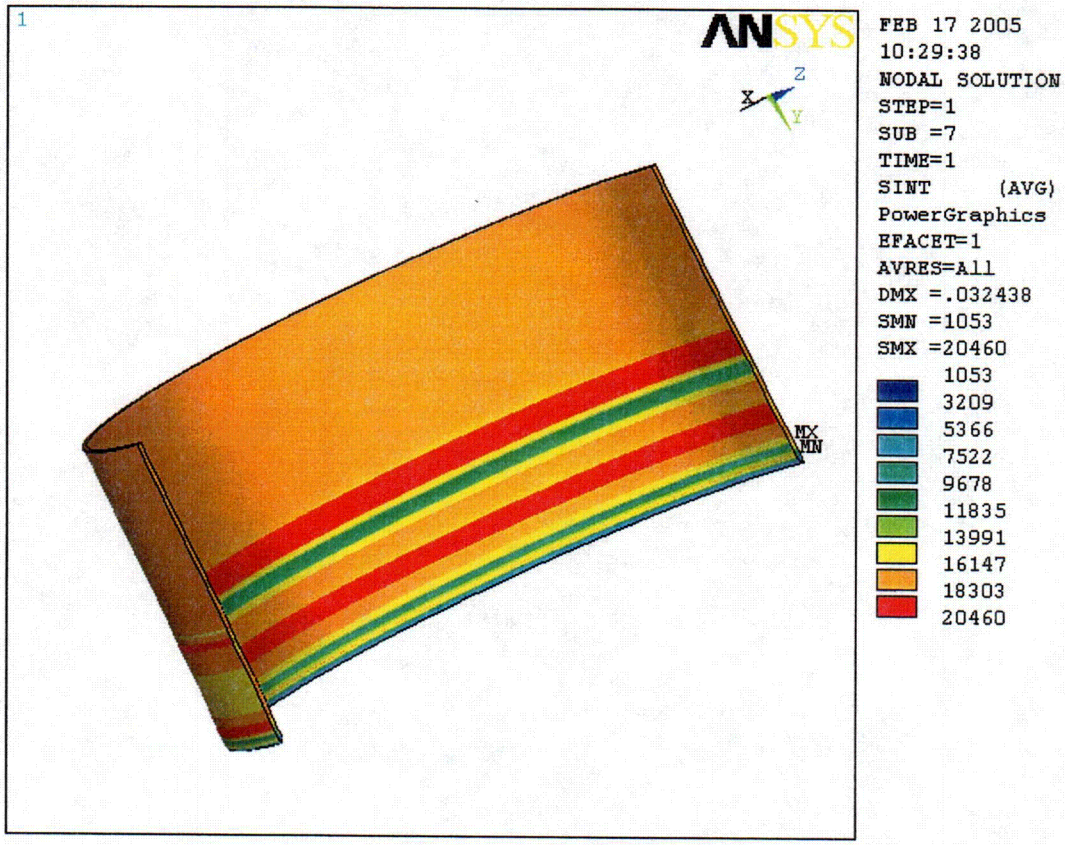

Figure 3-4
Maximum Stress Intensities in DSC Shell

C04

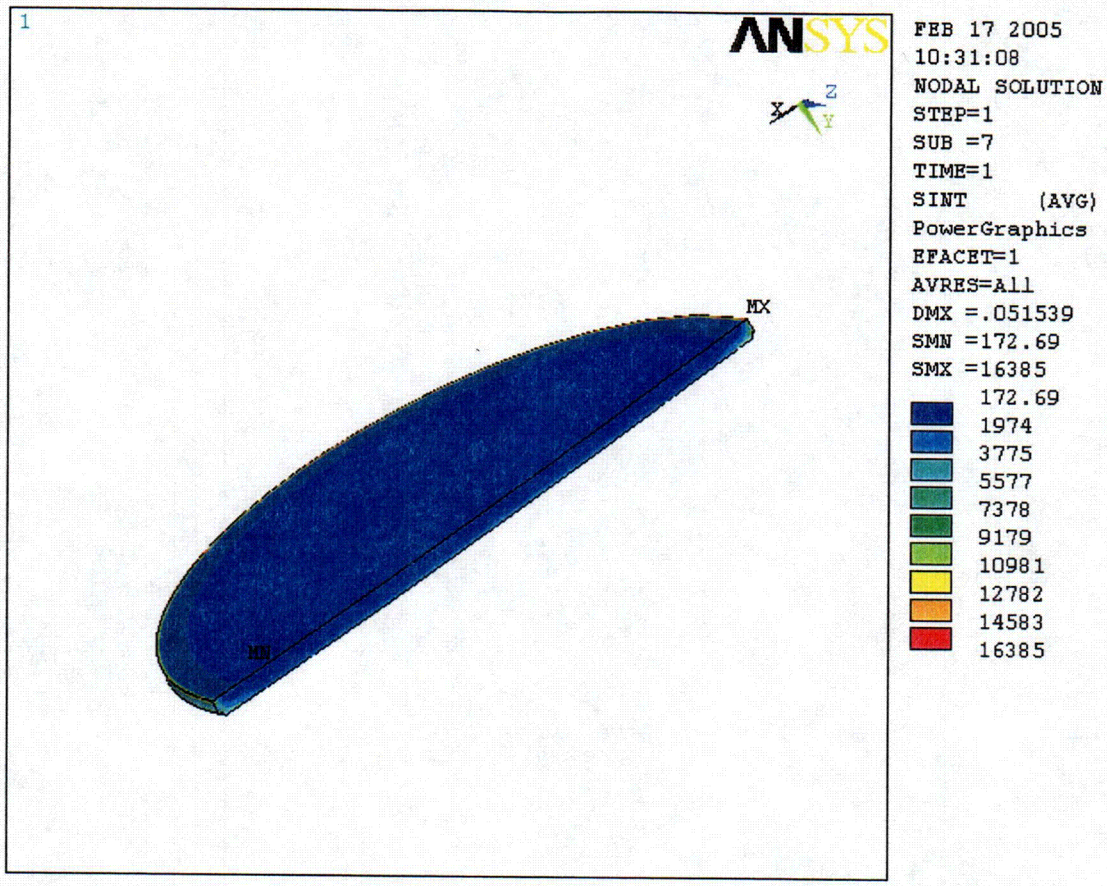

Figure 3-5
Maximum Stress Intensities in DSC Outer Top Cover

C05

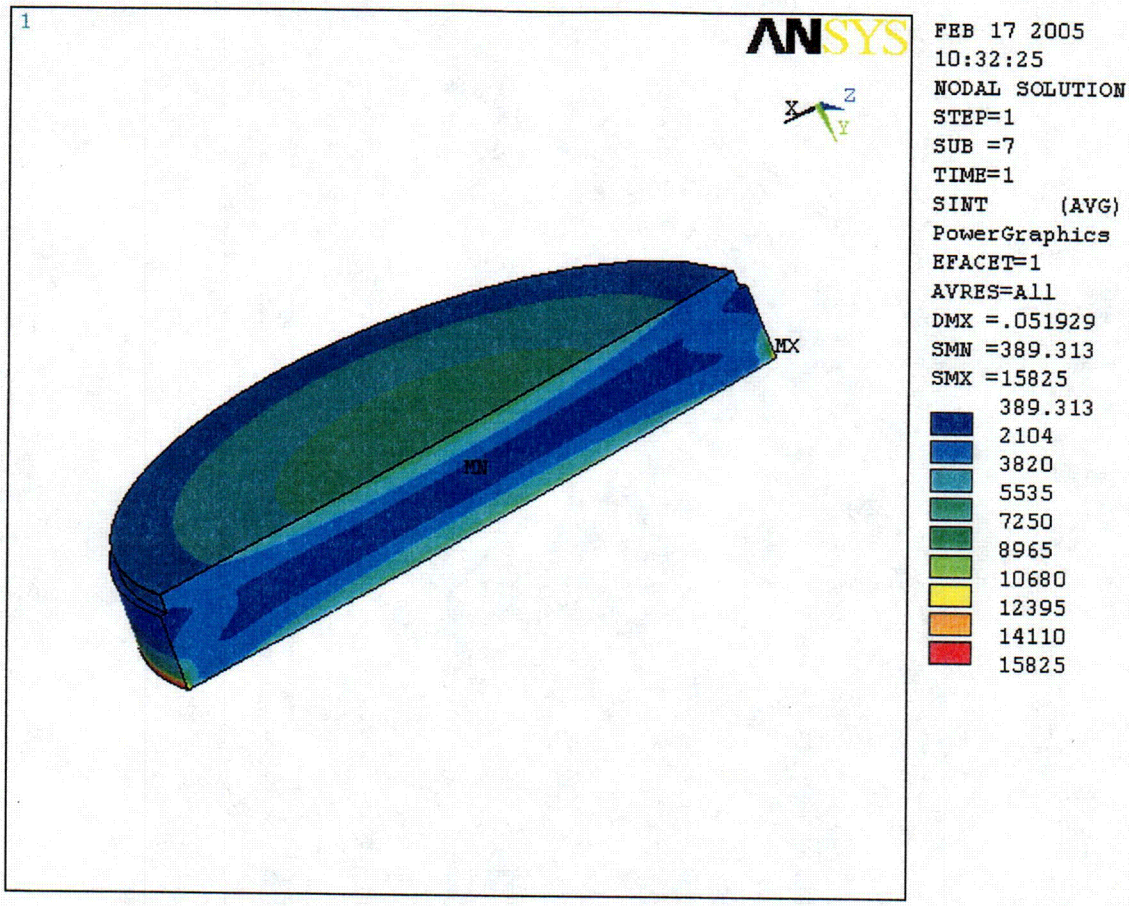

Figure 3-6
Maximum Stress Intensities in DSC Inner Top Cover

C06

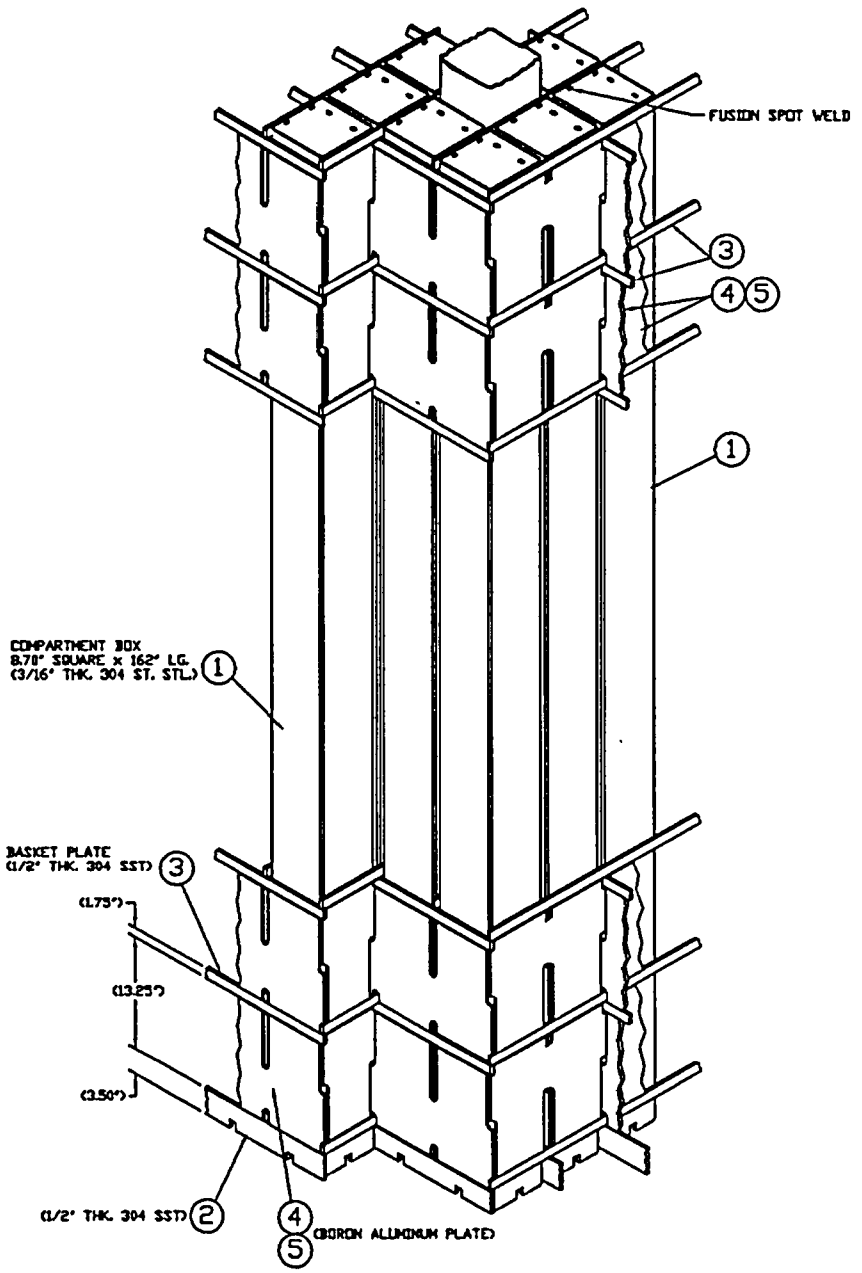

Figure 3-7
32PTH Basket Assembly

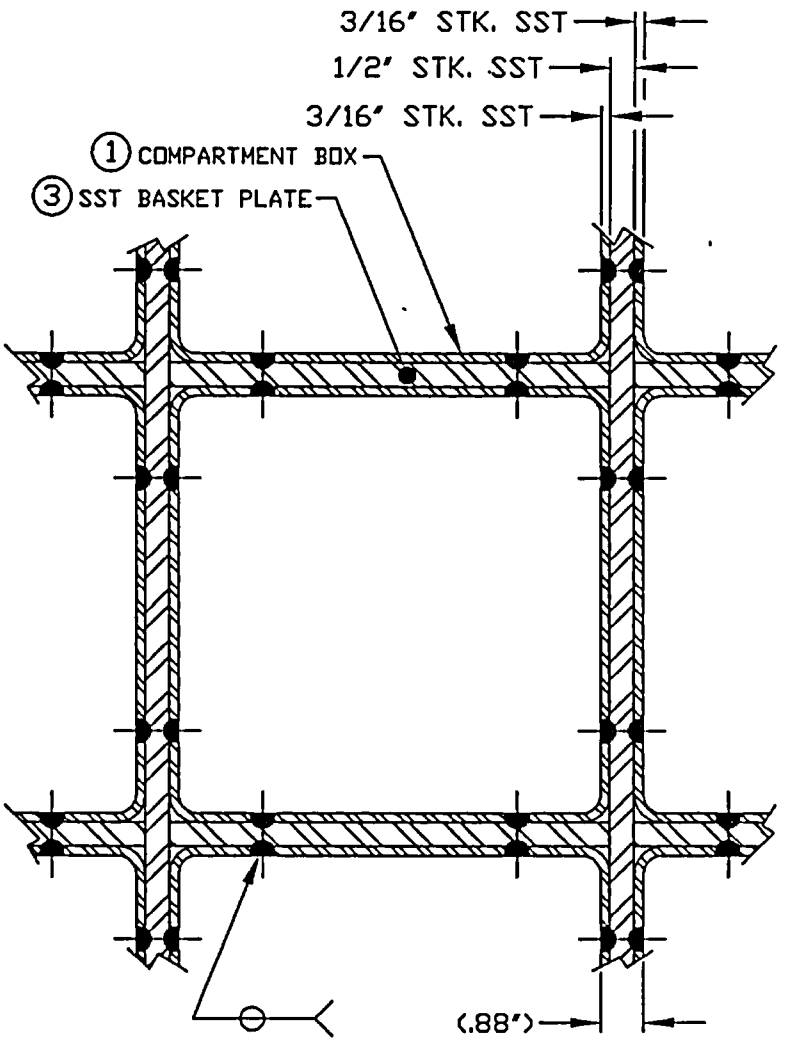

Figure 3-8
32PTH Basket Weld

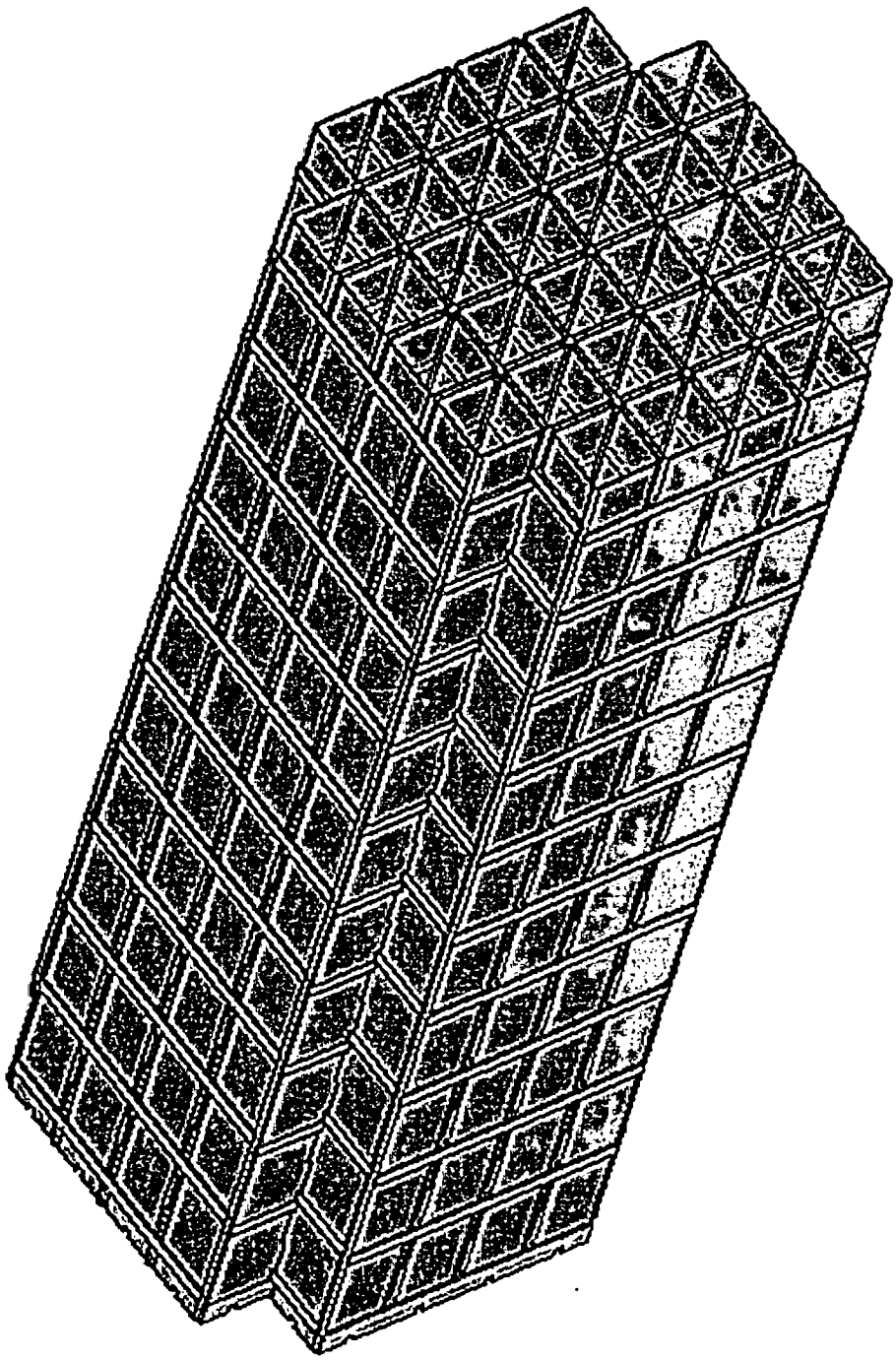

Figure 3-9
32PTH Basket SS Tube Assembly

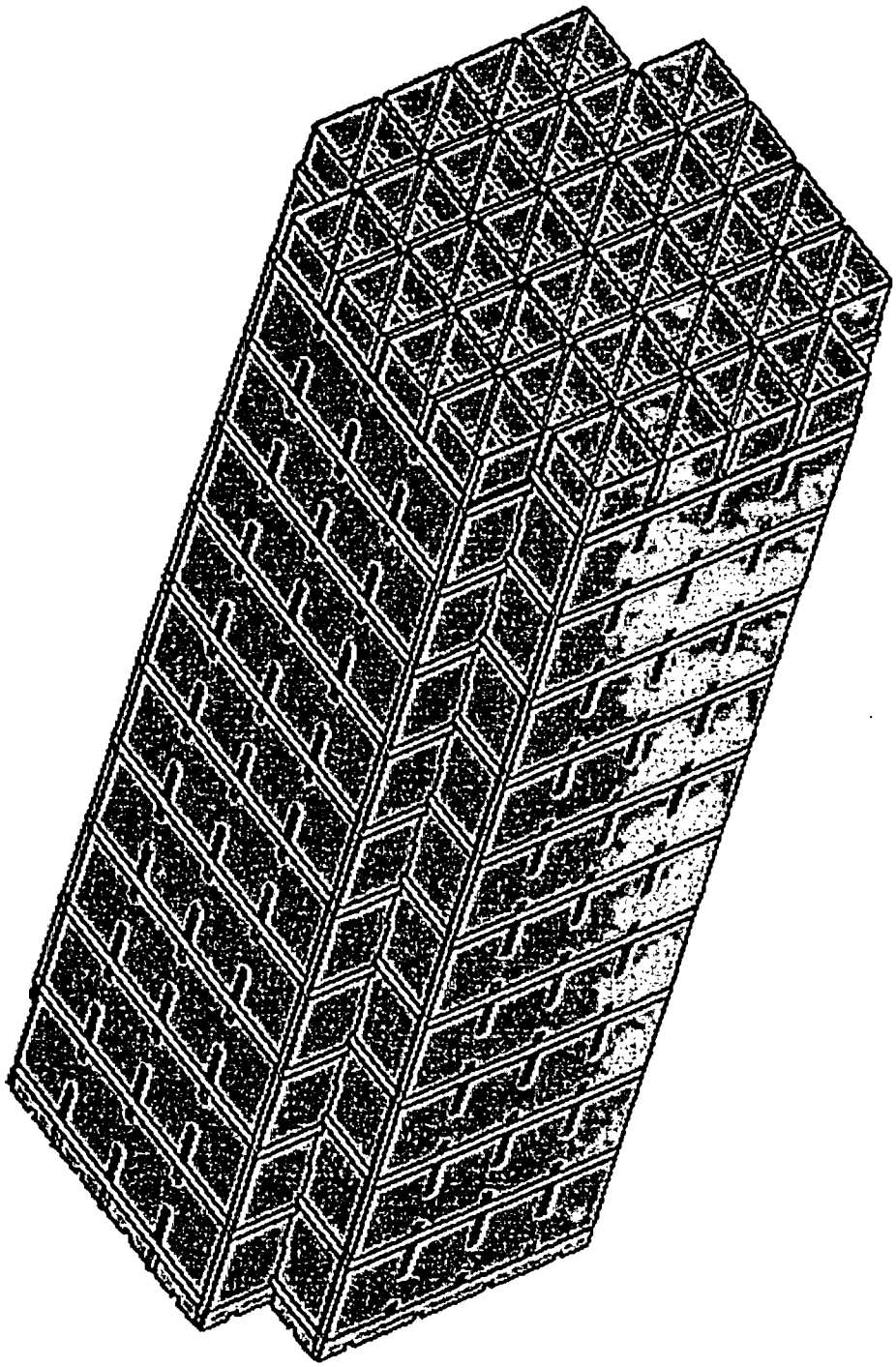

Figure 3-10
32PTH Basket SS Tube with Aluminum Plate

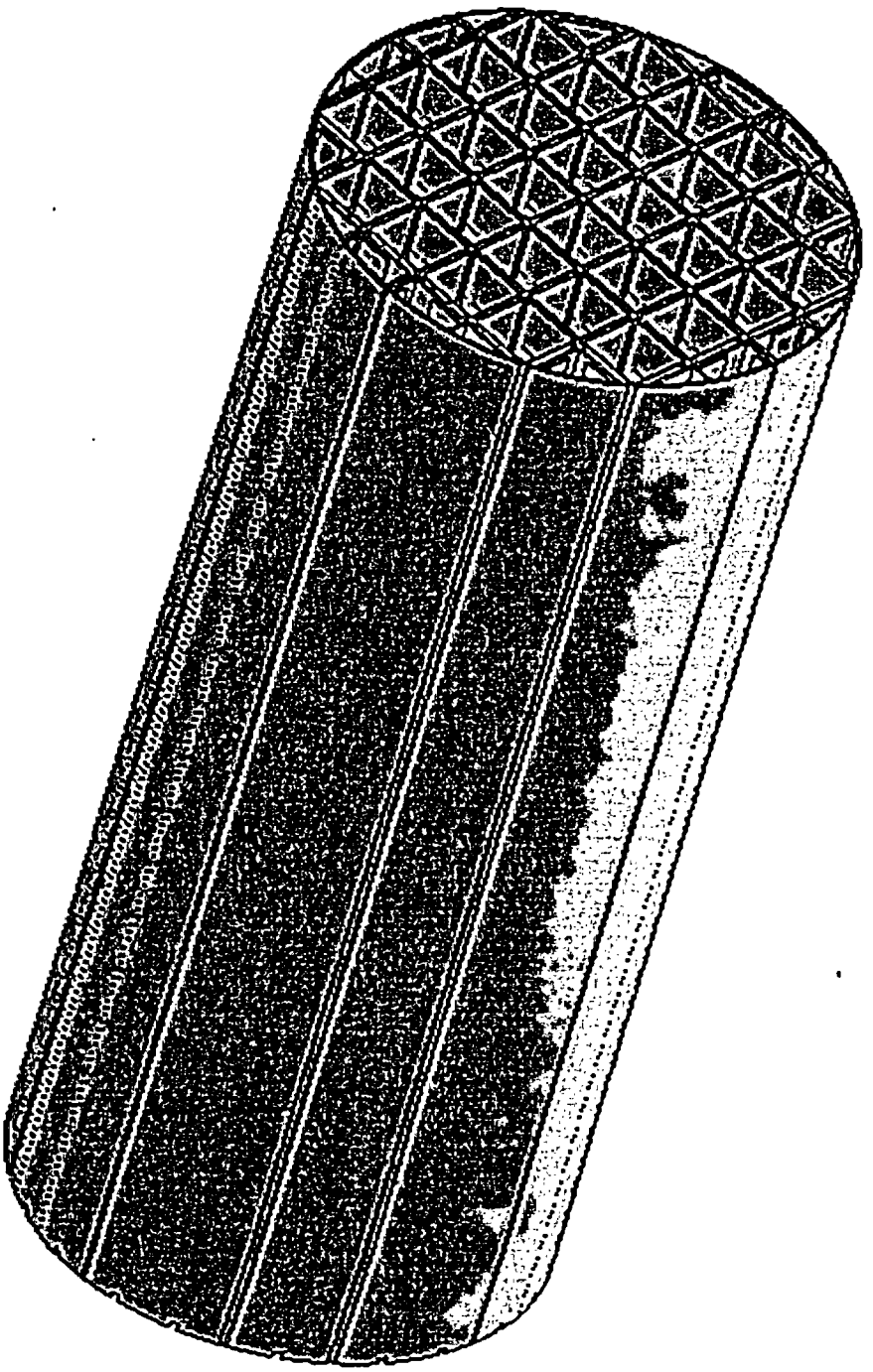

Figure 3-11
32PTH Basket with SS Rails

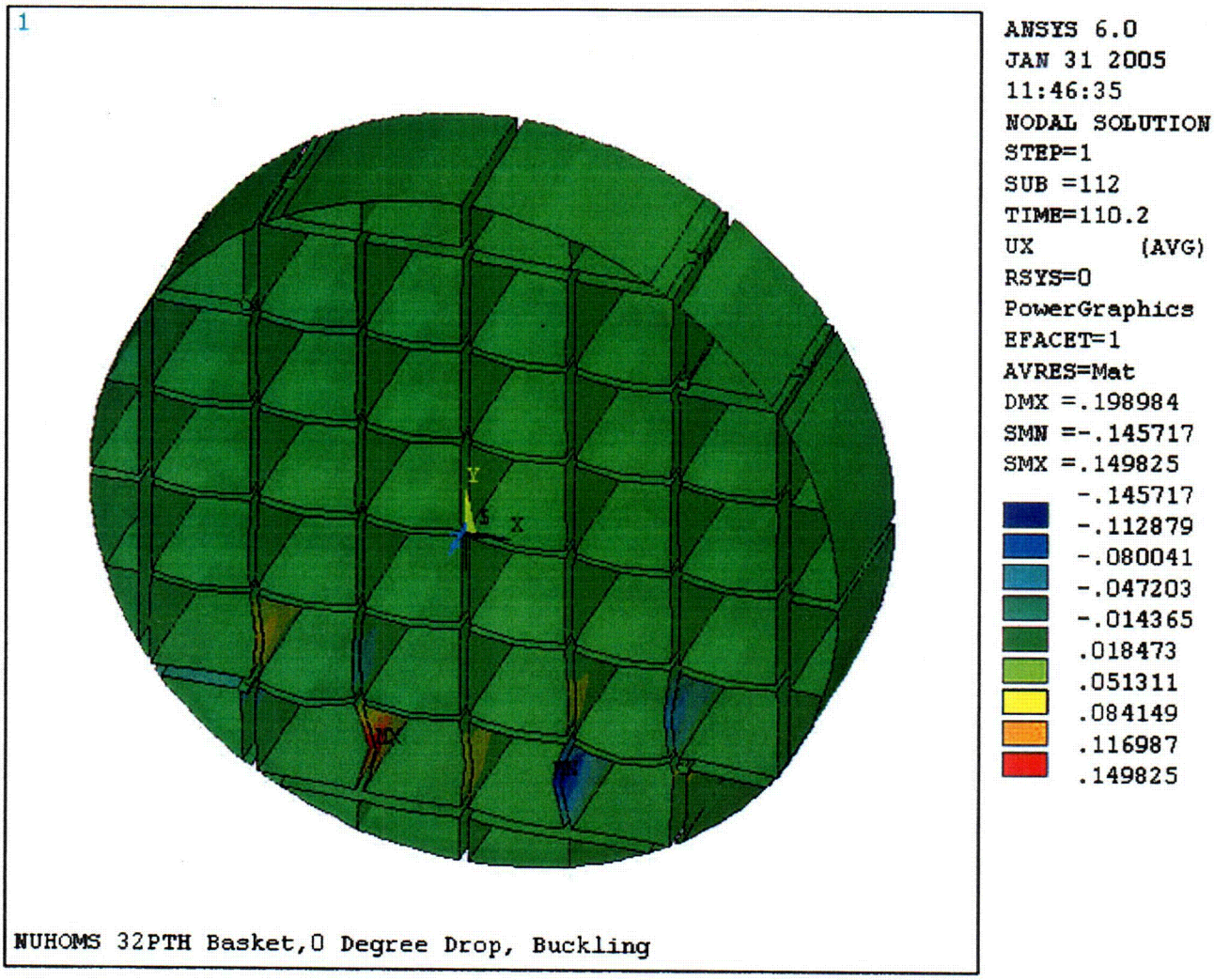

Figure 3-12
0^0 Drop Basket Deformation Plot

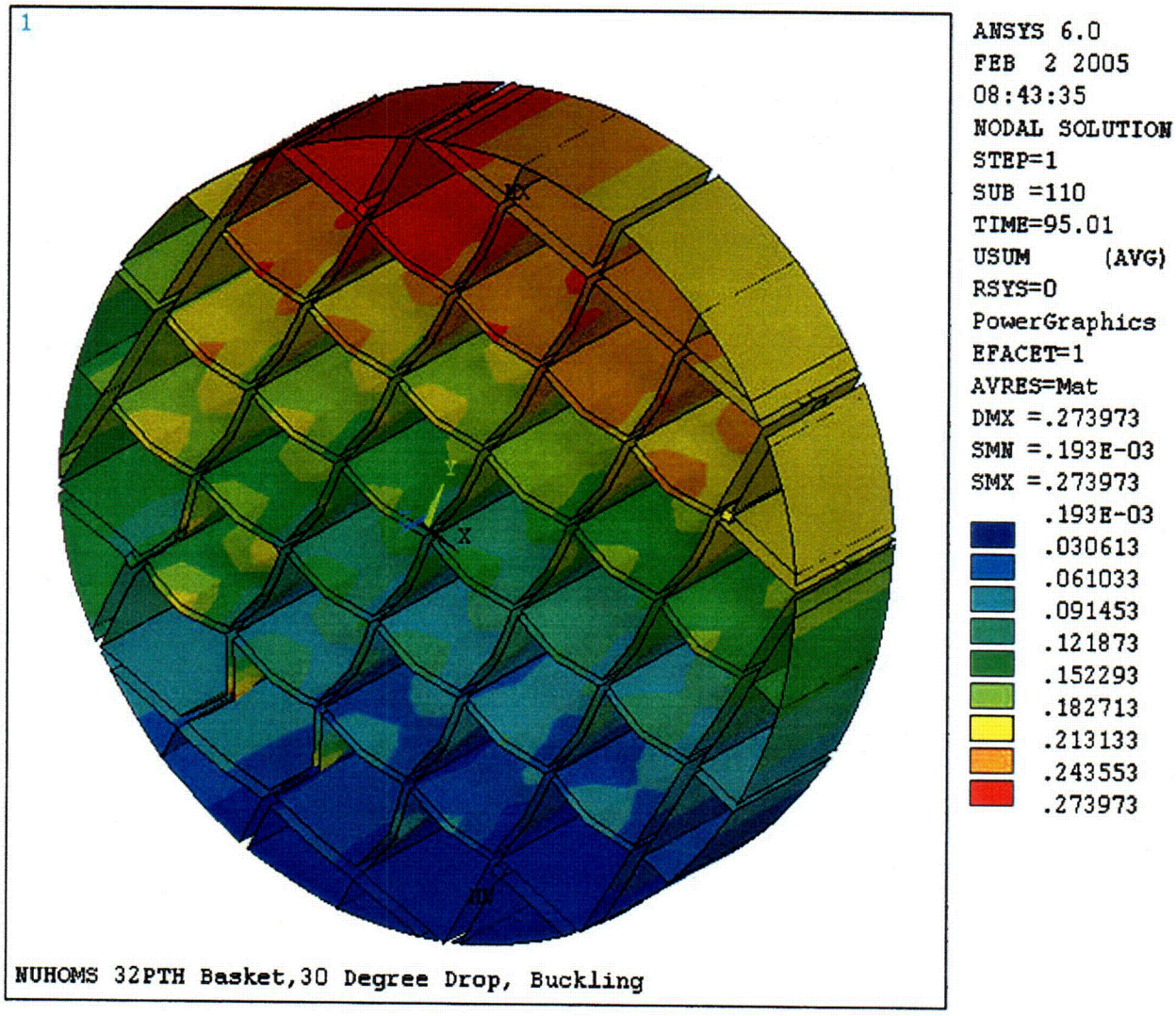

Figure 3-13
30^0 Drop Basket Deformation Plot

C08

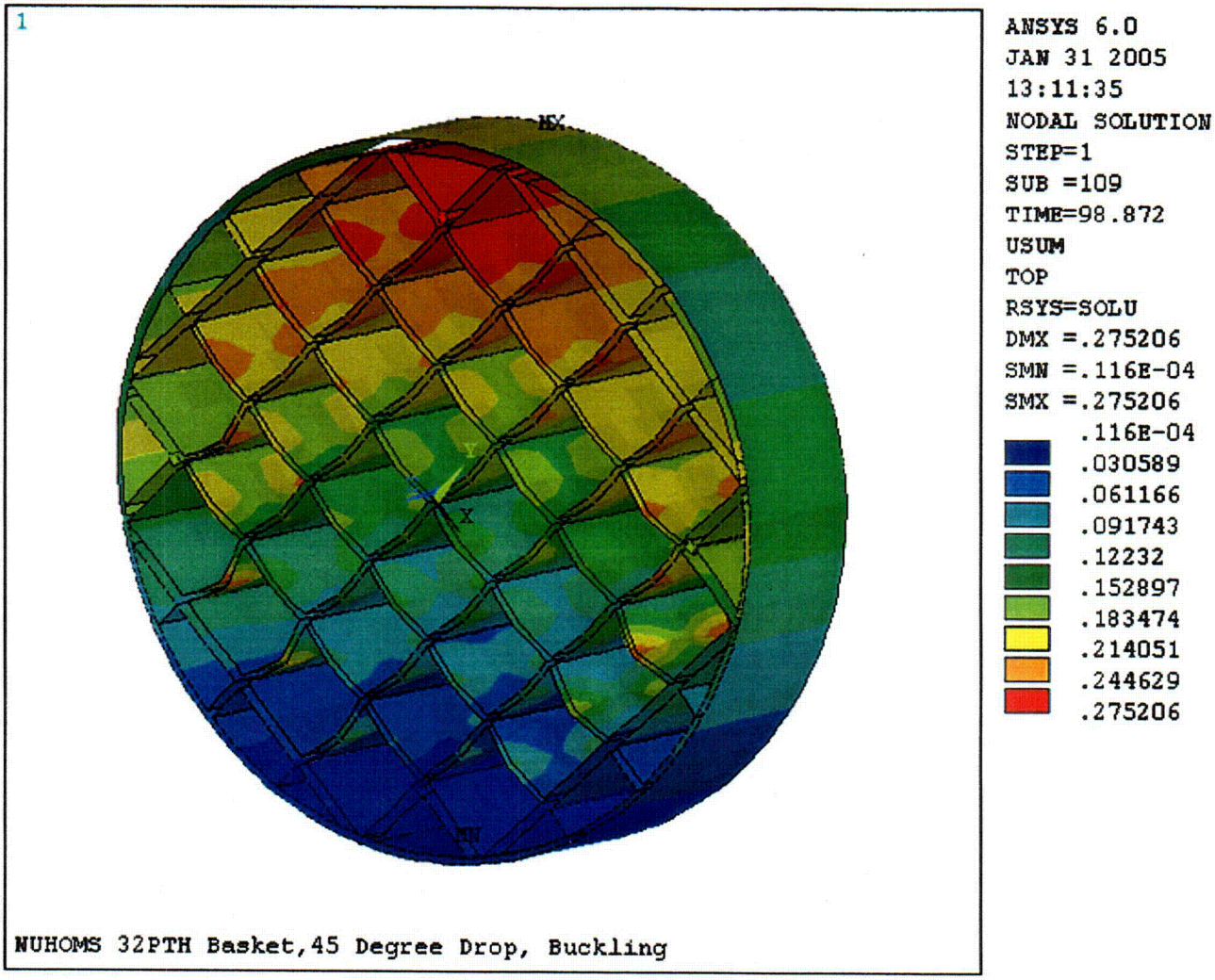

Figure 3-14
45^0 Drop Basket Deformation Plot

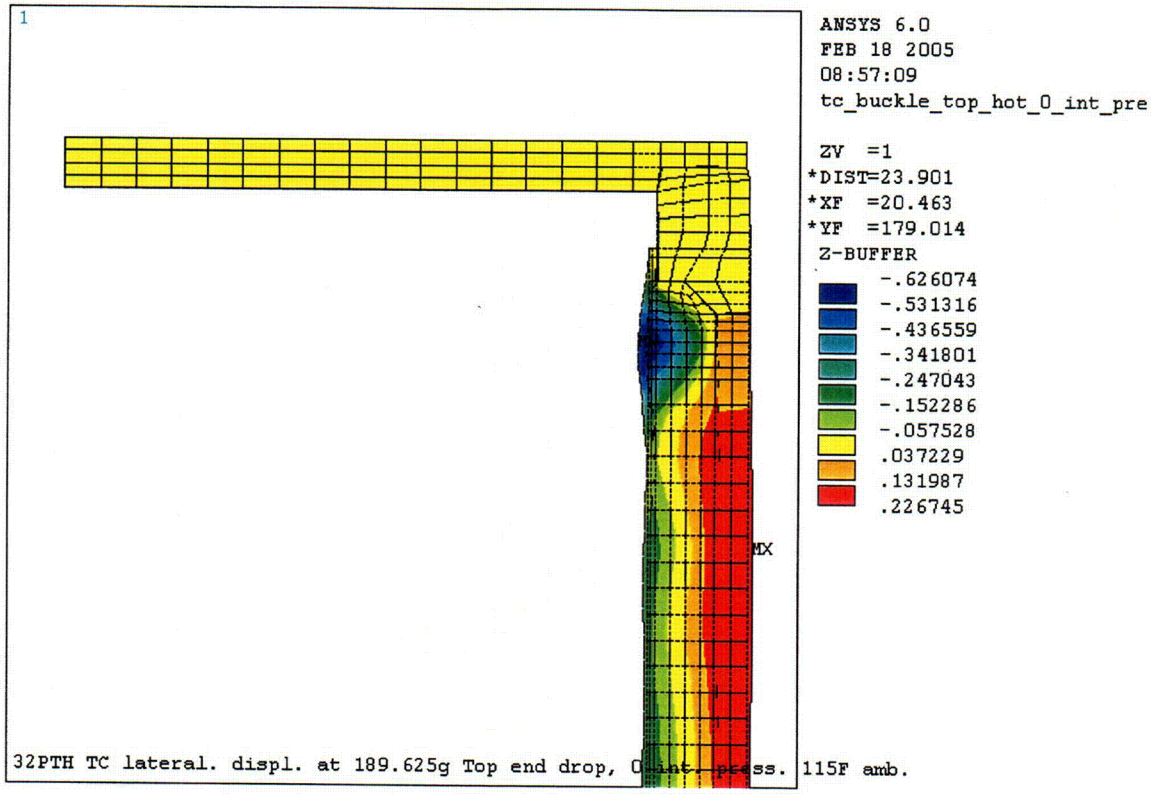

Figure 3-15
Transfer Cask Top End Drop Deformation Plot (at 189.625g)

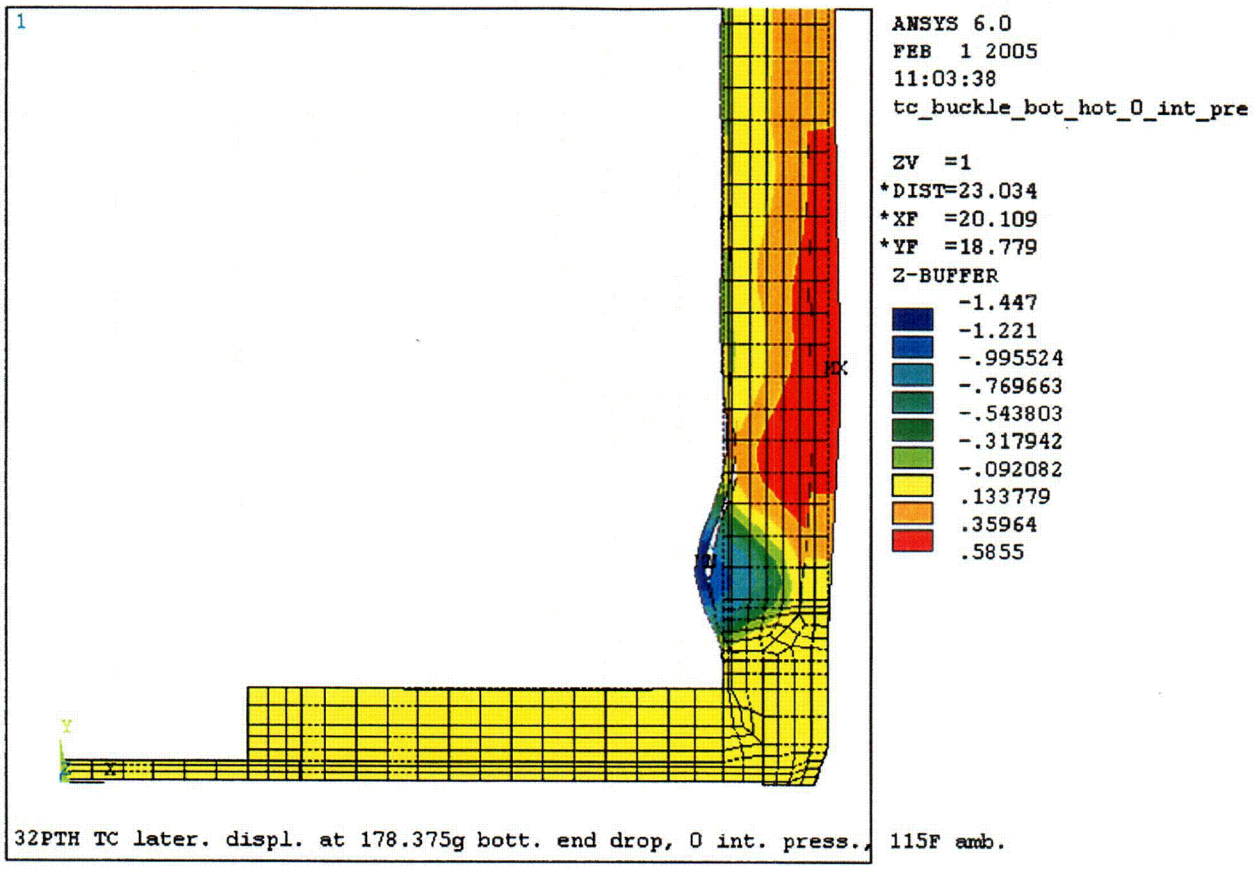

Figure 3-16
Transfer Cask Bottom End Drop Deformation Plot (at 178.375g)

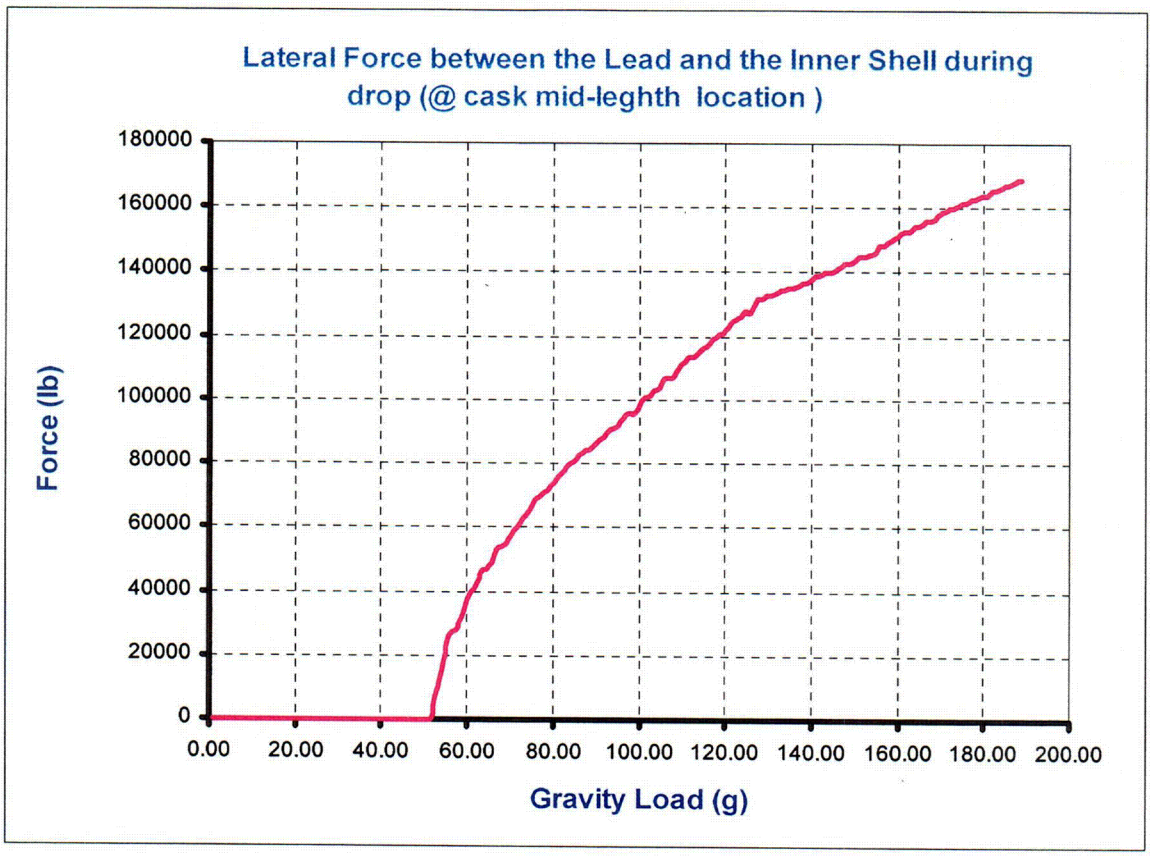

Figure 3-17
Lateral Force Exerted on Inner Shell (Transfer Cask Top End Drop)

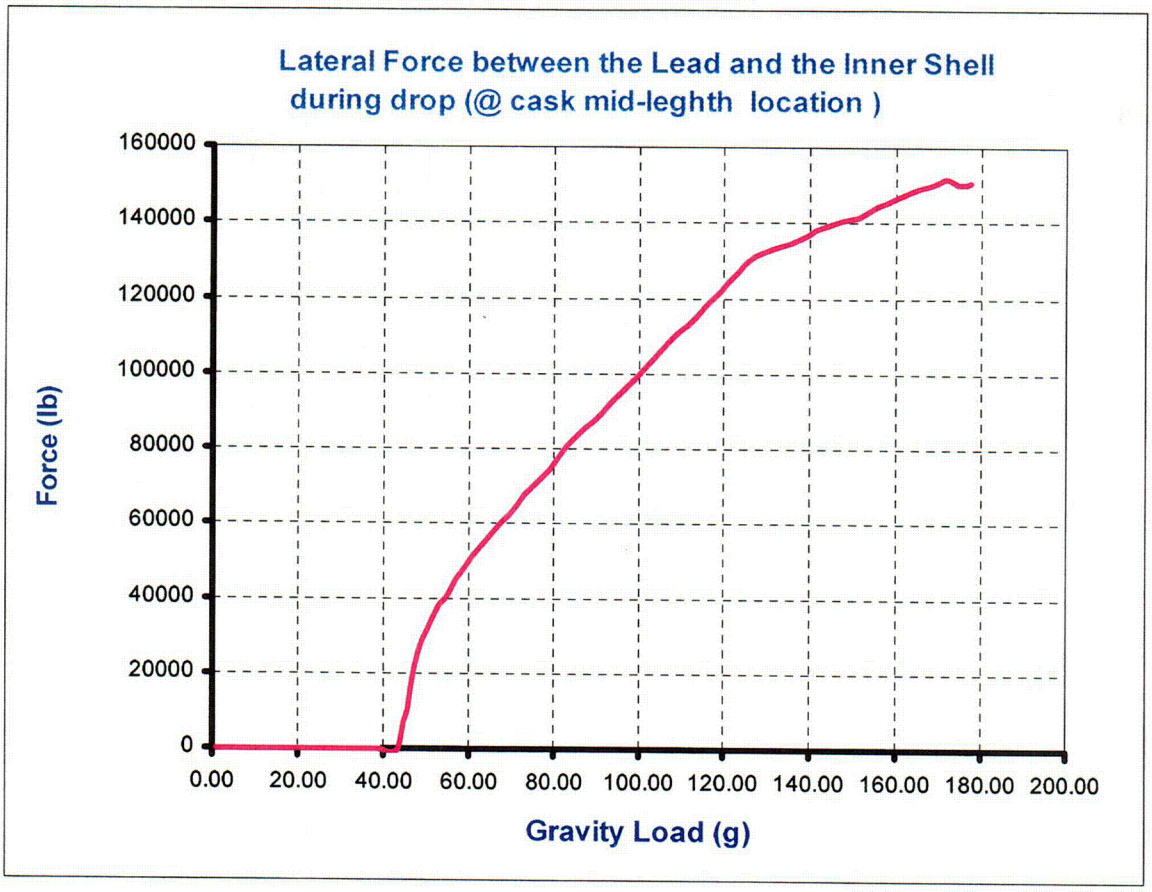

Figure 3-18
Lateral Force Exerted on Inner Shell (Transfer Cask Bottom End Drop)

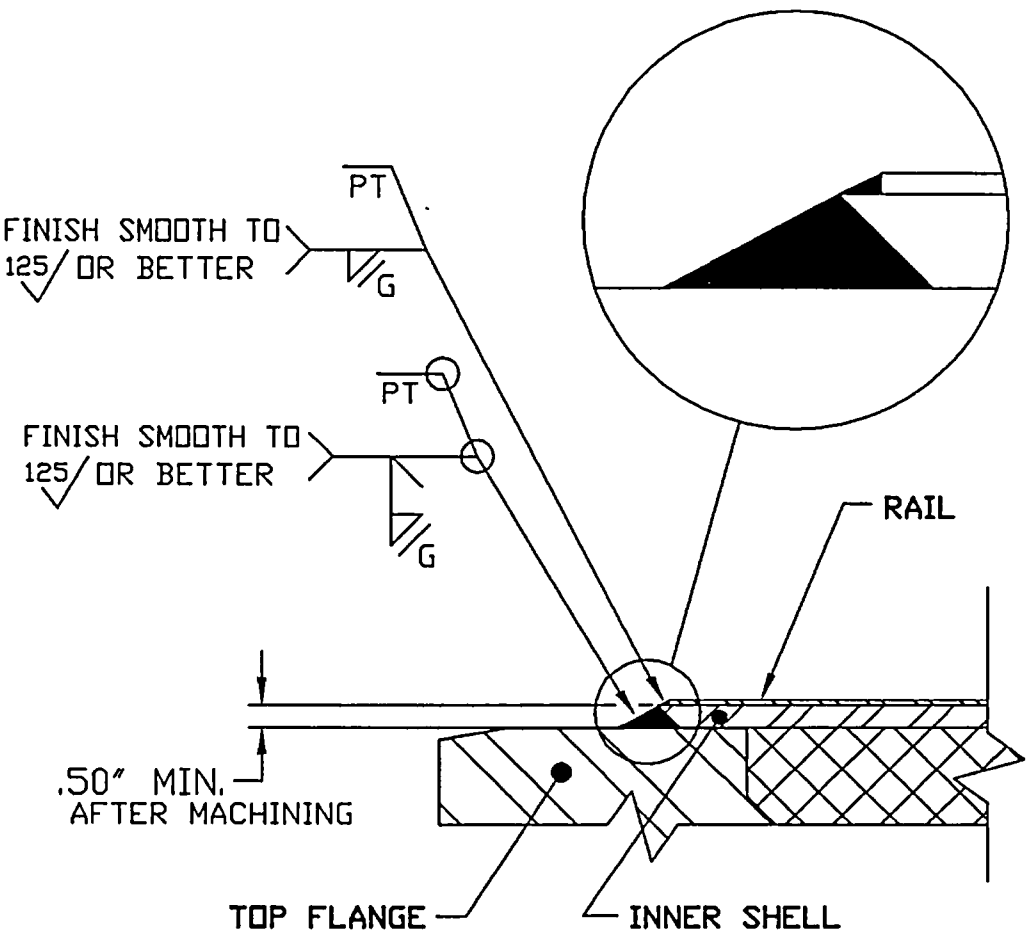

Figure 3-19
Transfer Cask Inner Shell & Flange Weld Details

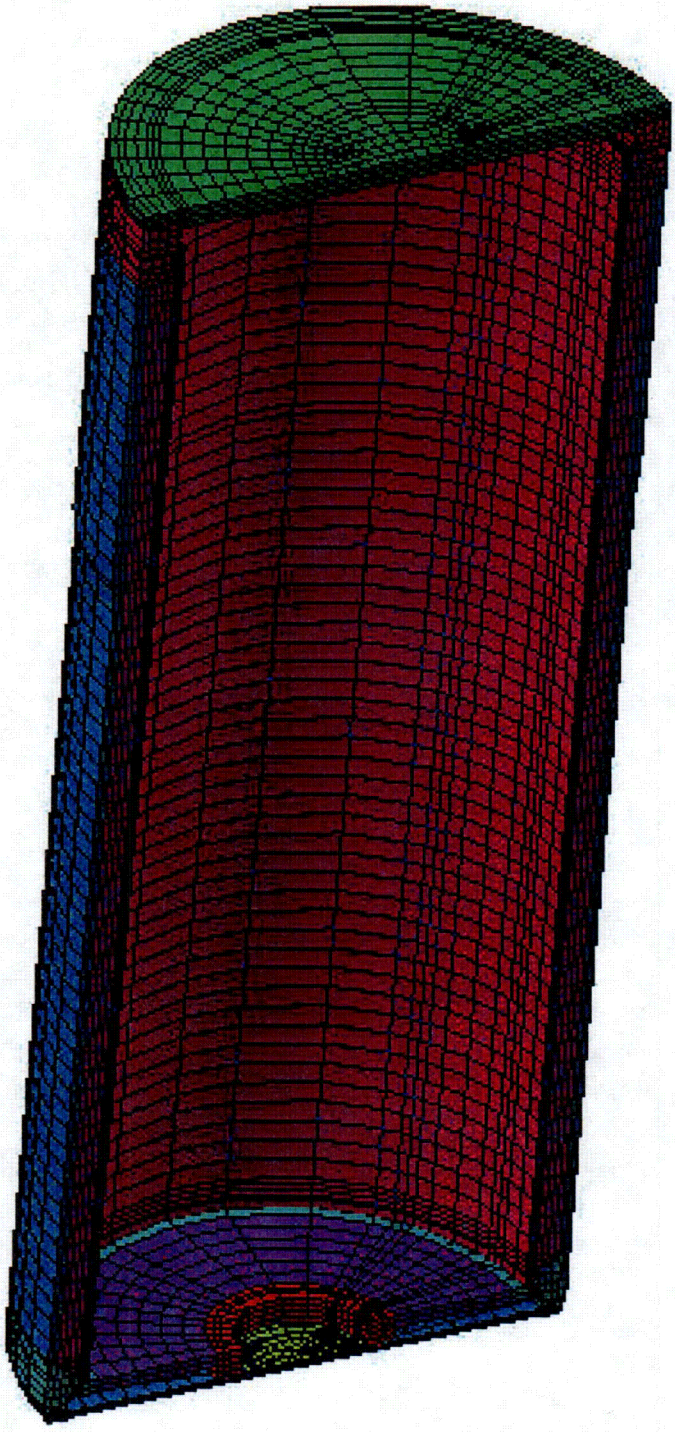

Figure 3-20
3D - Model of Transfer Cask

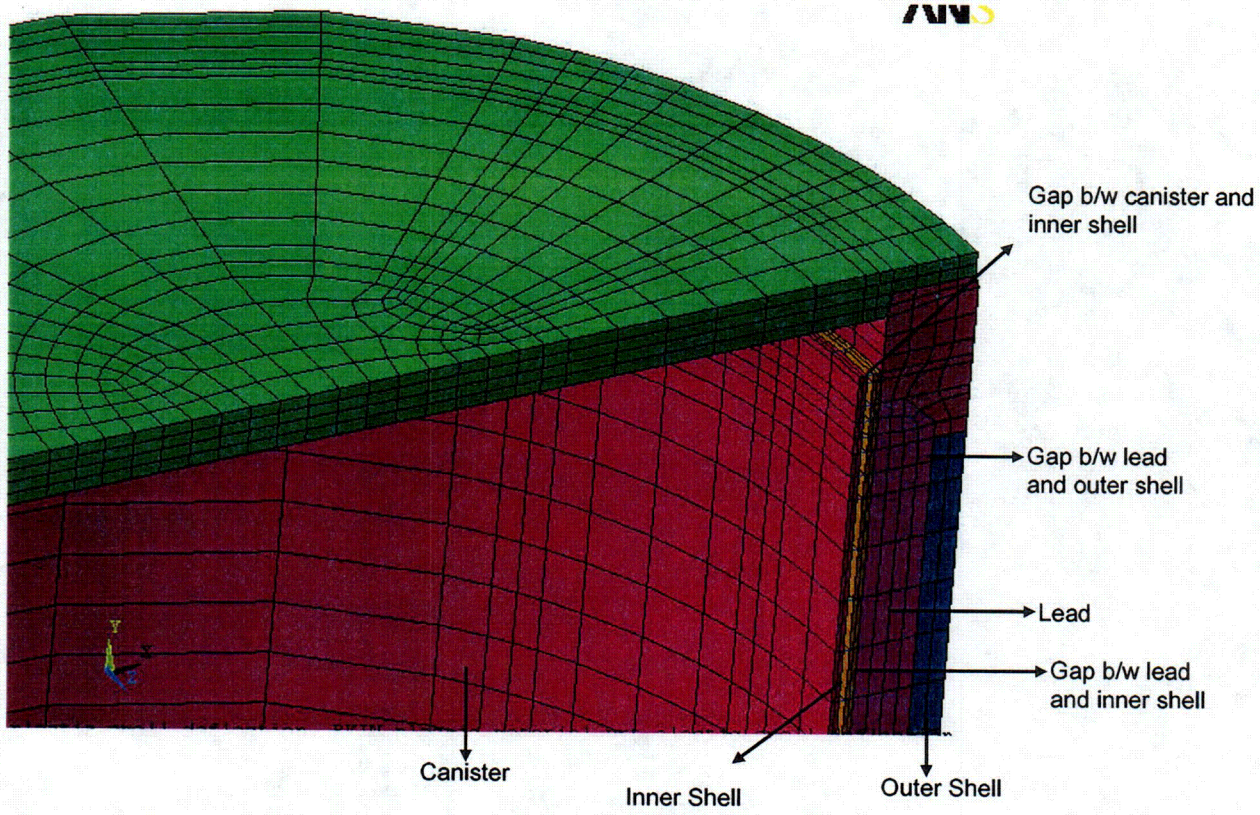

Figure 3-21
Canister/Cask Top Cover/Flange/CONTACT 52 Element Representation

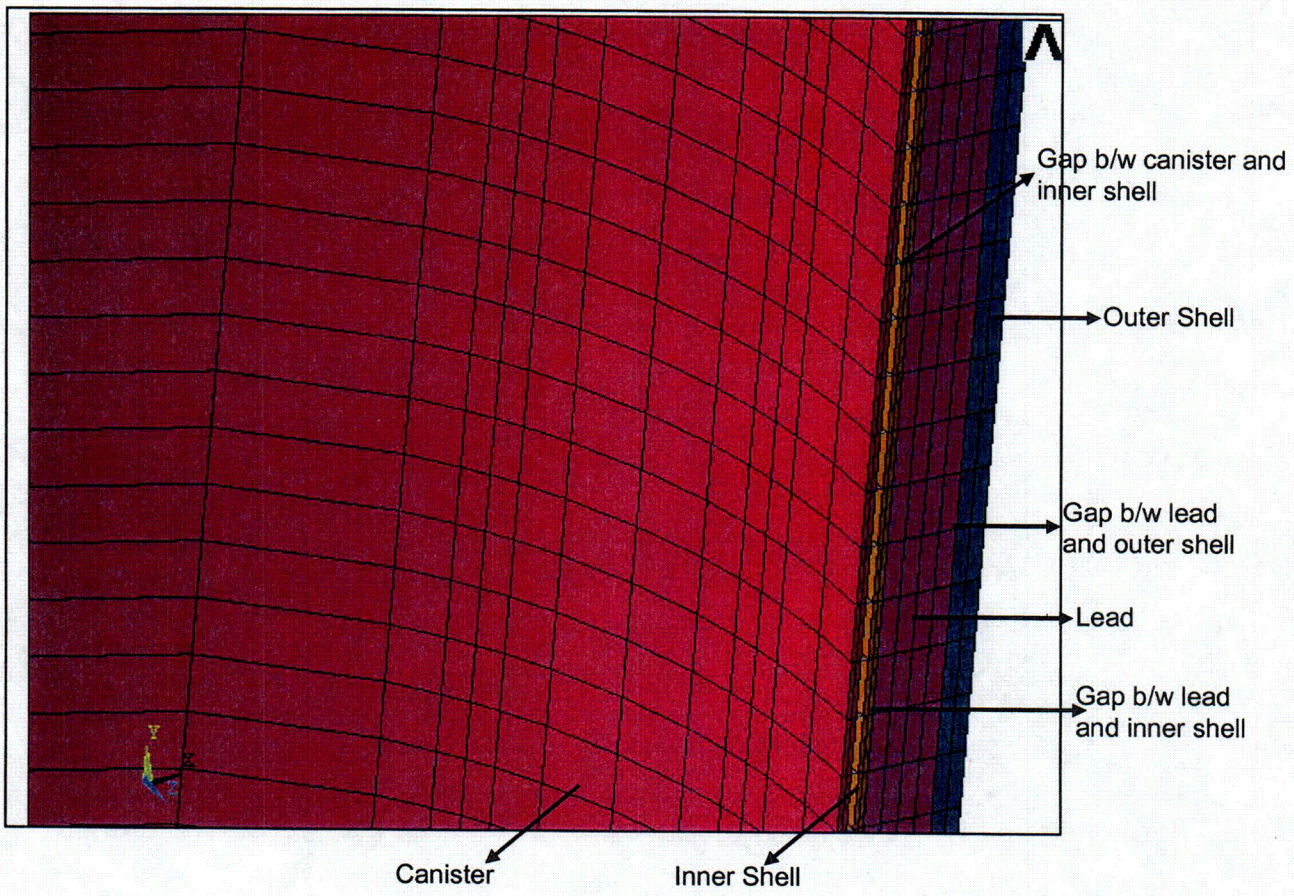

Figure 3-22
Canister/ Cask Shell /Lead /CONTACT 52 Element Representation

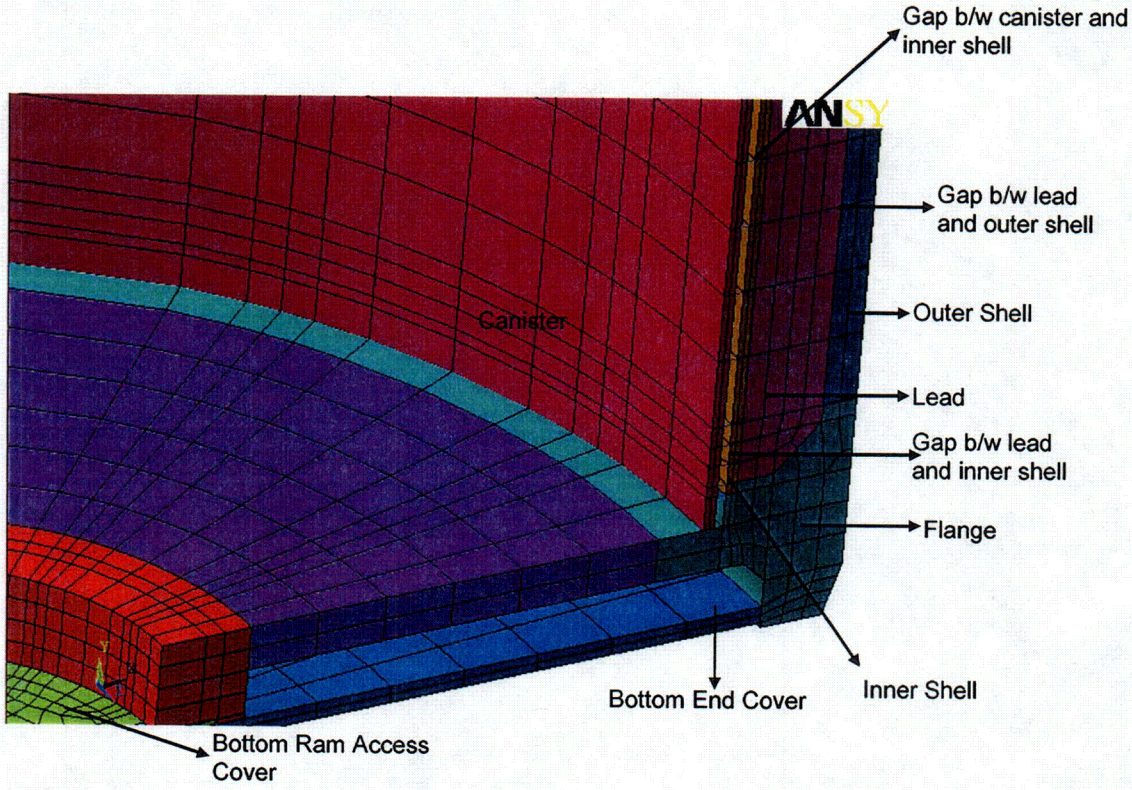

Figure 3-23
Canister/ Cask Bottom Access/Shell/ Flange/ Lead /CONTACT 52 Element Representation

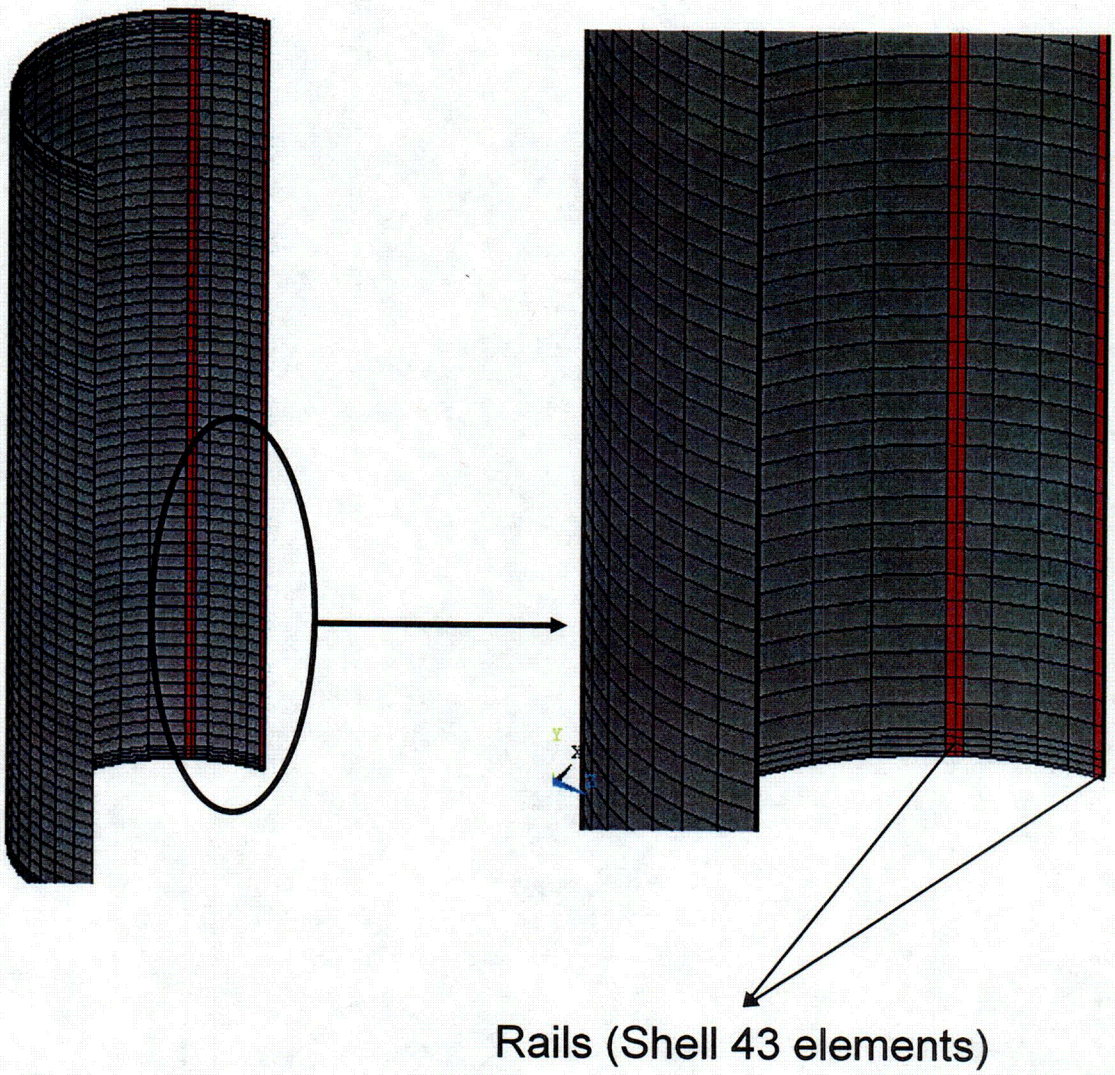

Figure 3-24
Transfer Cask Inner Shell & Rails

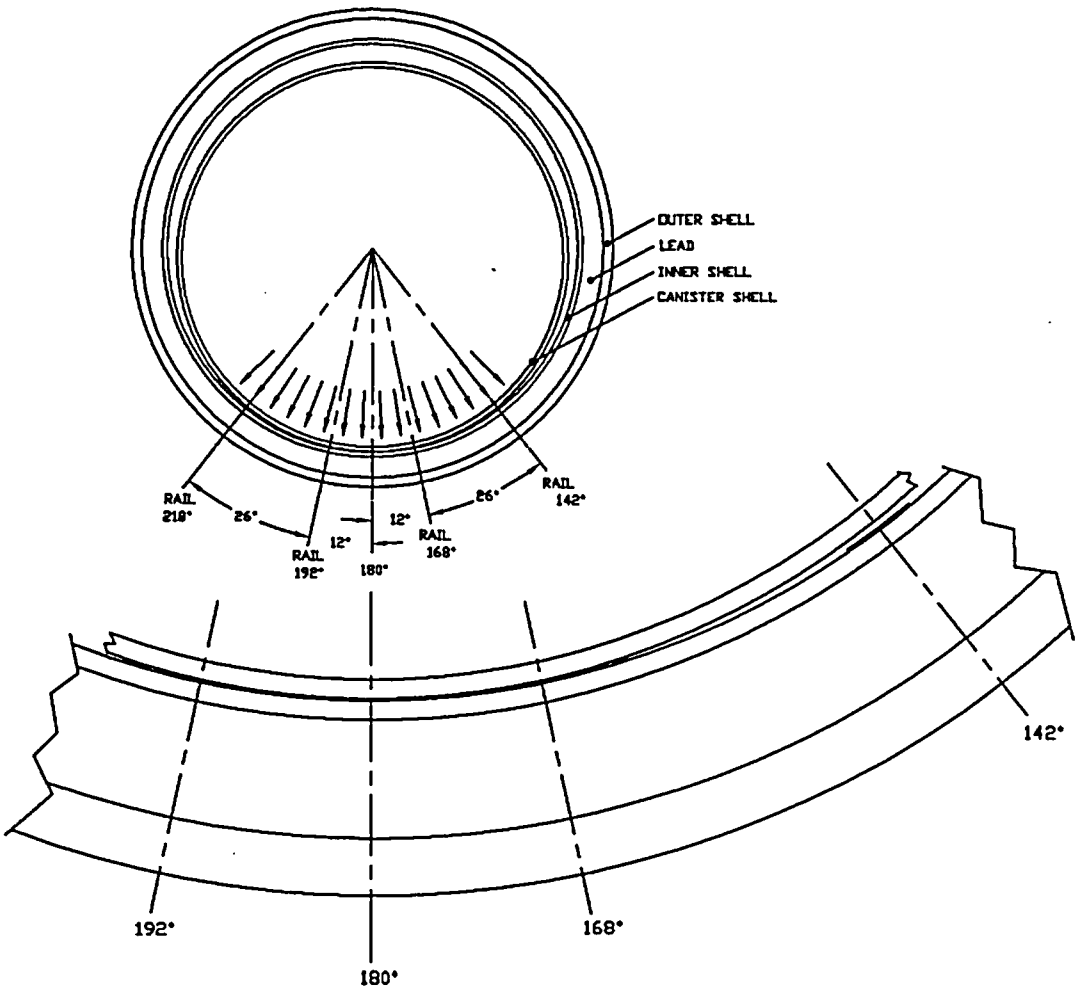

Figure 3-25

Drop Sketch for Initial Impact @ both 168^0 and 192^0 Rails (Load Case 1)

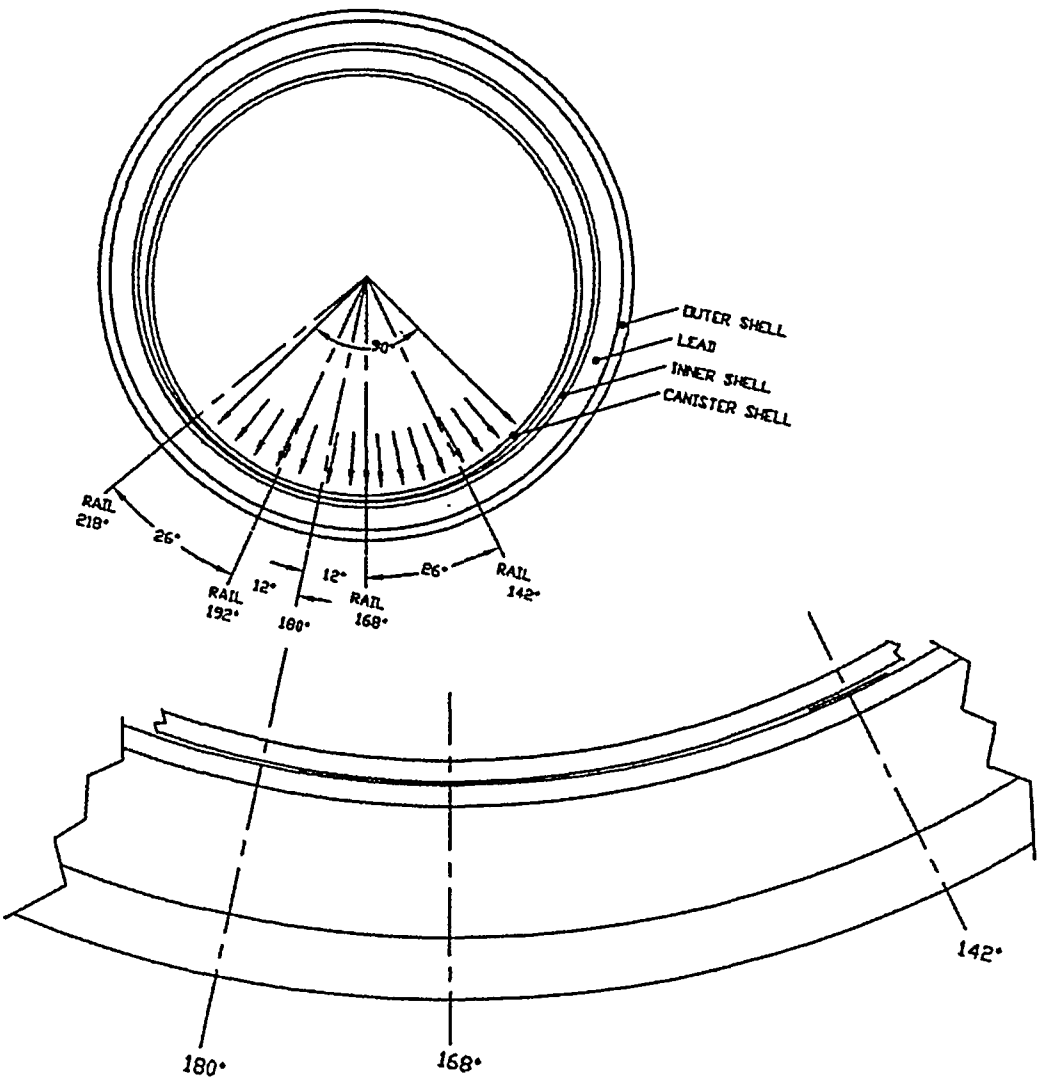

Figure 3-26
Drop Sketch for Initial Impact @ 168°Rail (Load Case 2)

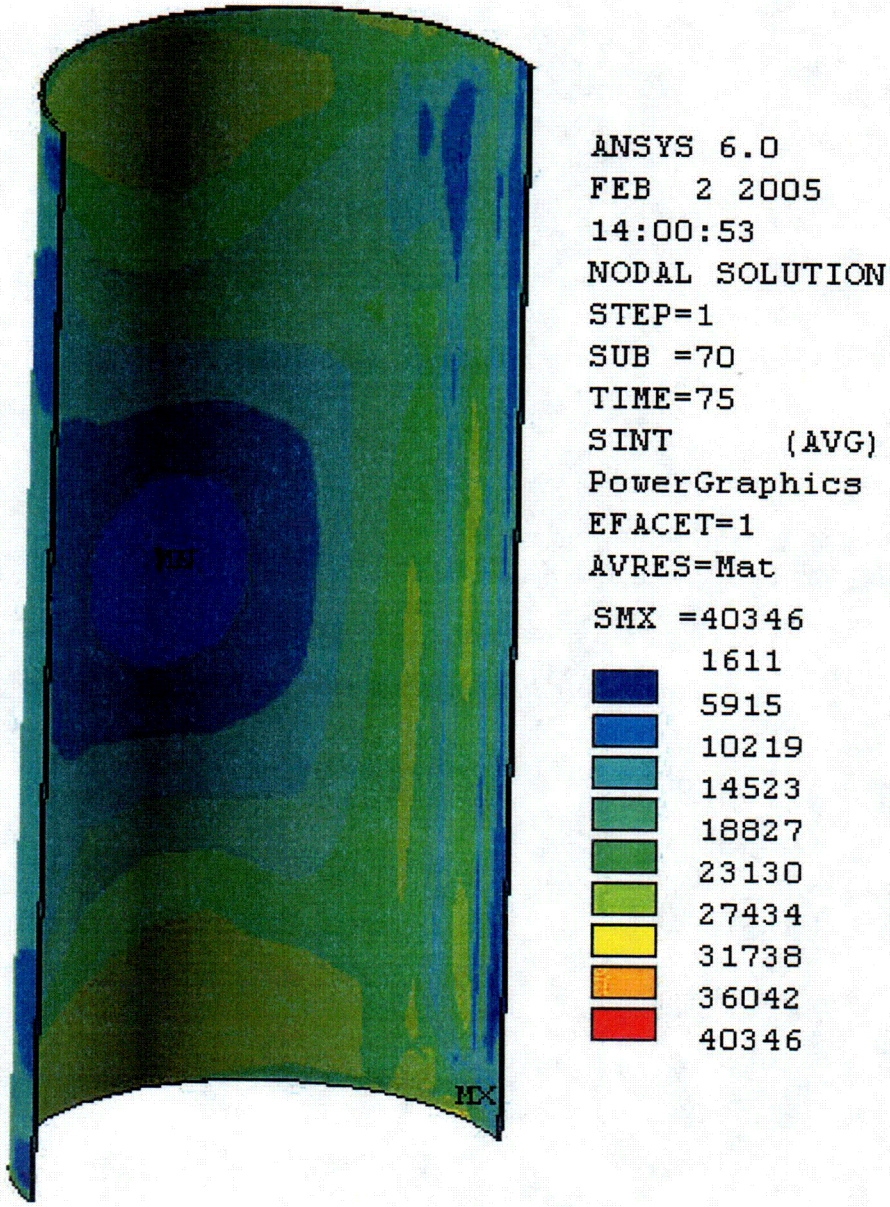

Figure 3-27
Inner Shell Stress Intensity Plot (Load Case 1)

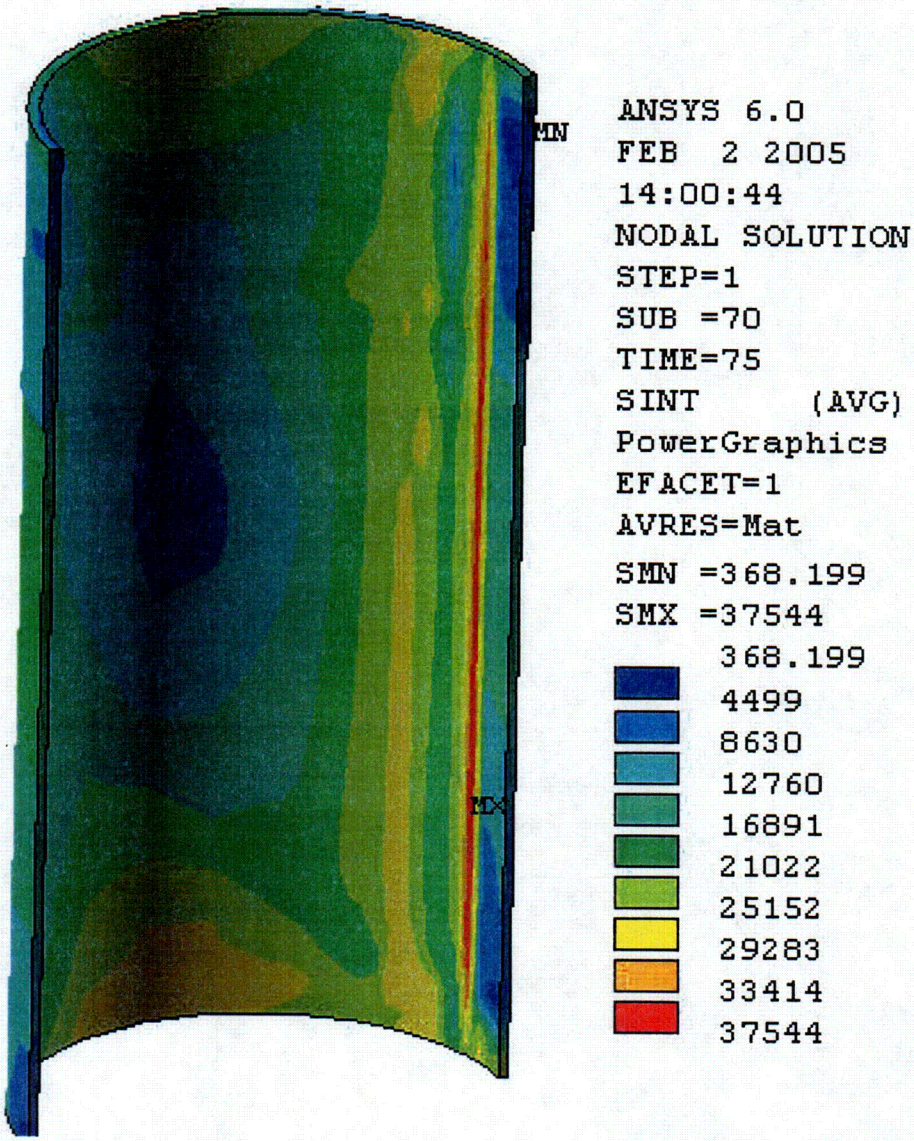

Figure 3-28
Outer Shell Stress Intensity Plot (Load Case 1)

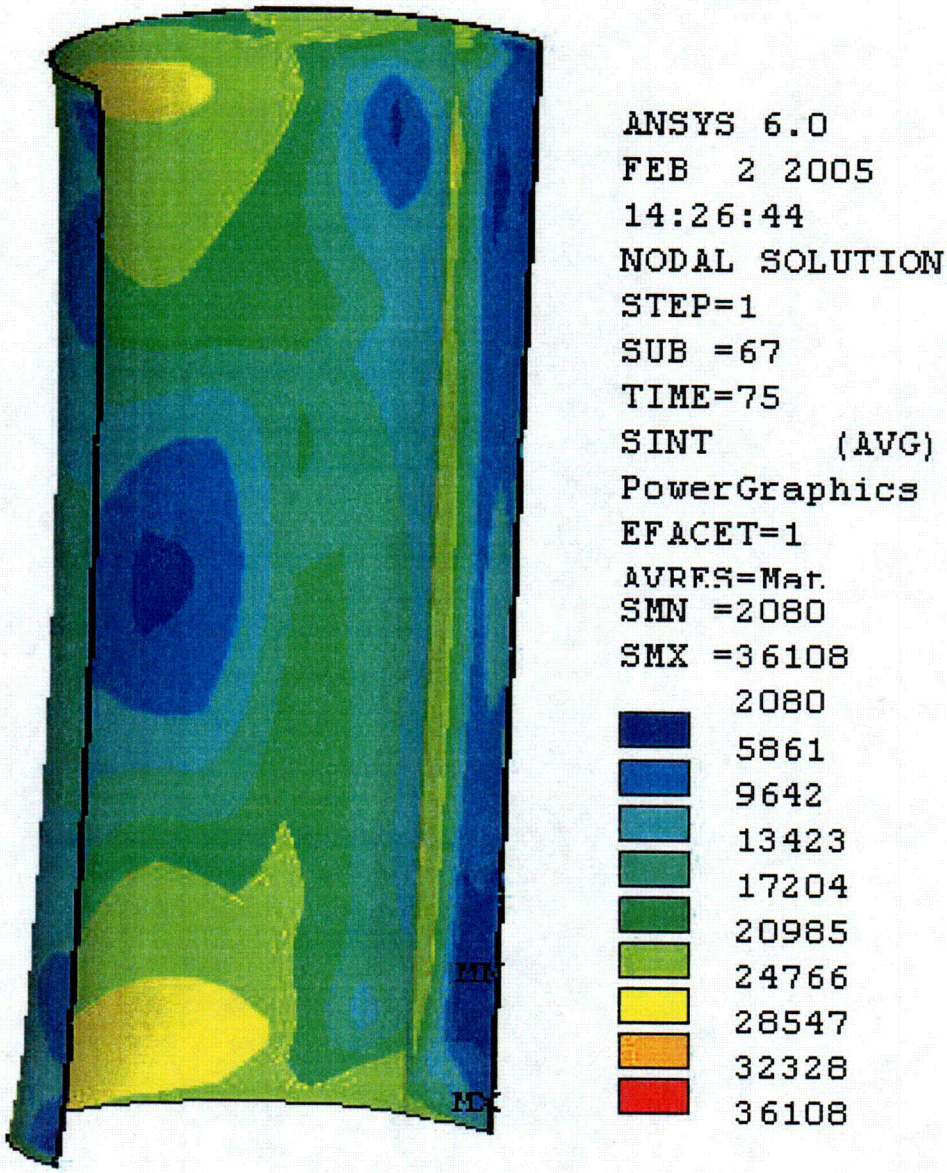

Figure 3-29
Inner Shell Stress Intensity Plot (Load Case 2)

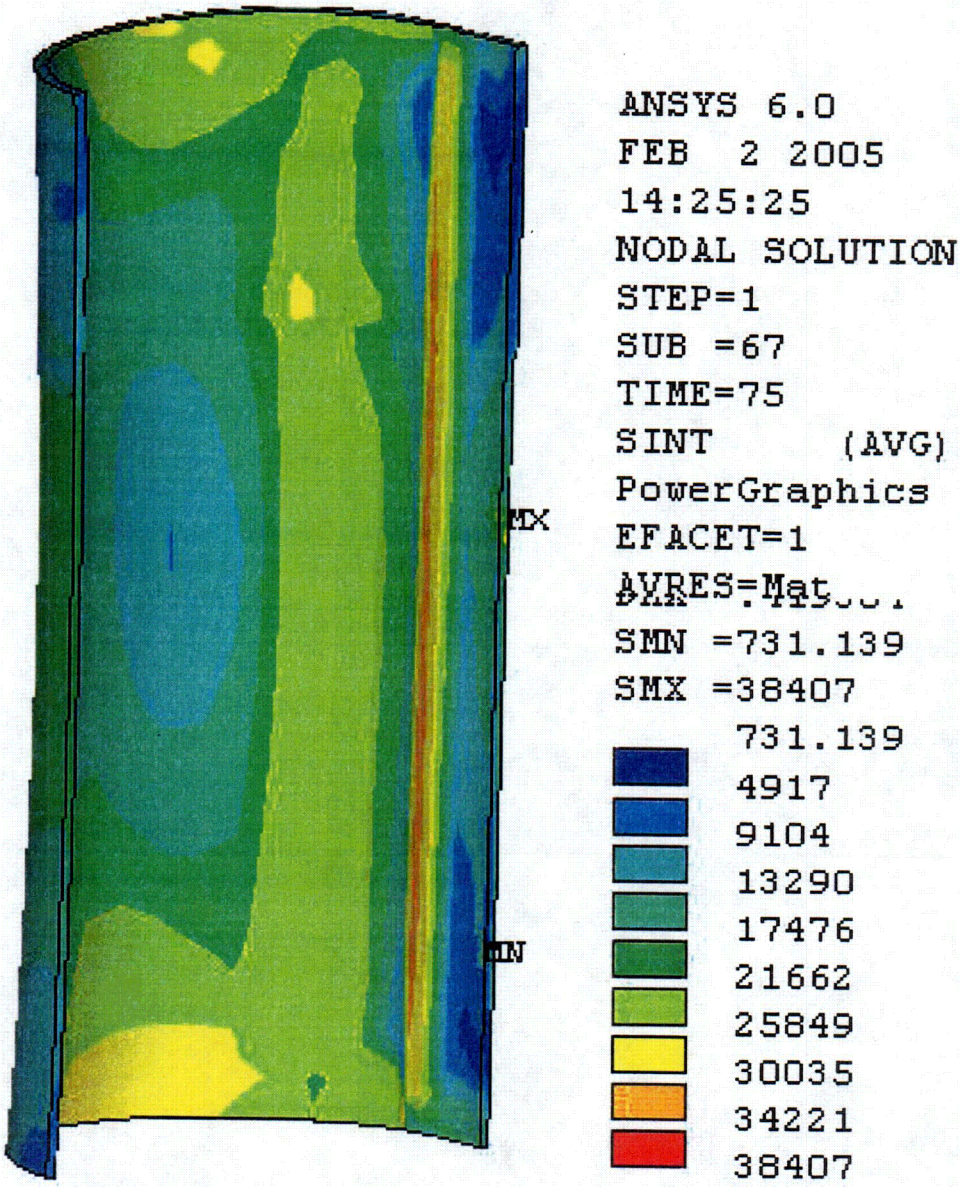

Figure 3-30
Outer Shell Stress Intensity Plot (Load Case 2)

C22

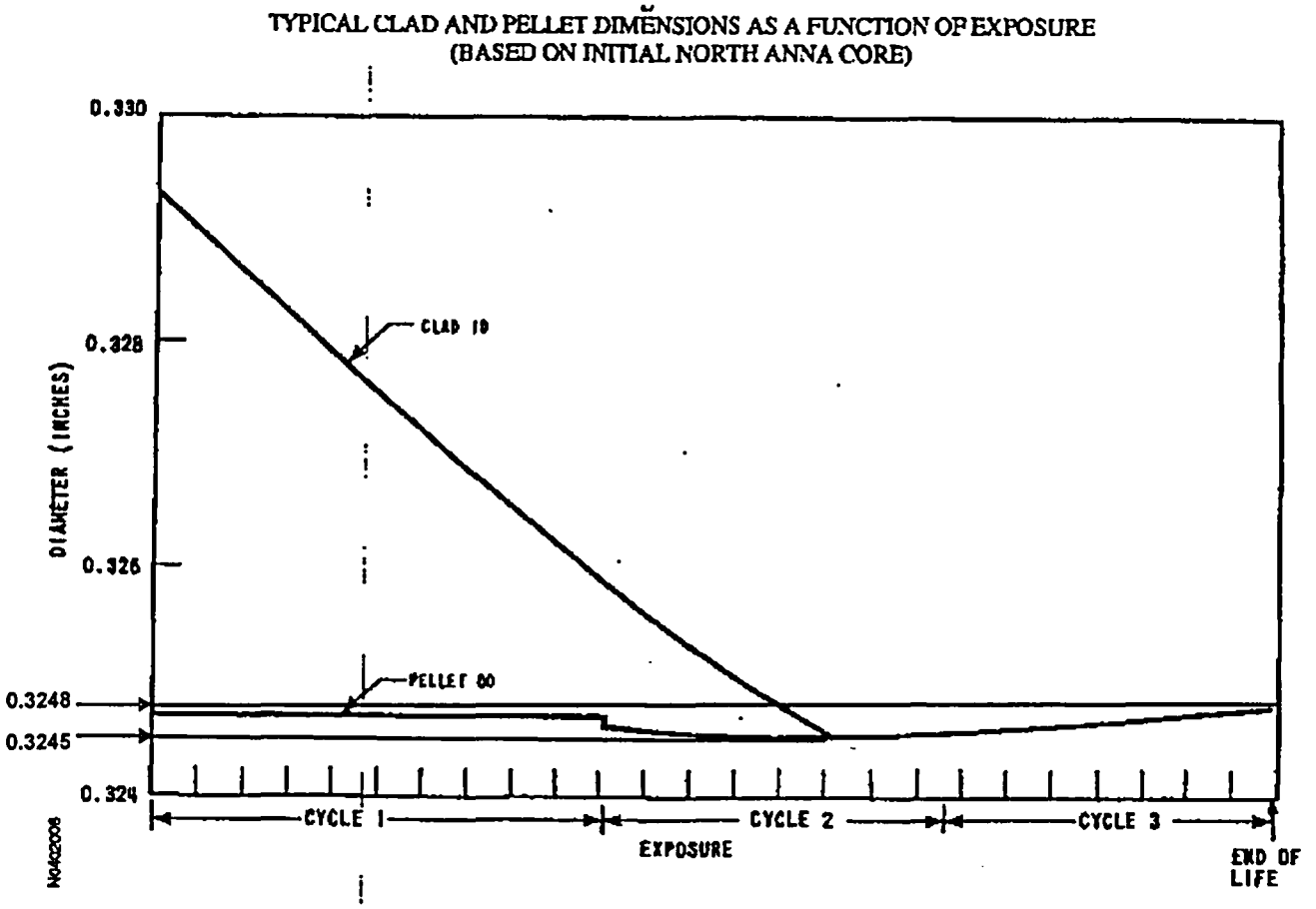

Figure 3-31
Typical Clad and Pellet Dimensions As A Function of Exposure

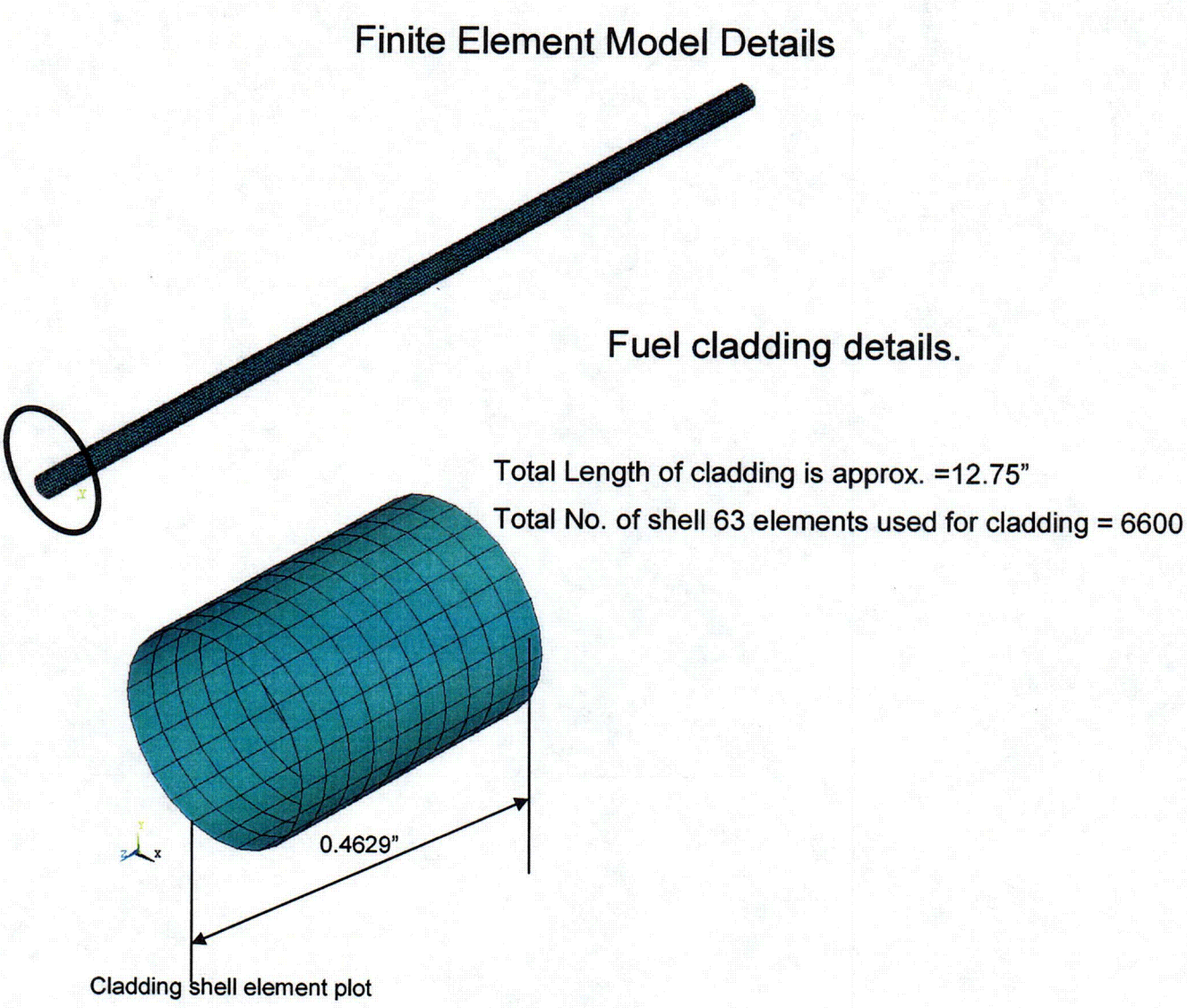

Figure 3-32
Finite Element Model of Cladding

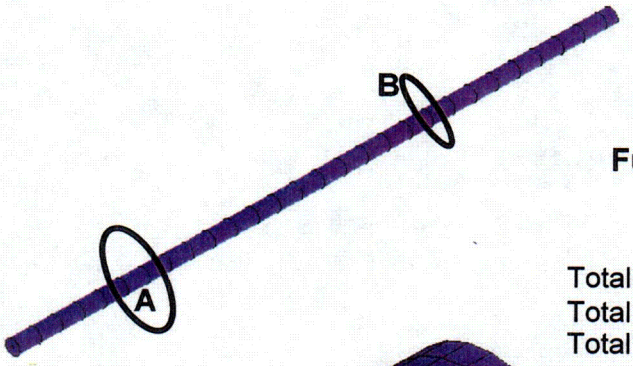

Fuel Pellet details.

Total no. of pellets =27.5
Total Length of pellets is approx. =12.75"
Total No. of solid 45 elements used for the Pellets= 33000

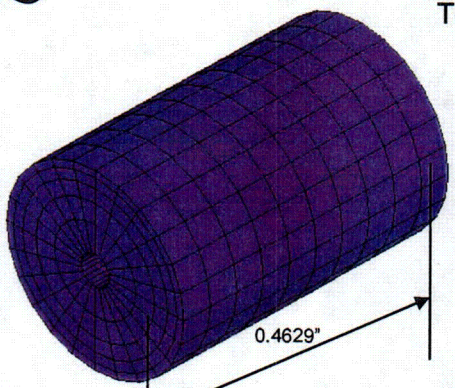

Pellet solid element plot for single pellet

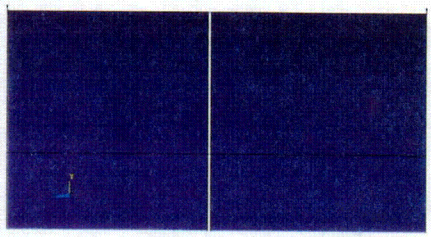

Total axial gap elements (Contact 52) used between the adjacent gaps in each pellet is 144.

Figure 3-33
Finite Element Model of Fuel Pellets

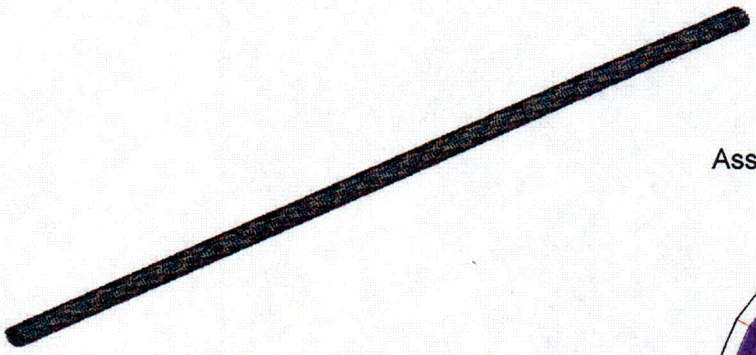

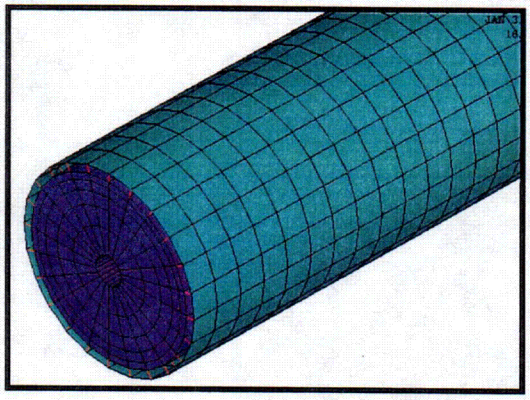

Assembly Details

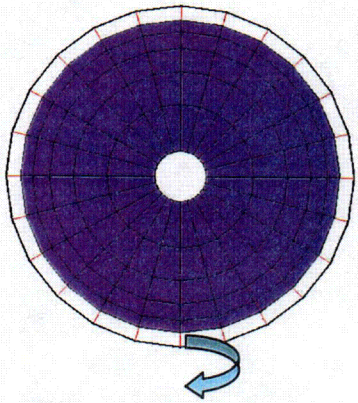

Total radial gap element (contact 52) used between the pellets and the cladding is 7272 for the entire length of approx 12.75" model.

Figure 3-34
Finite Element Model of Cladding and Pellets

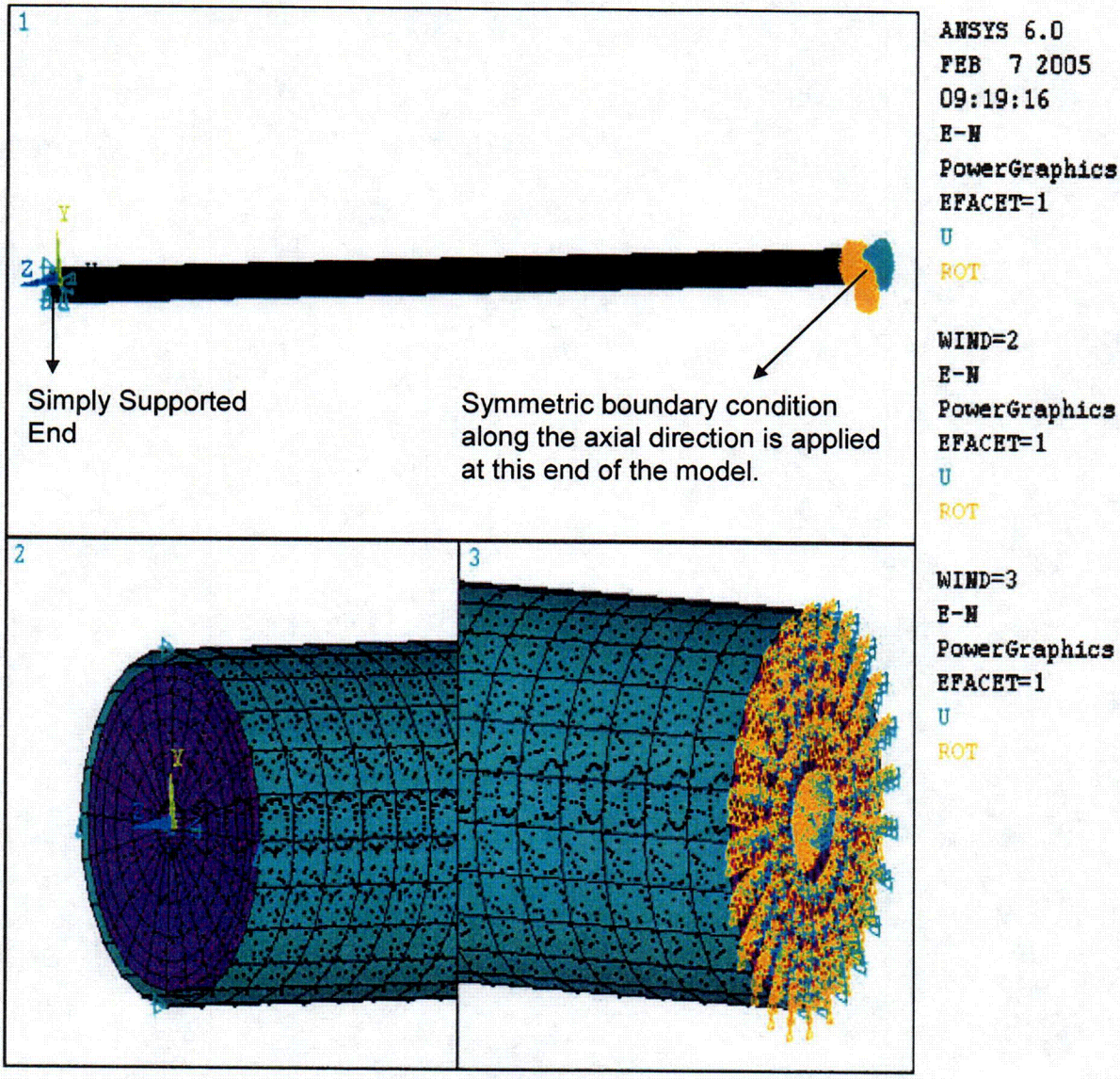

Figure 3-35
Boundary Conditions of Cladding/ Fuel Pellets Finite Element Model

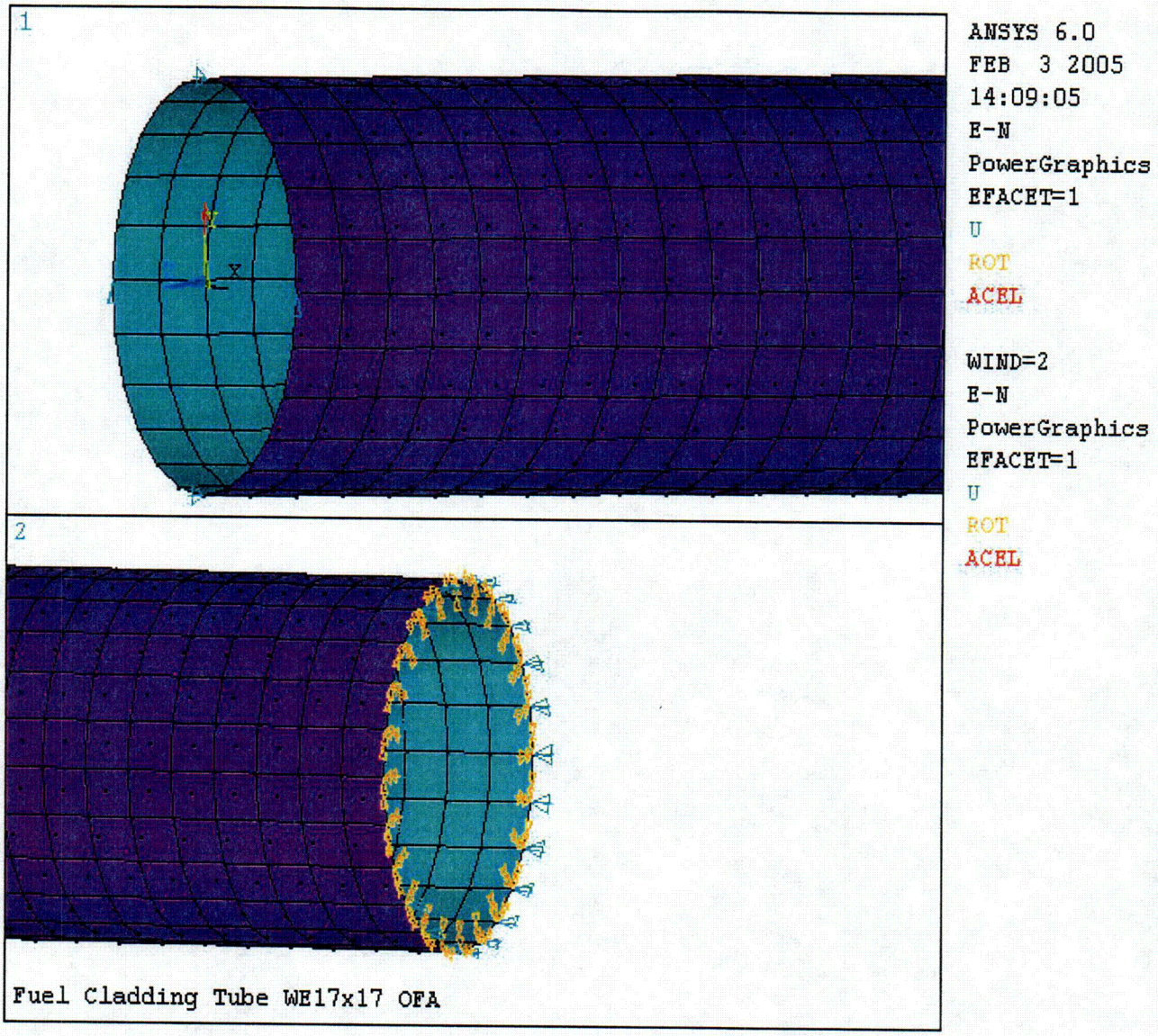

Figure 3-36
Boundary Conditions of Cladding Finite Element Model

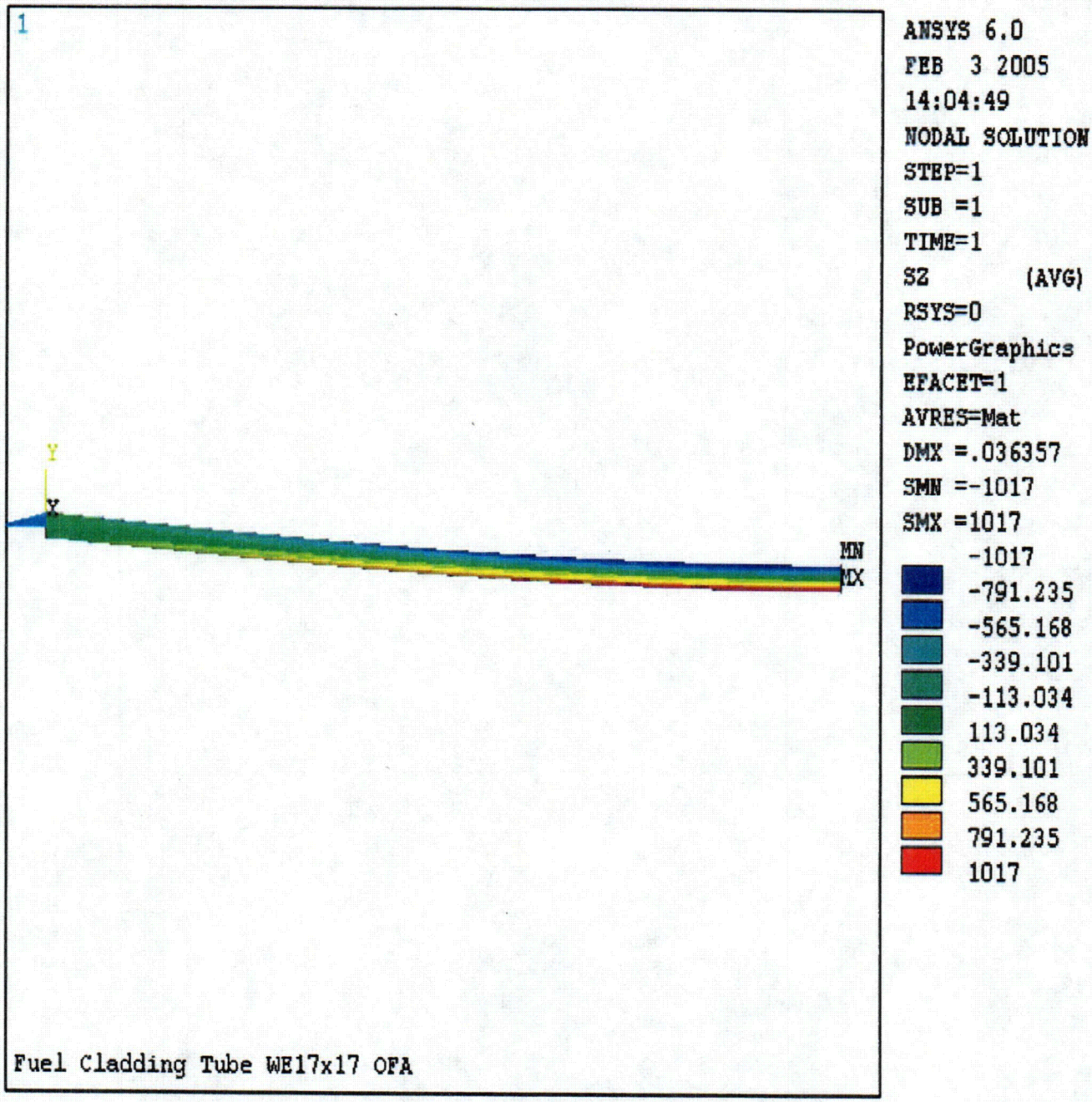

Figure 3-37
Cladding Stress Distribution
(Pellets are not Included in the Model)

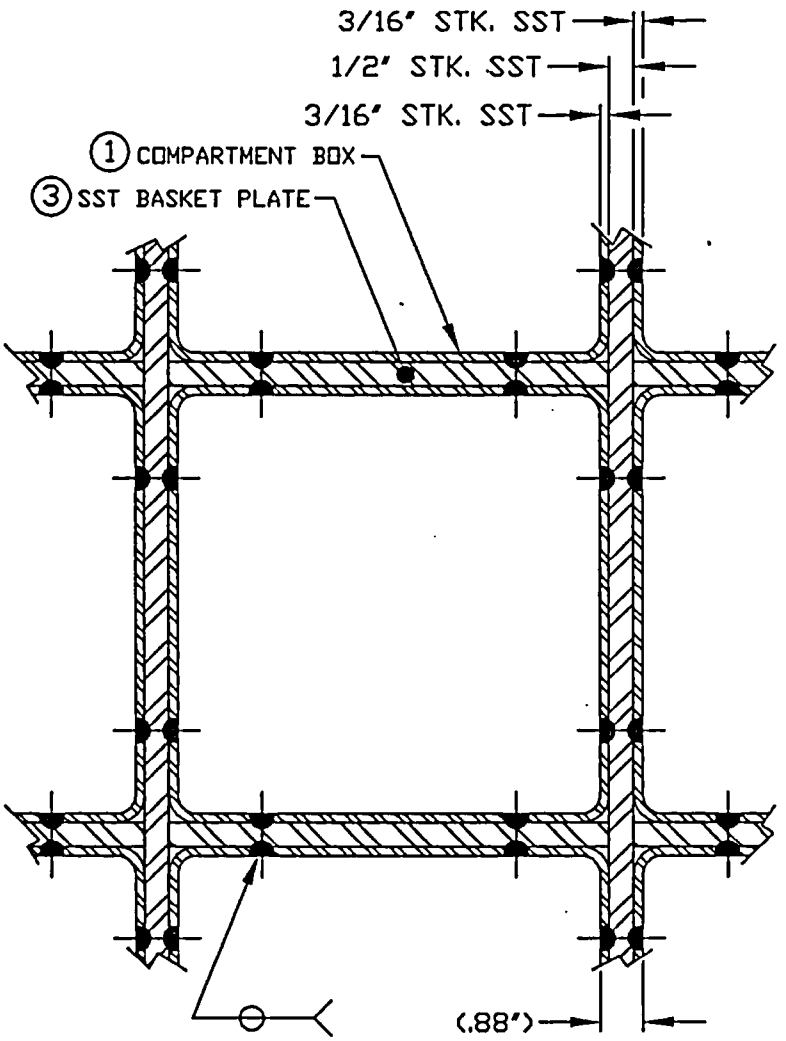

Figure 3-8
32PTH Basket Weld

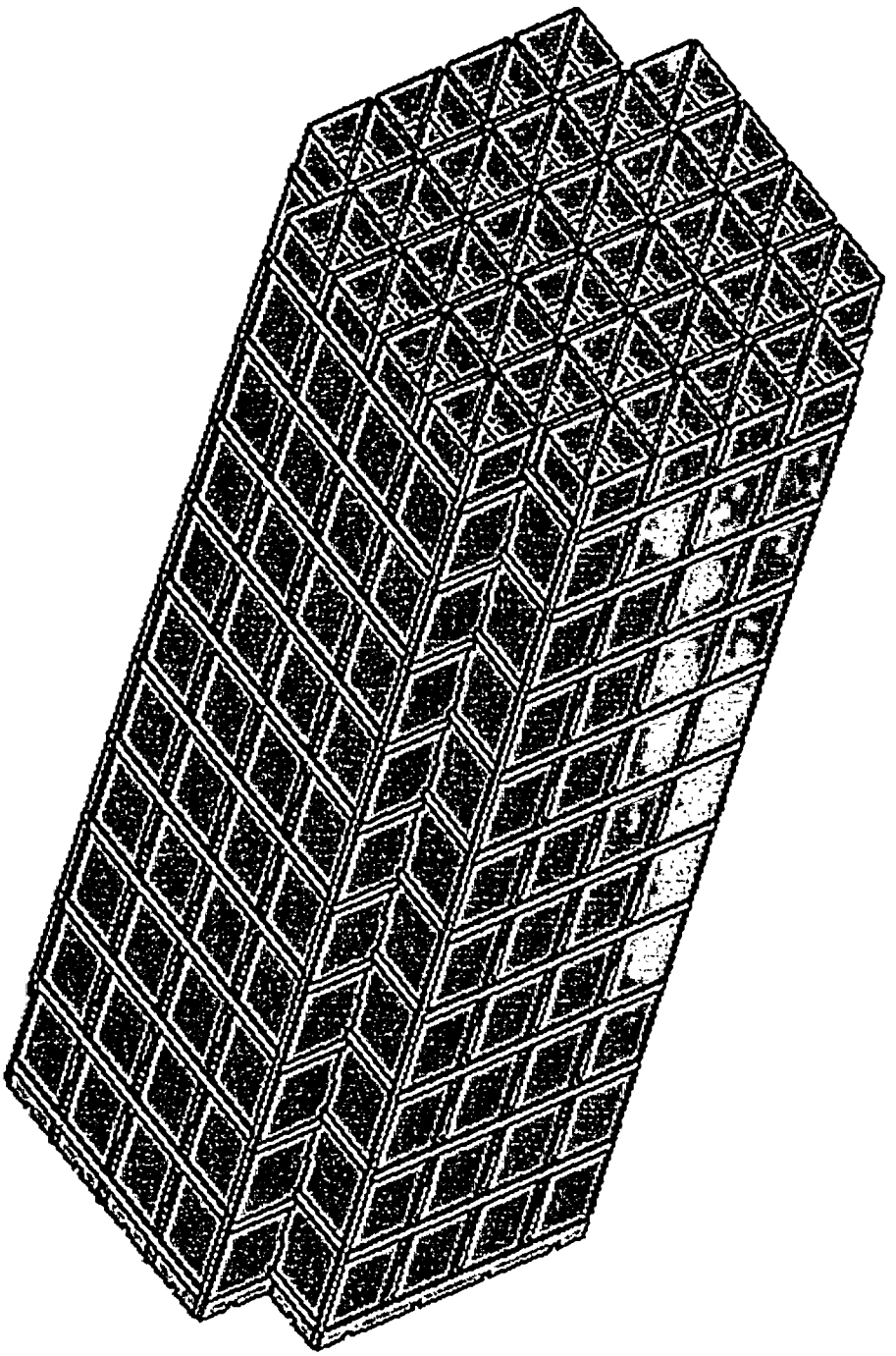

Figure 3-9
32PTH Basket SS Tube Assembly

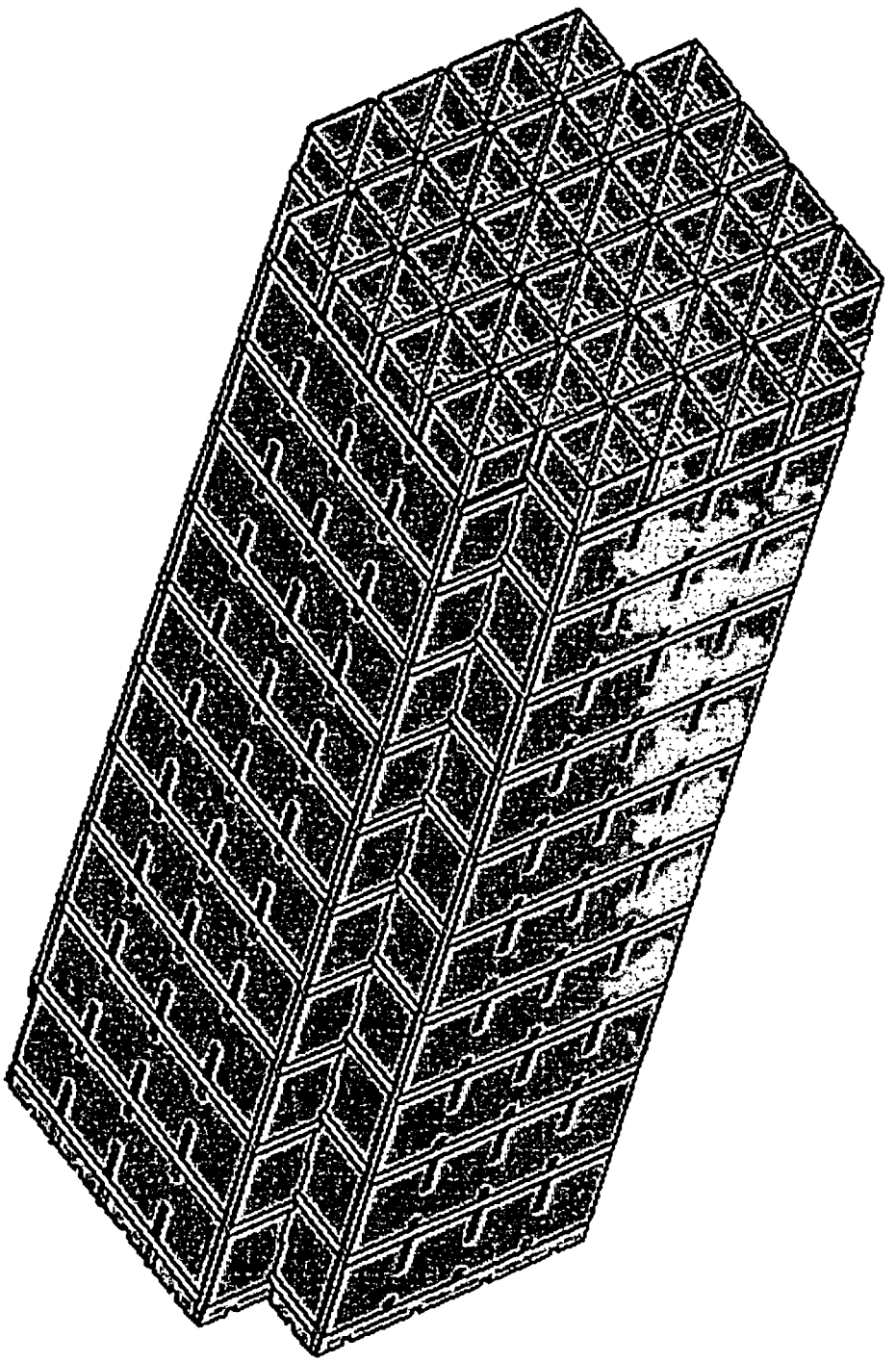

Figure 3-10
32PTH Basket SS Tube with Aluminum Plate

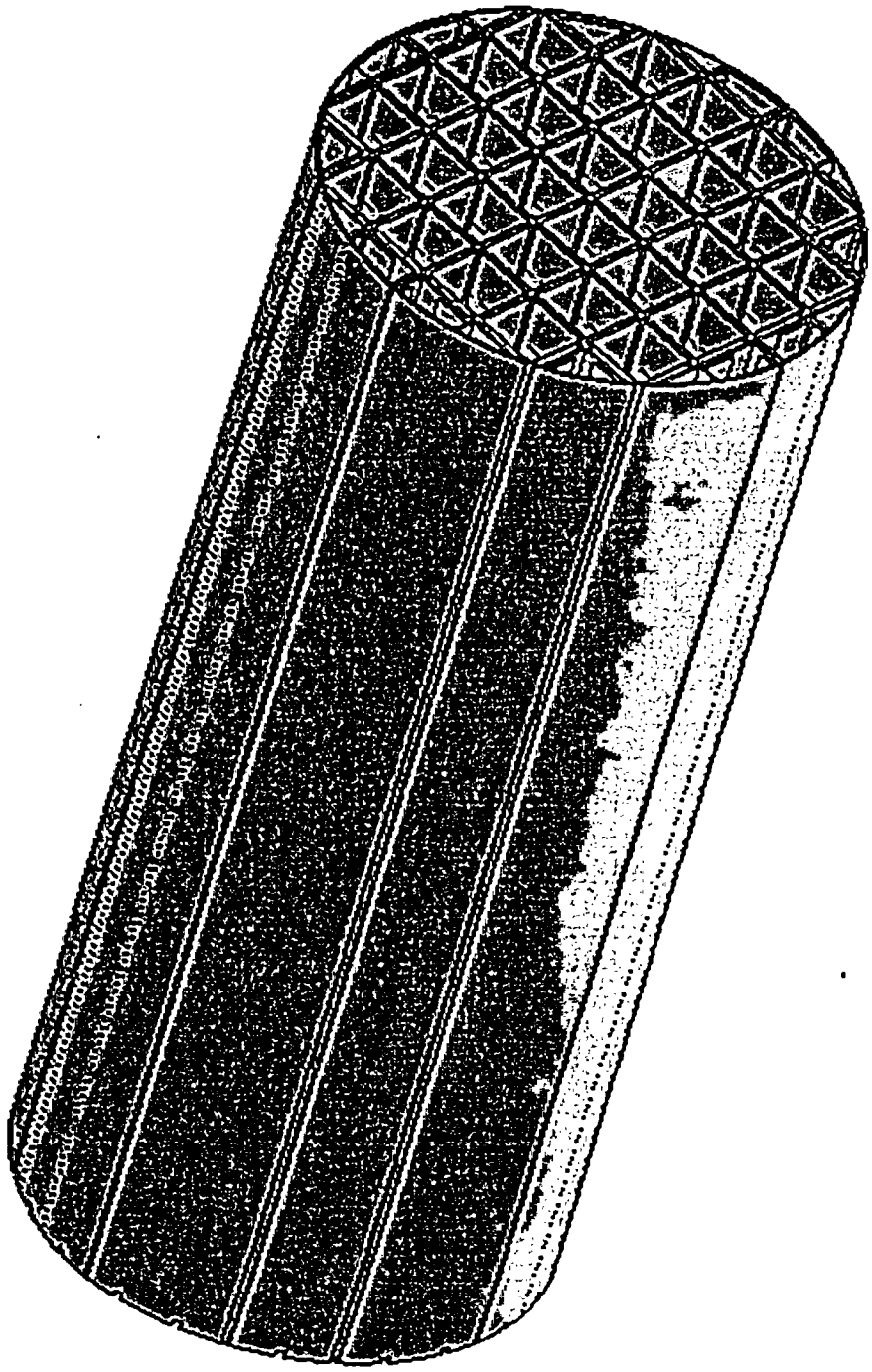

Figure 3-11
32PTH Basket with SS Rails

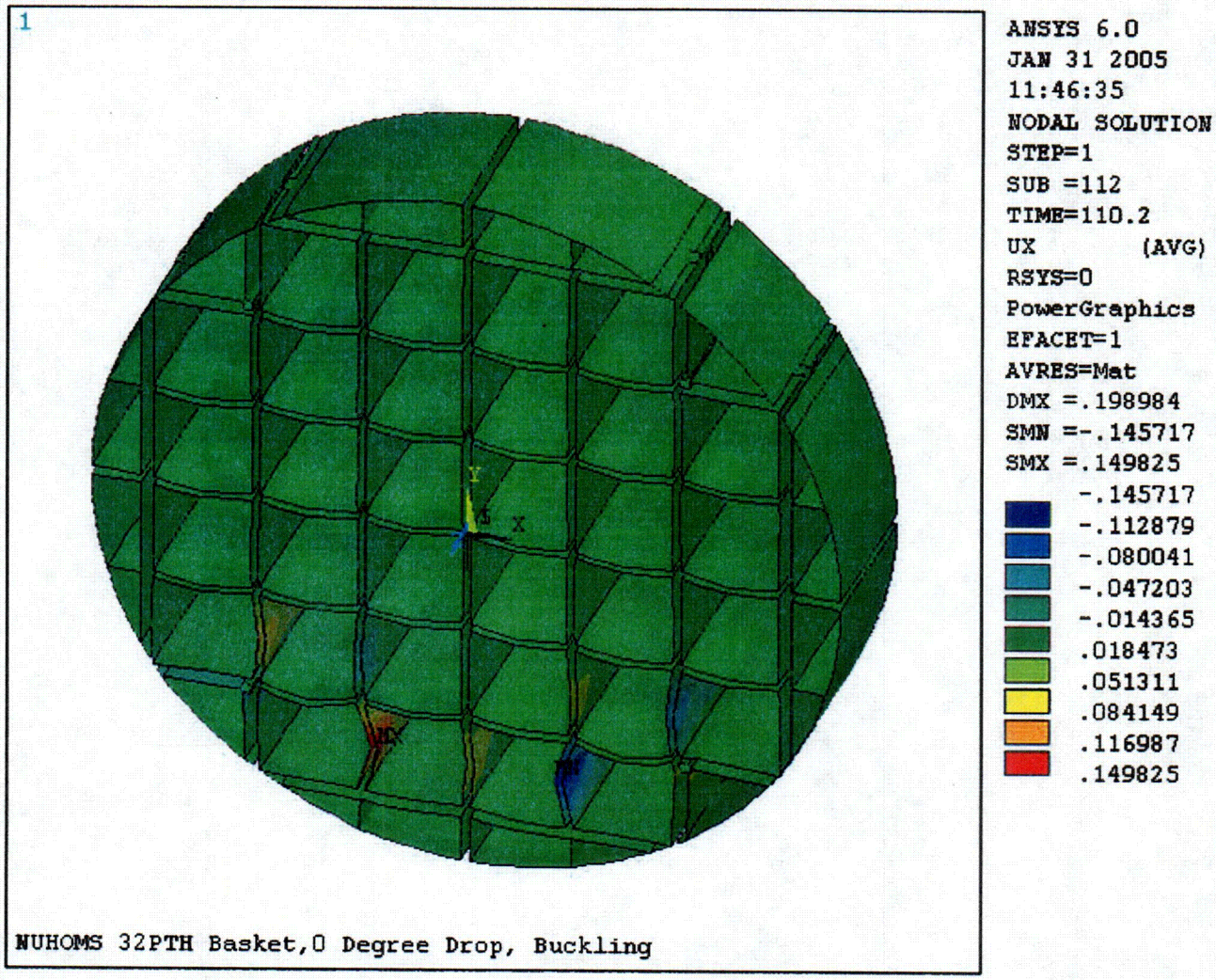

Figure 3-12
0^0 Drop Basket Deformation Plot

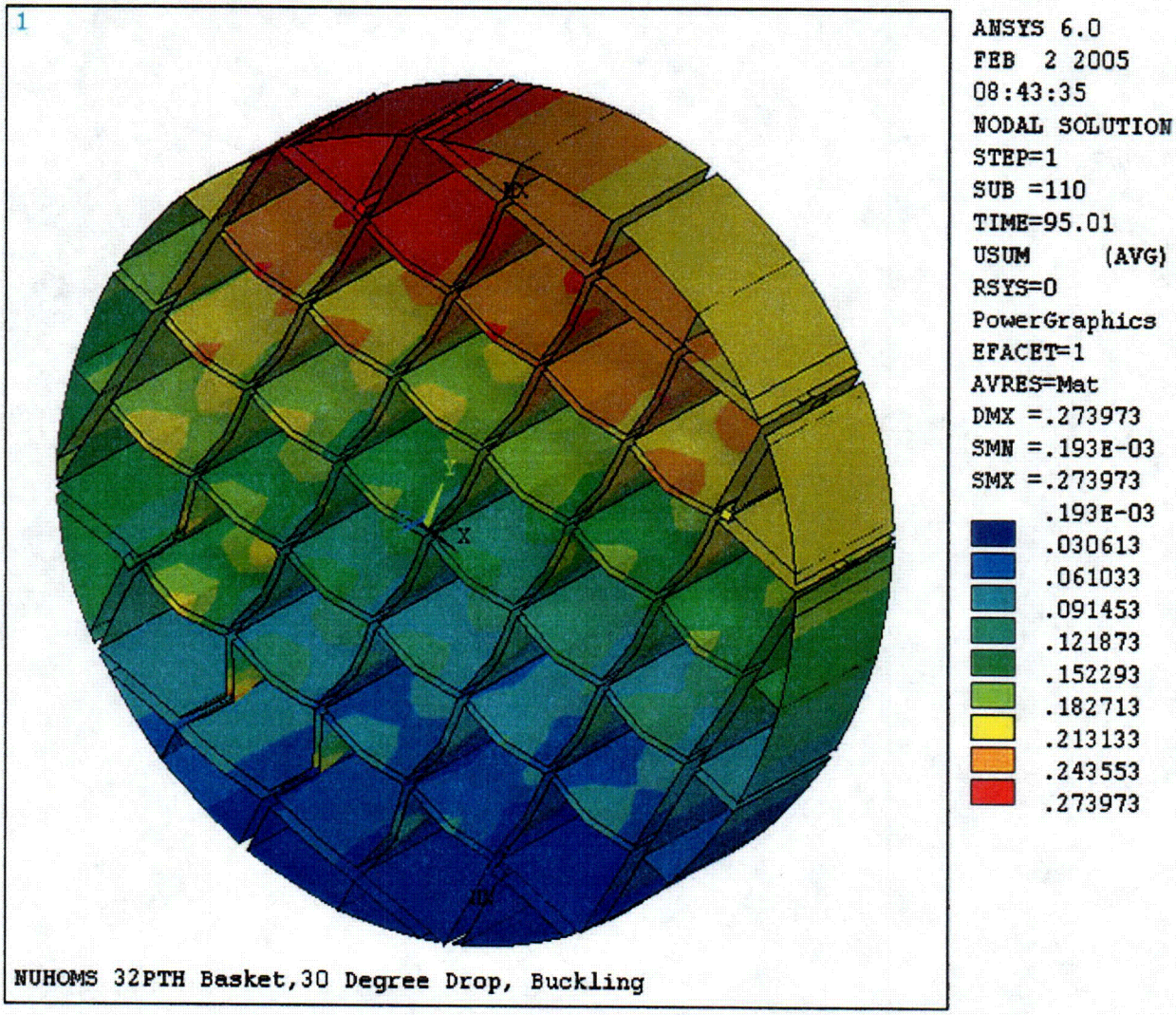

Figure 3-13
30^0 Drop Basket Deformation Plot

C30

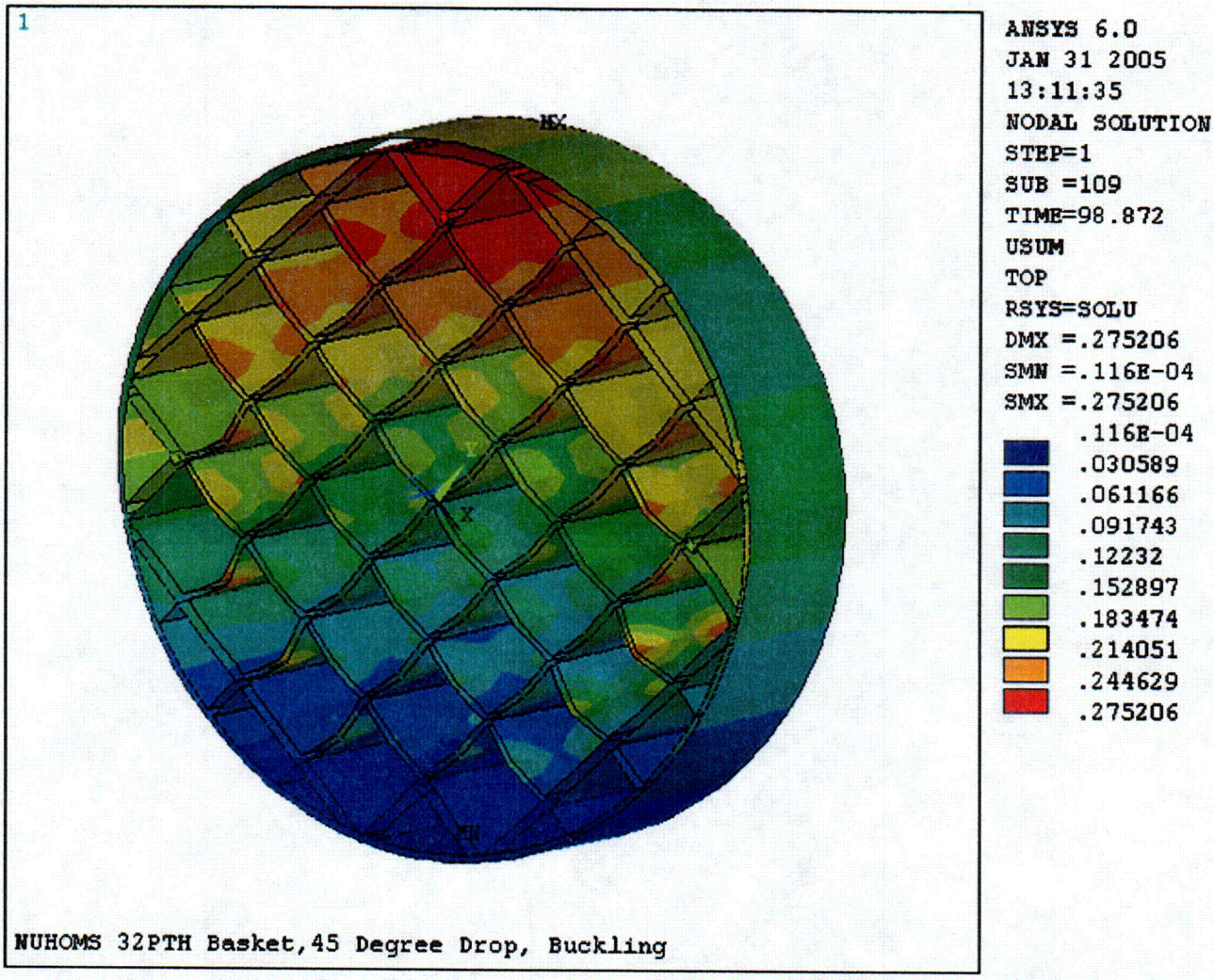

Figure 3-14
45^0 Drop Basket Deformation Plot

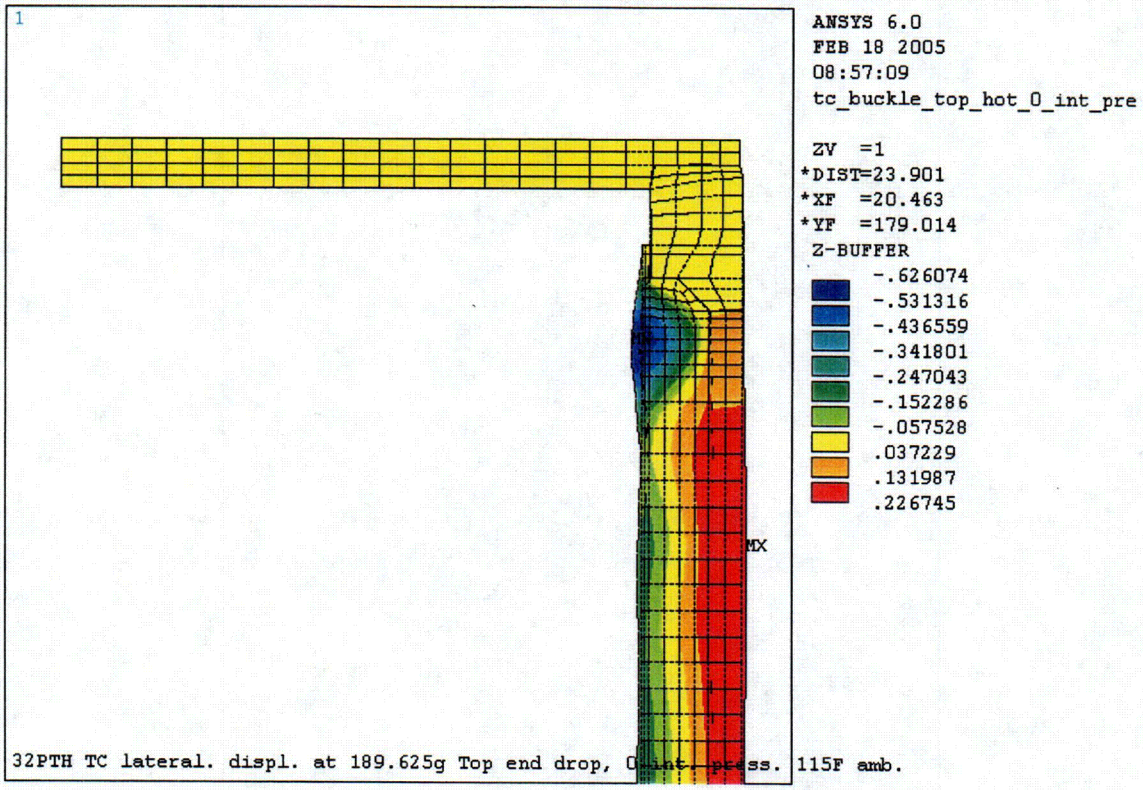

Figure 3-15
Transfer Cask Top End Drop Deformation Plot (at 189.625g)

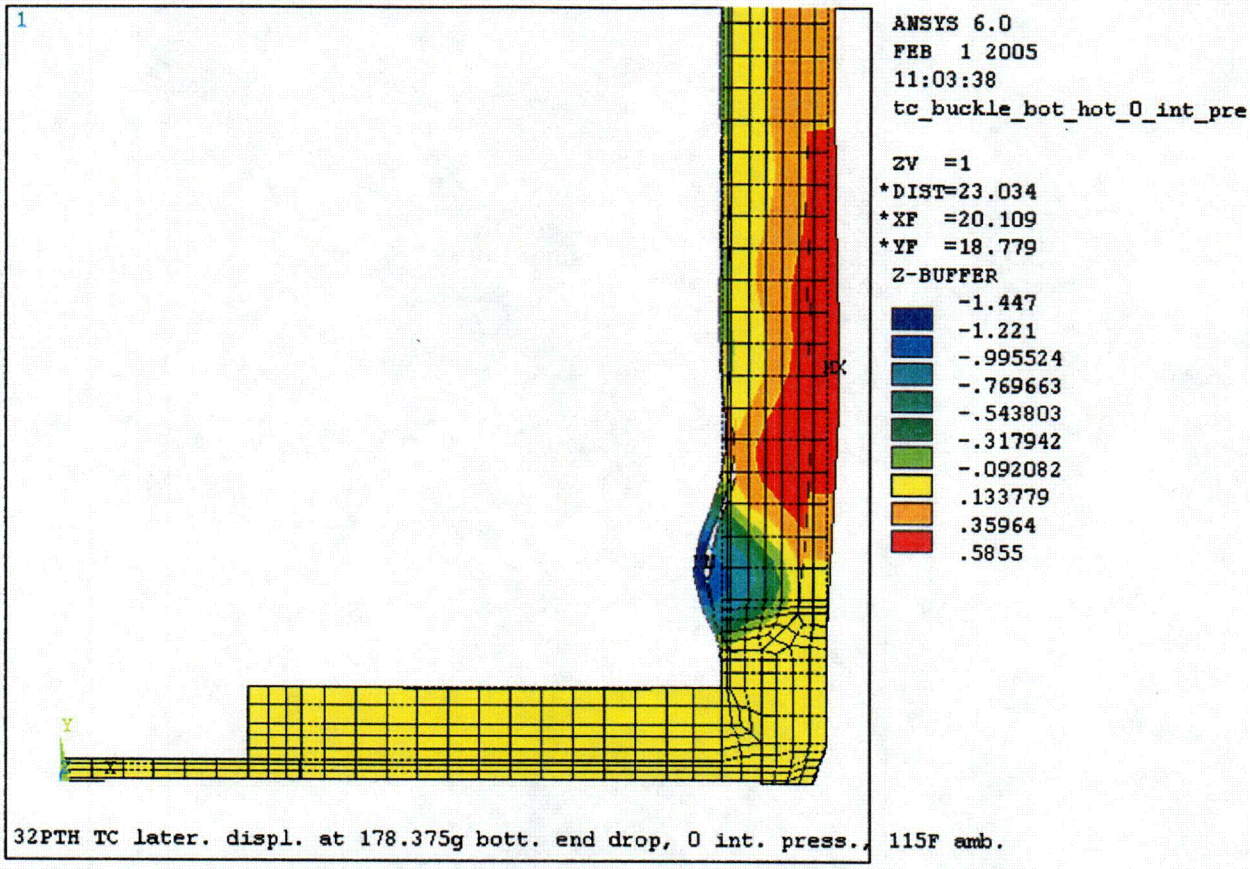

Figure 3-16
Transfer Cask Bottom End Drop Deformation Plot (at 178.375g)

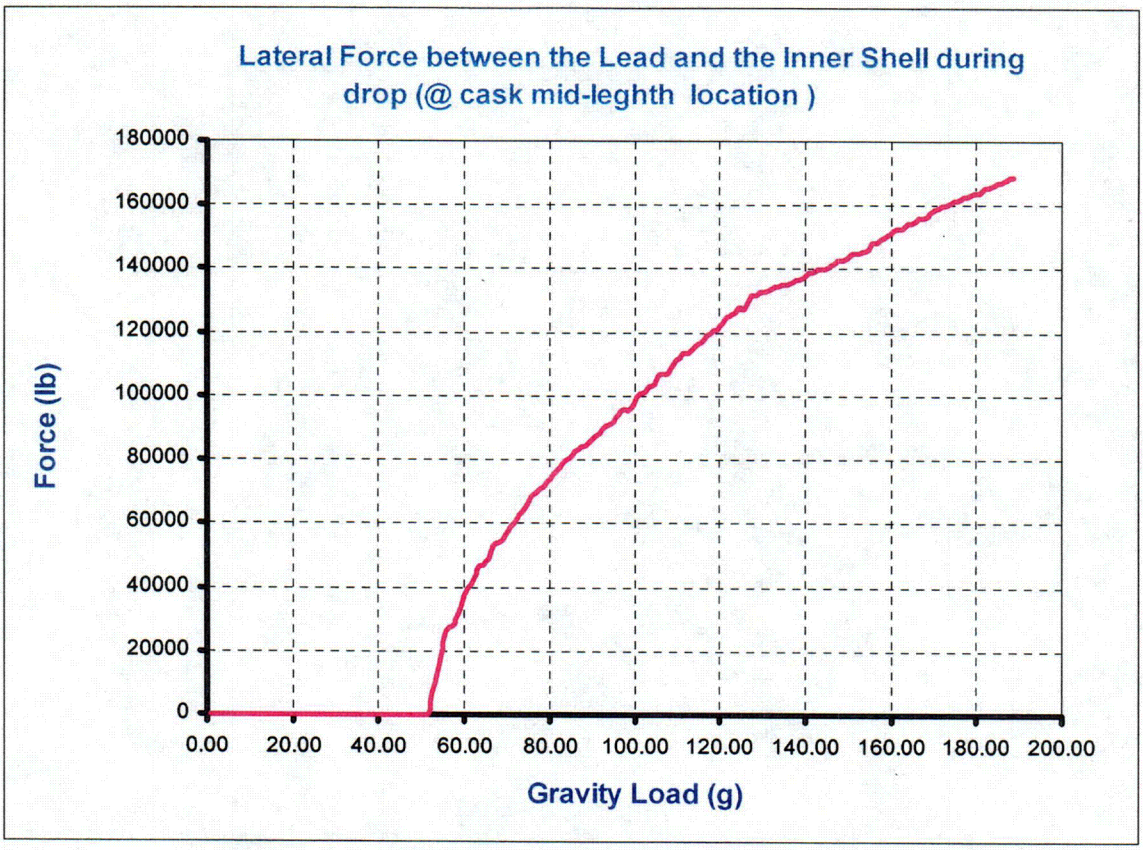

Figure 3-17
Lateral Force Exerted on Inner Shell (Transfer Cask Top End Drop)

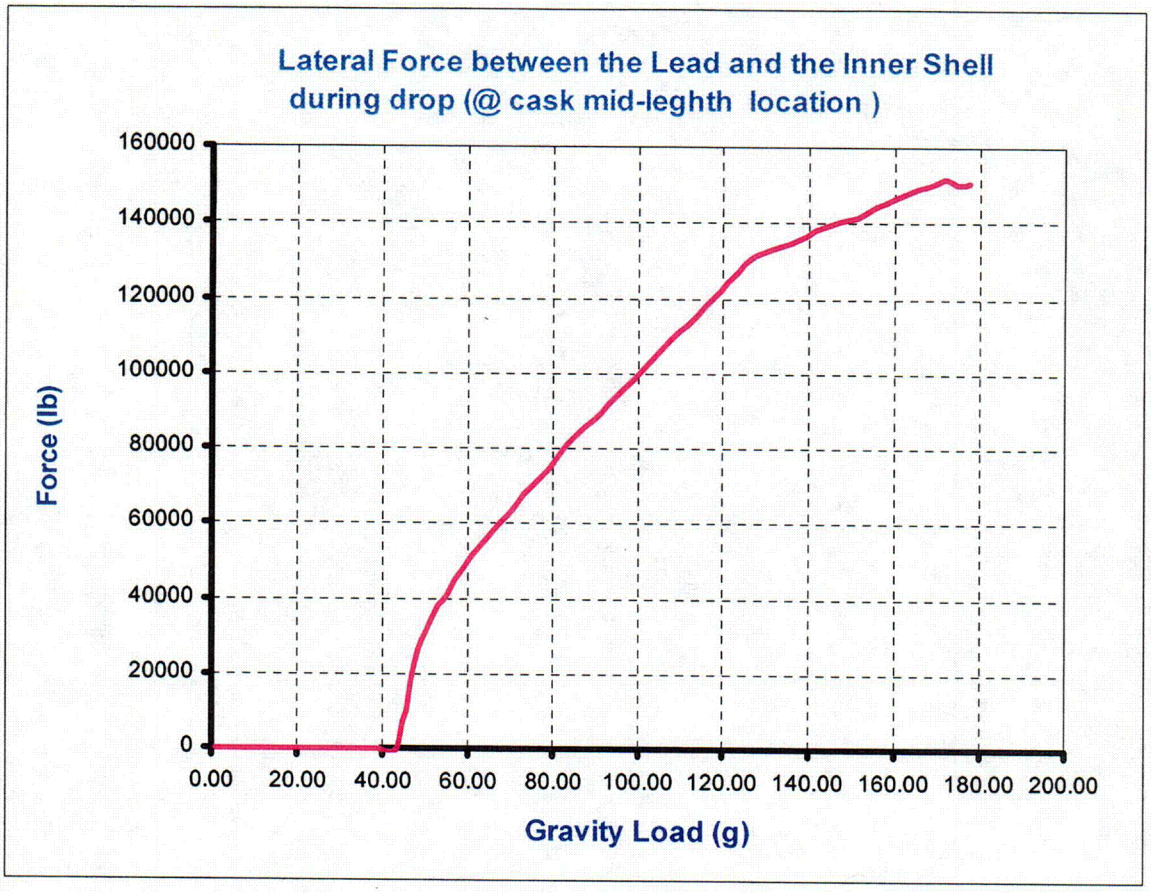

Figure 3-18
Lateral Force Exerted on Inner Shell (Transfer Cask Bottom End Drop)

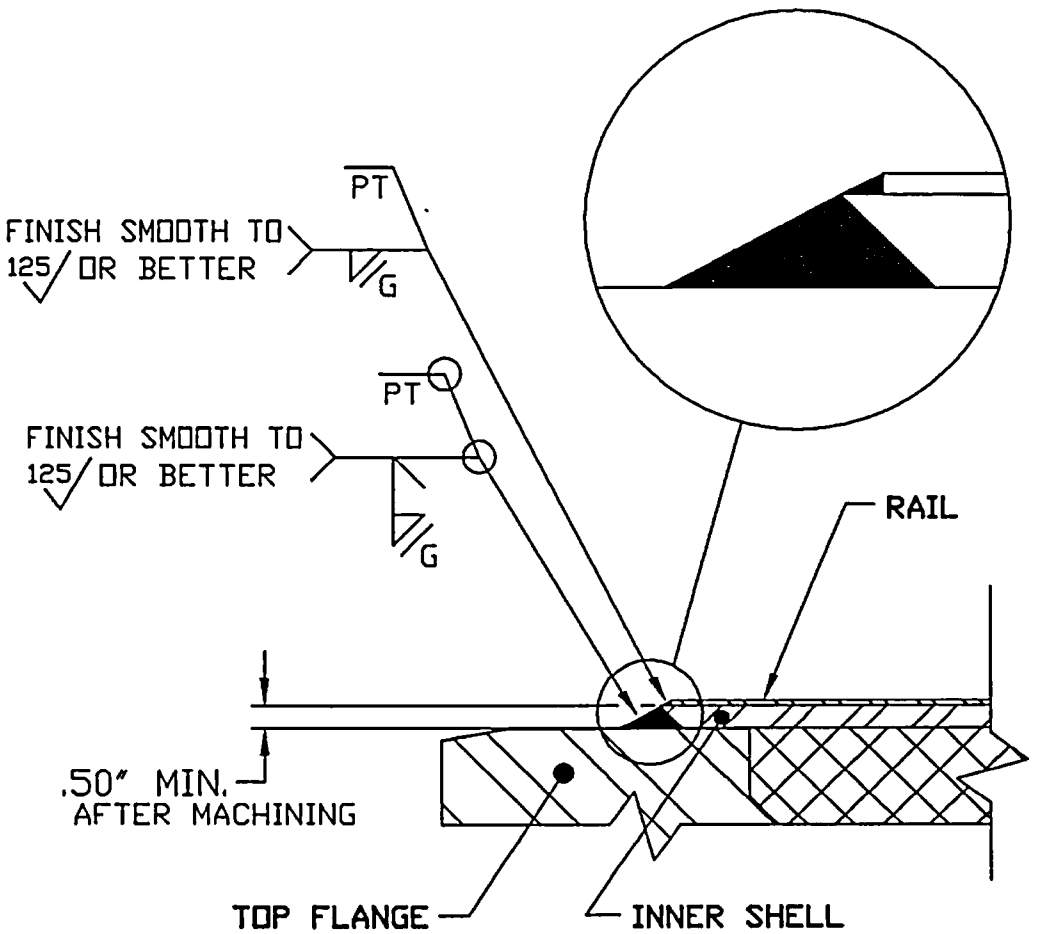

Figure 3-19
Transfer Cask Inner Shell & Flange Weld Details

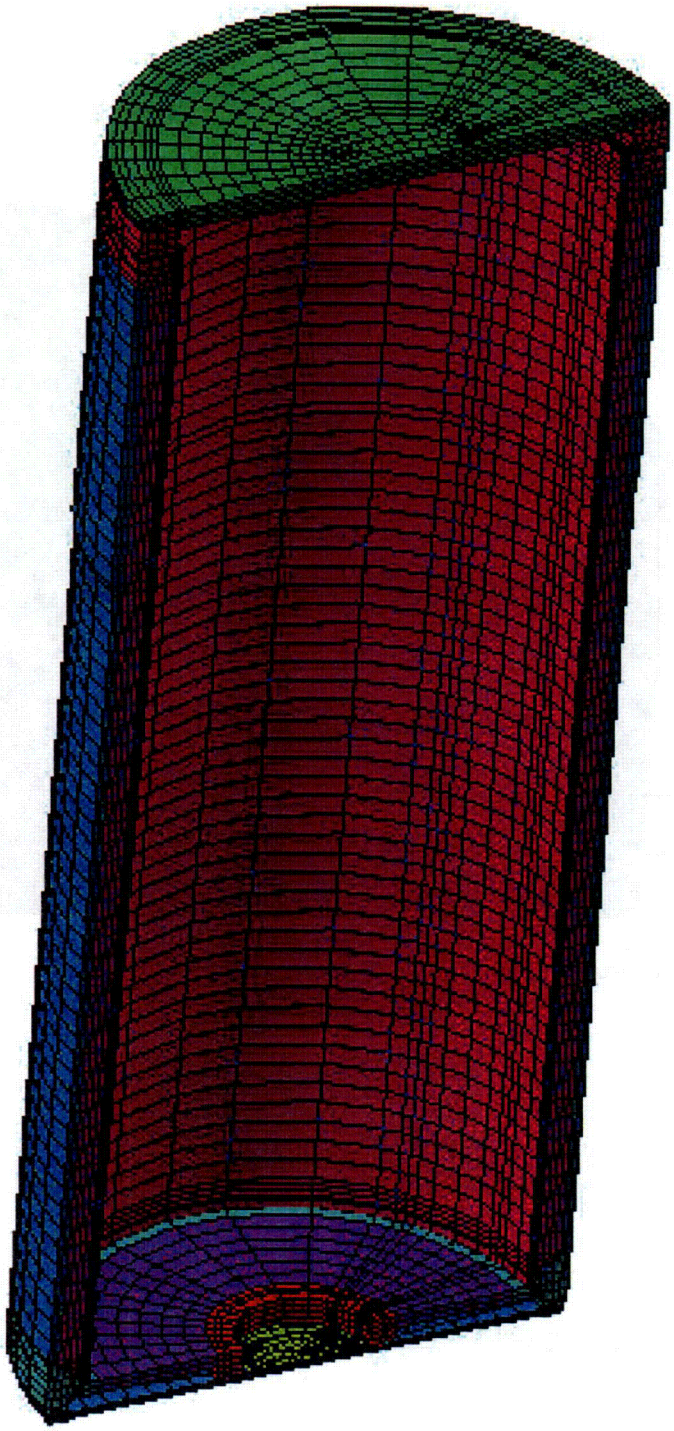

Figure 3-20
3D - Model of Transfer Cask

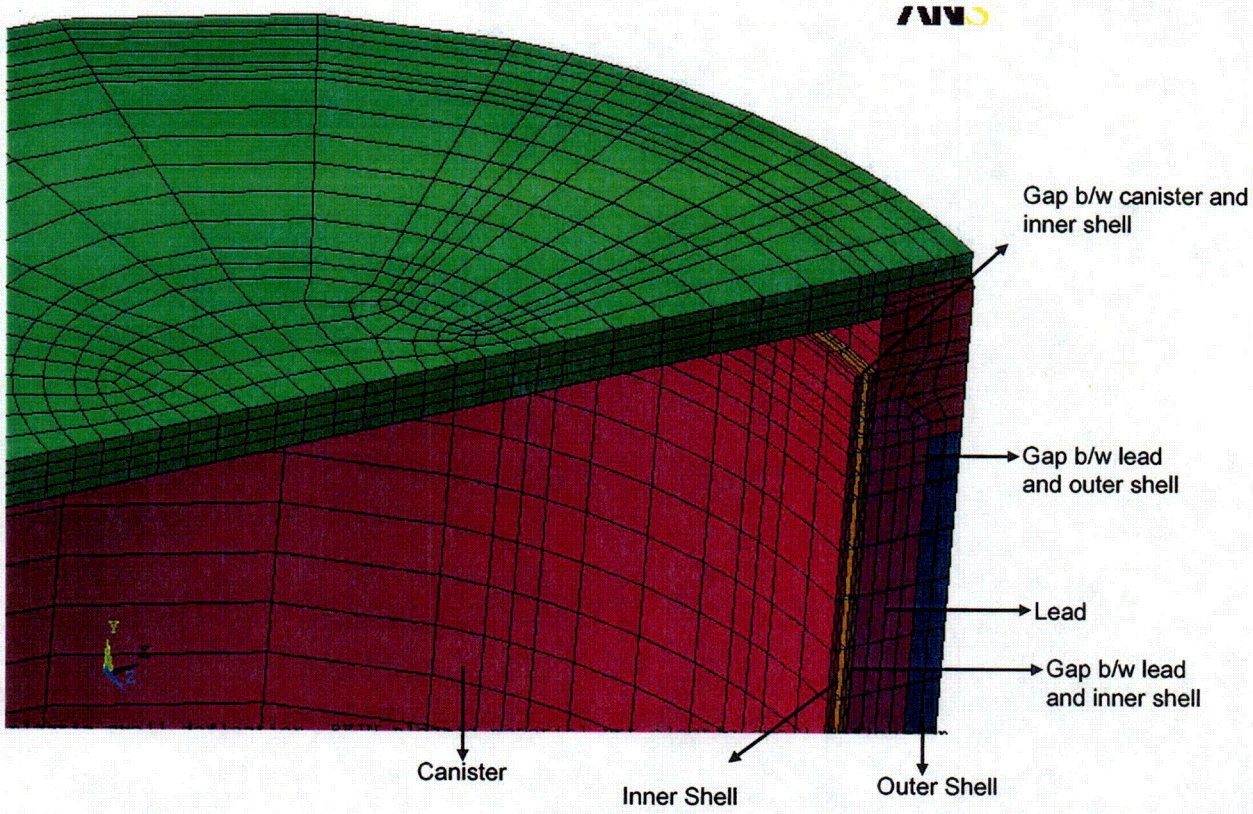

Figure 3-21
Canister/Cask Top Cover/Flange/CONTACT 52 Element Representation

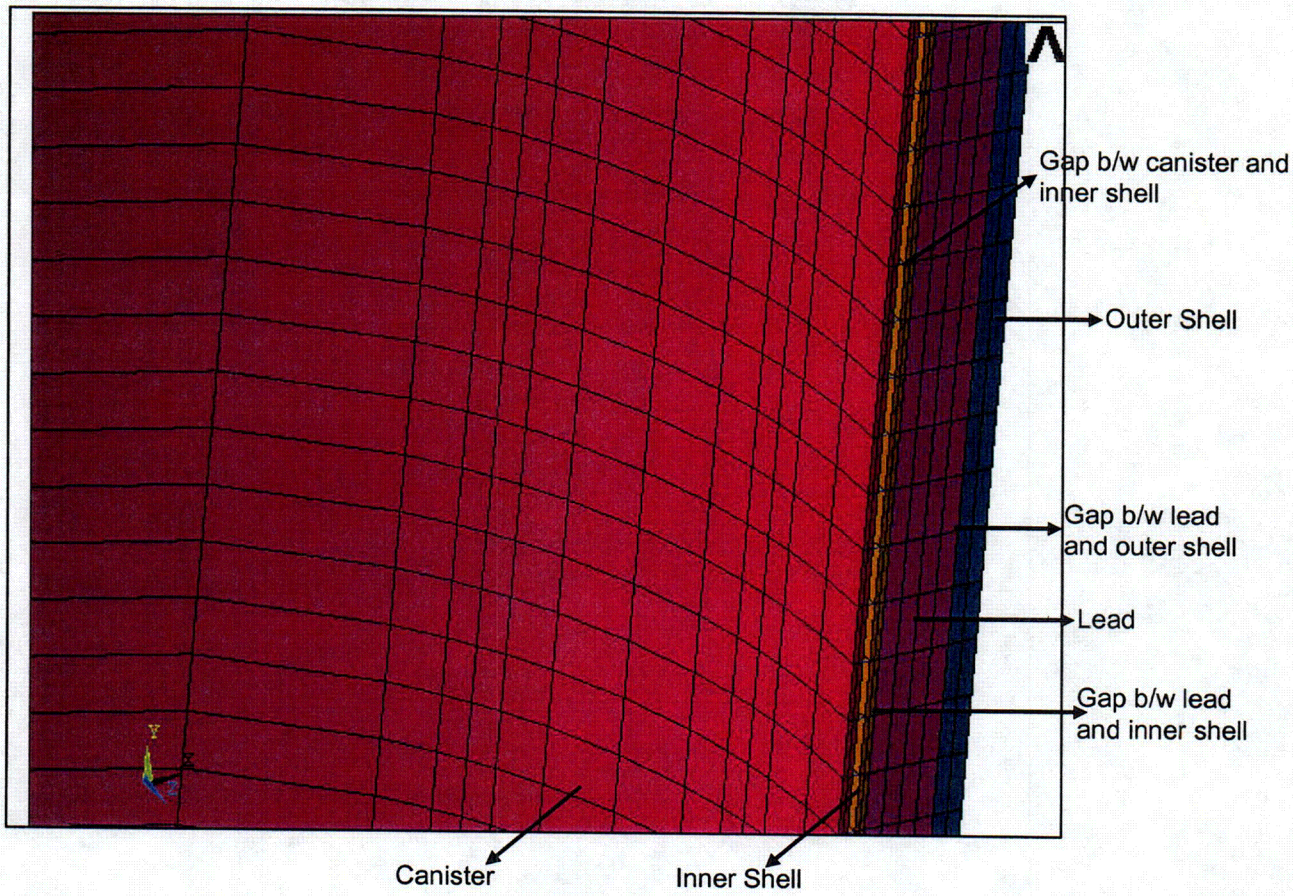

Figure 3-22
Canister/ Cask Shell /Lead /CONTACT 52 Element Representation

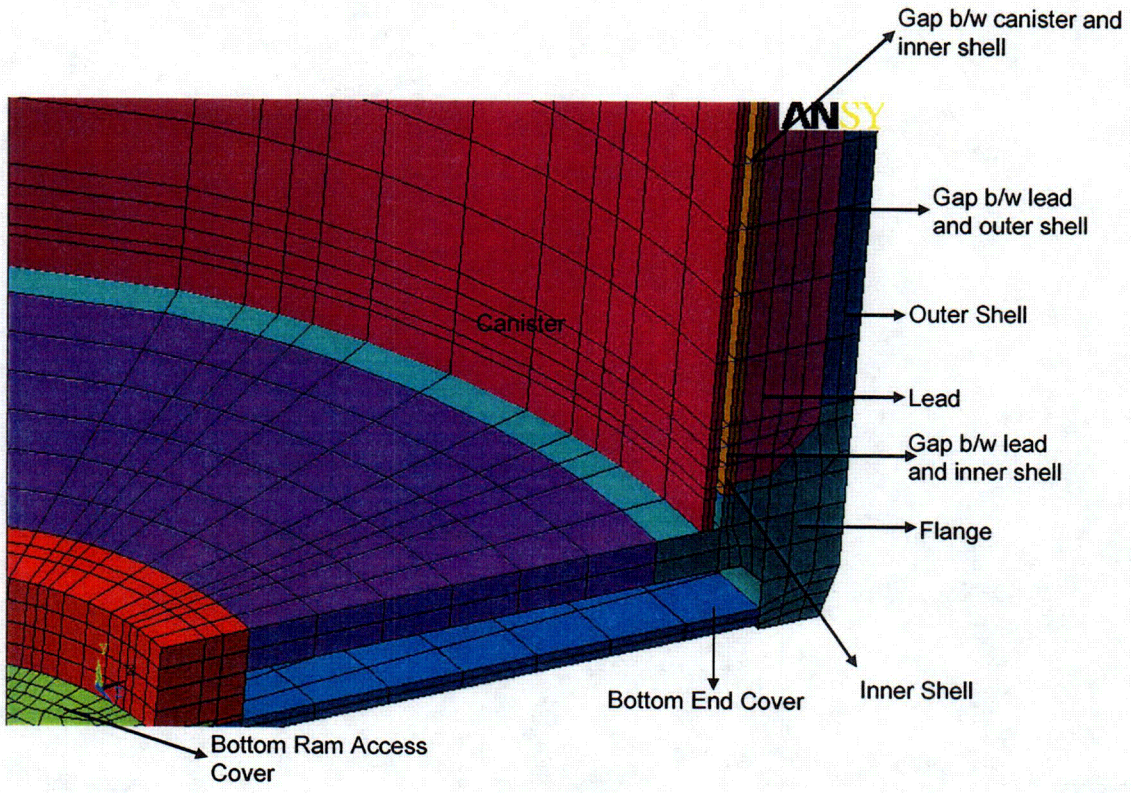

Figure 3-23
Canister/ Cask Bottom Access/Shell/ Flange/ Lead /CONTACT 52 Element Representation

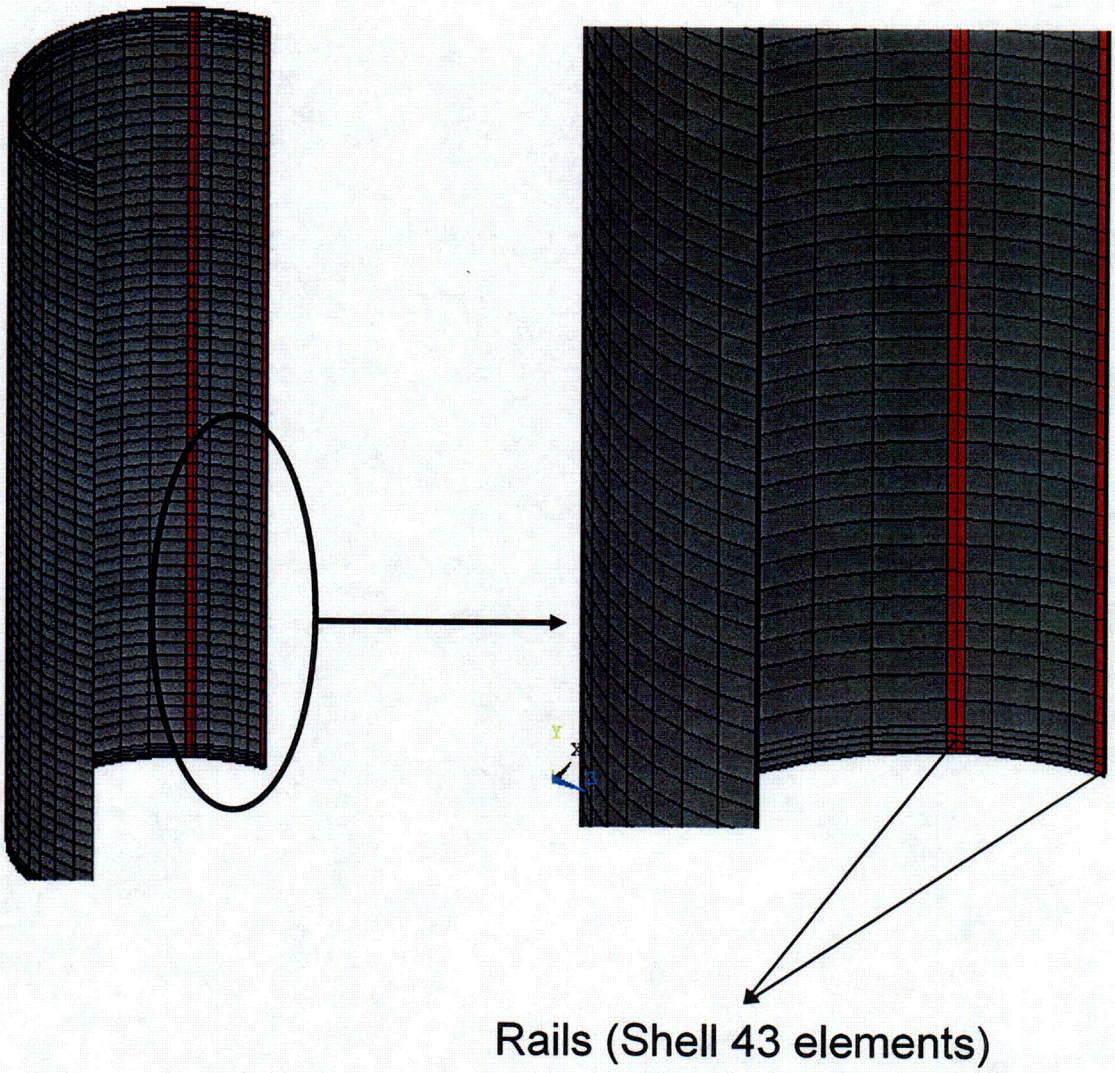

Figure 3-24
Transfer Cask Inner Shell & Rails

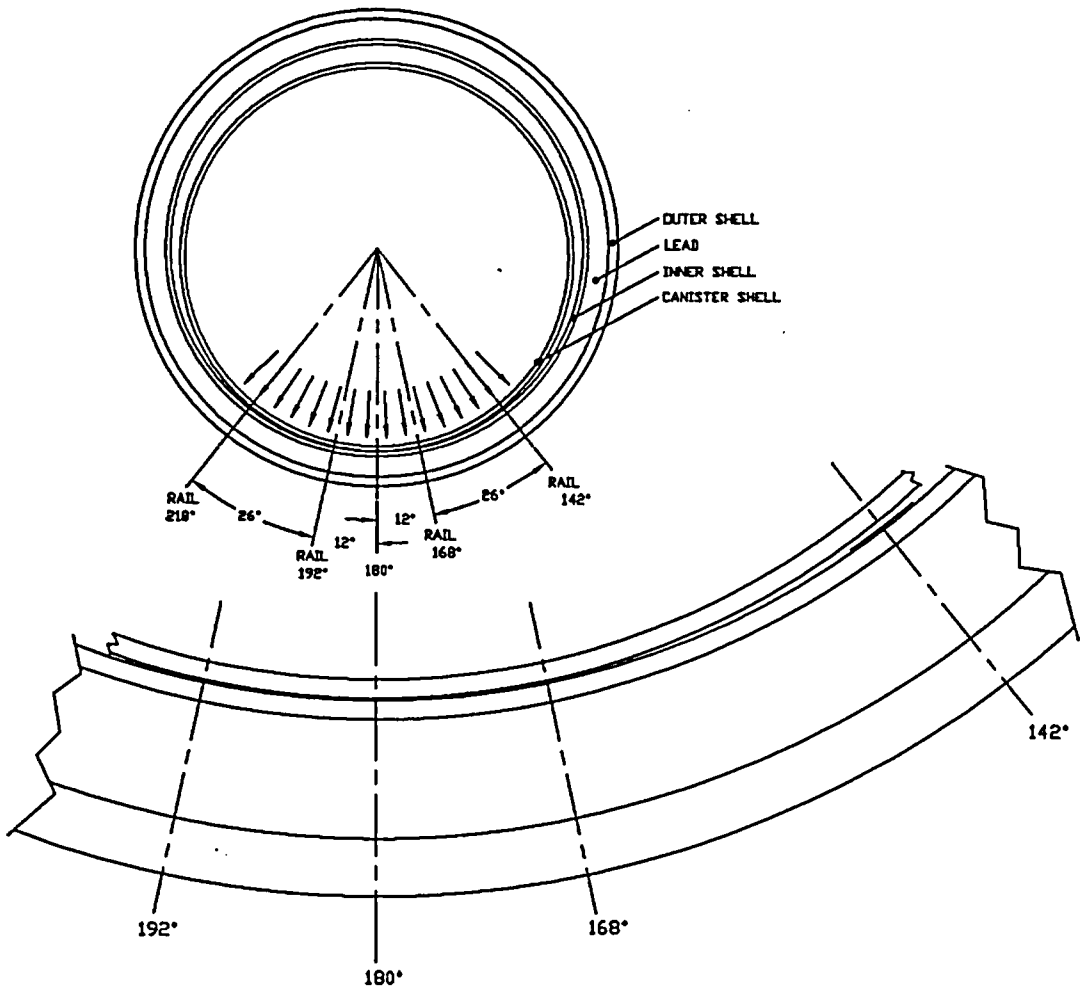

Figure 3-25
Drop Sketch for Initial Impact @ both 168^0 and 192^0 Rails (Load Case 1)

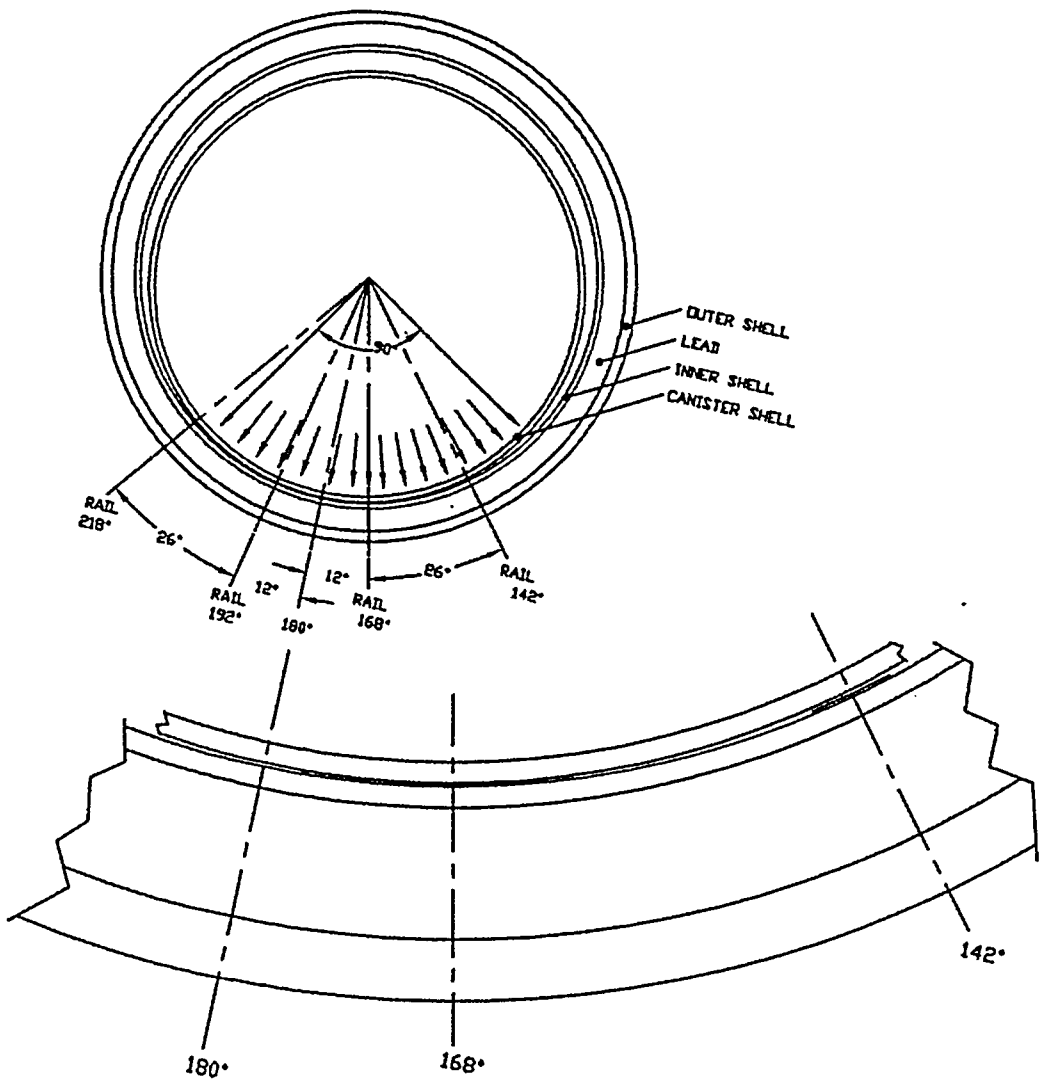

Figure 3-26
Drop Sketch for Initial Impact @ 168°Rail (Load Case 2)

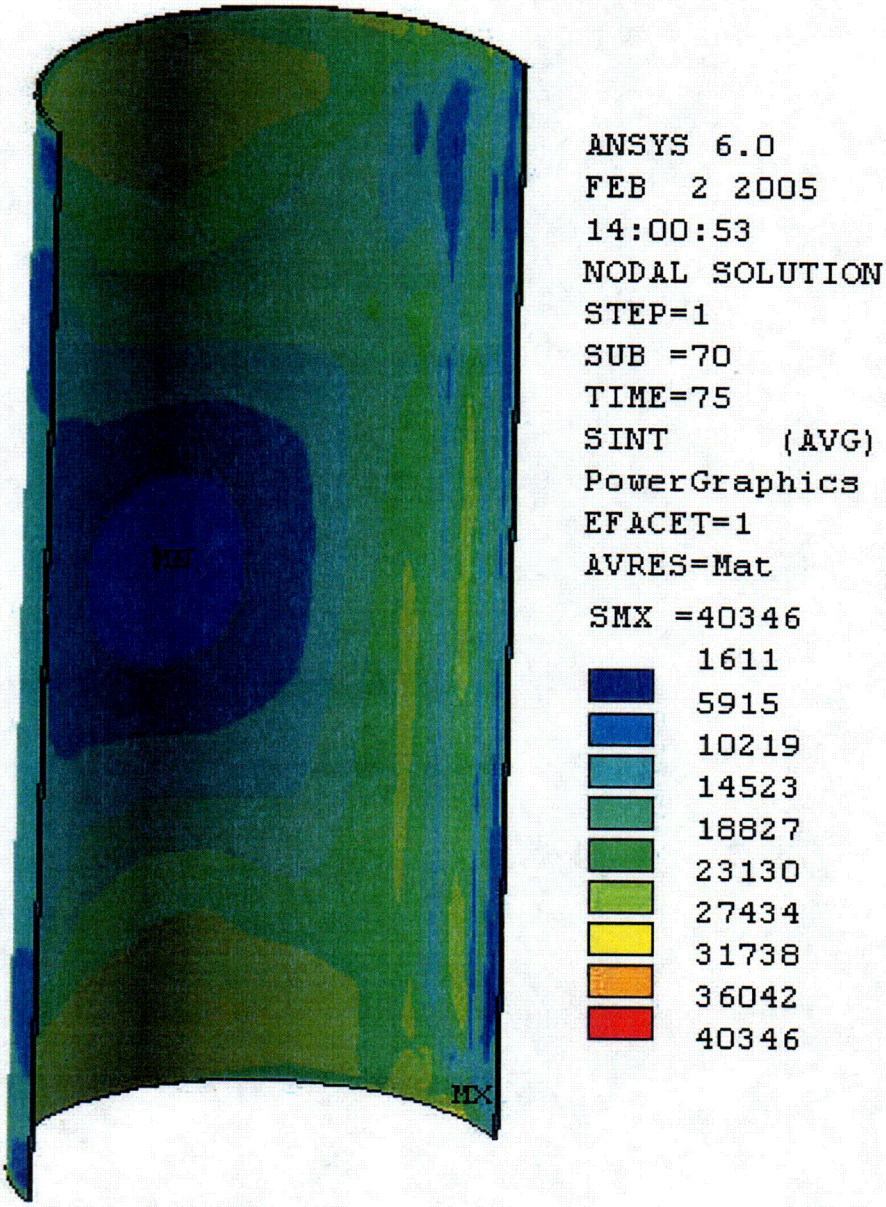

Figure 3-27
Inner Shell Stress Intensity Plot (Load Case 1)

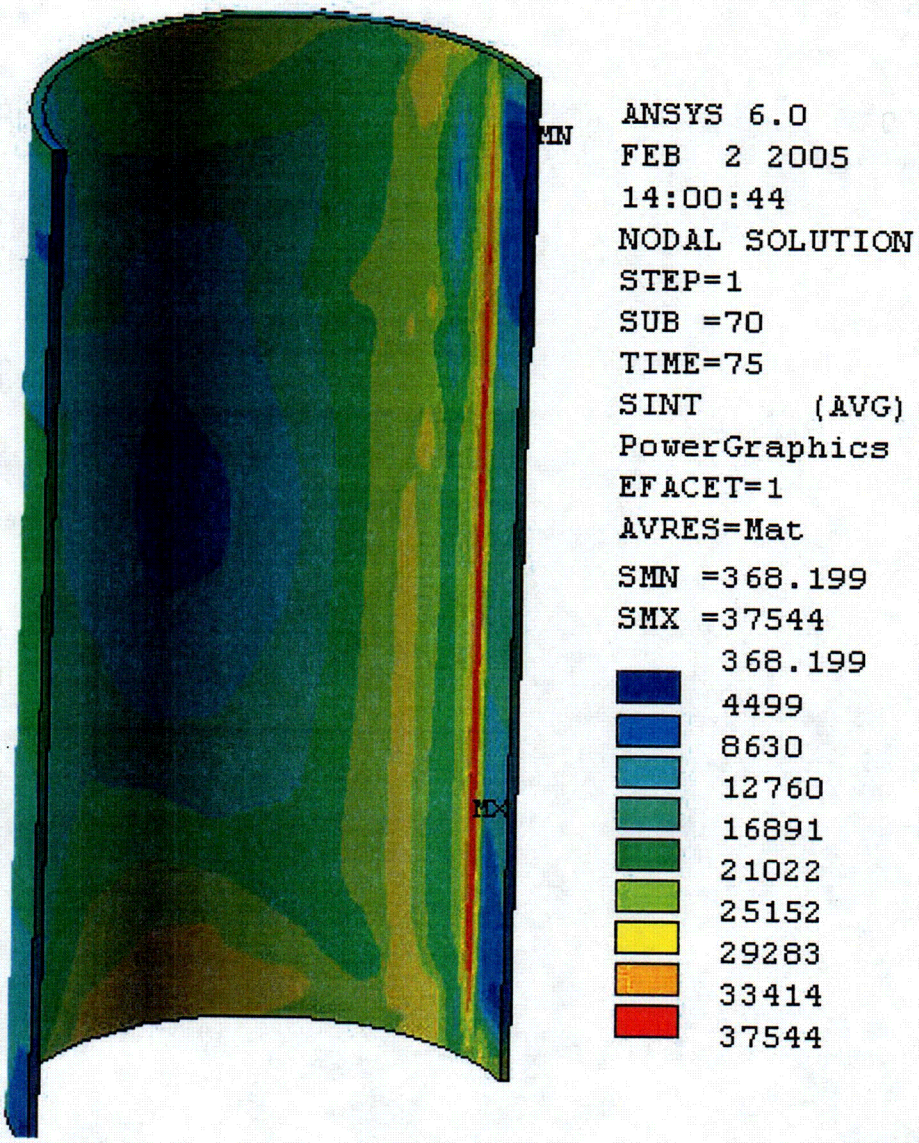

Figure 3-28
Outer Shell Stress Intensity Plot (Load Case 1)

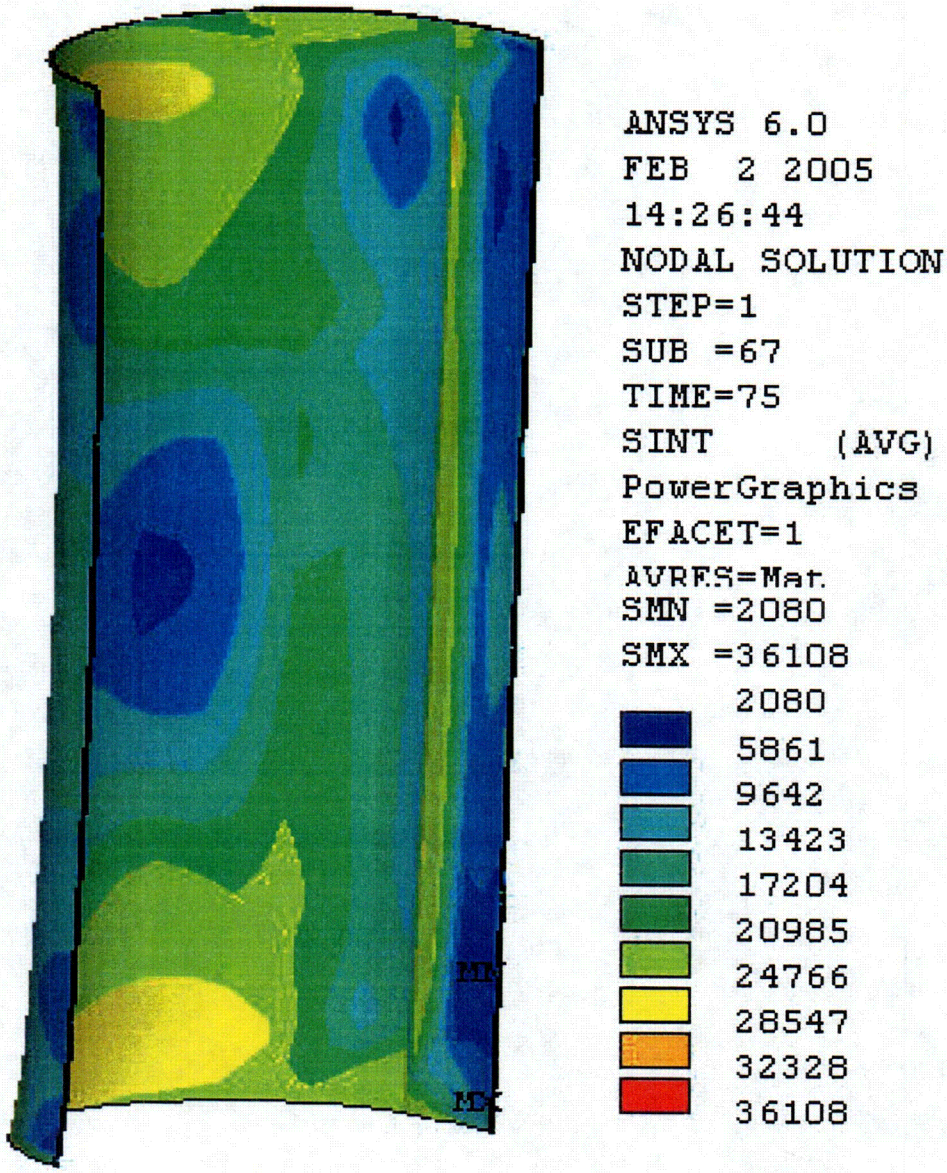

Figure 3-29
Inner Shell Stress Intensity Plot (Load Case 2)

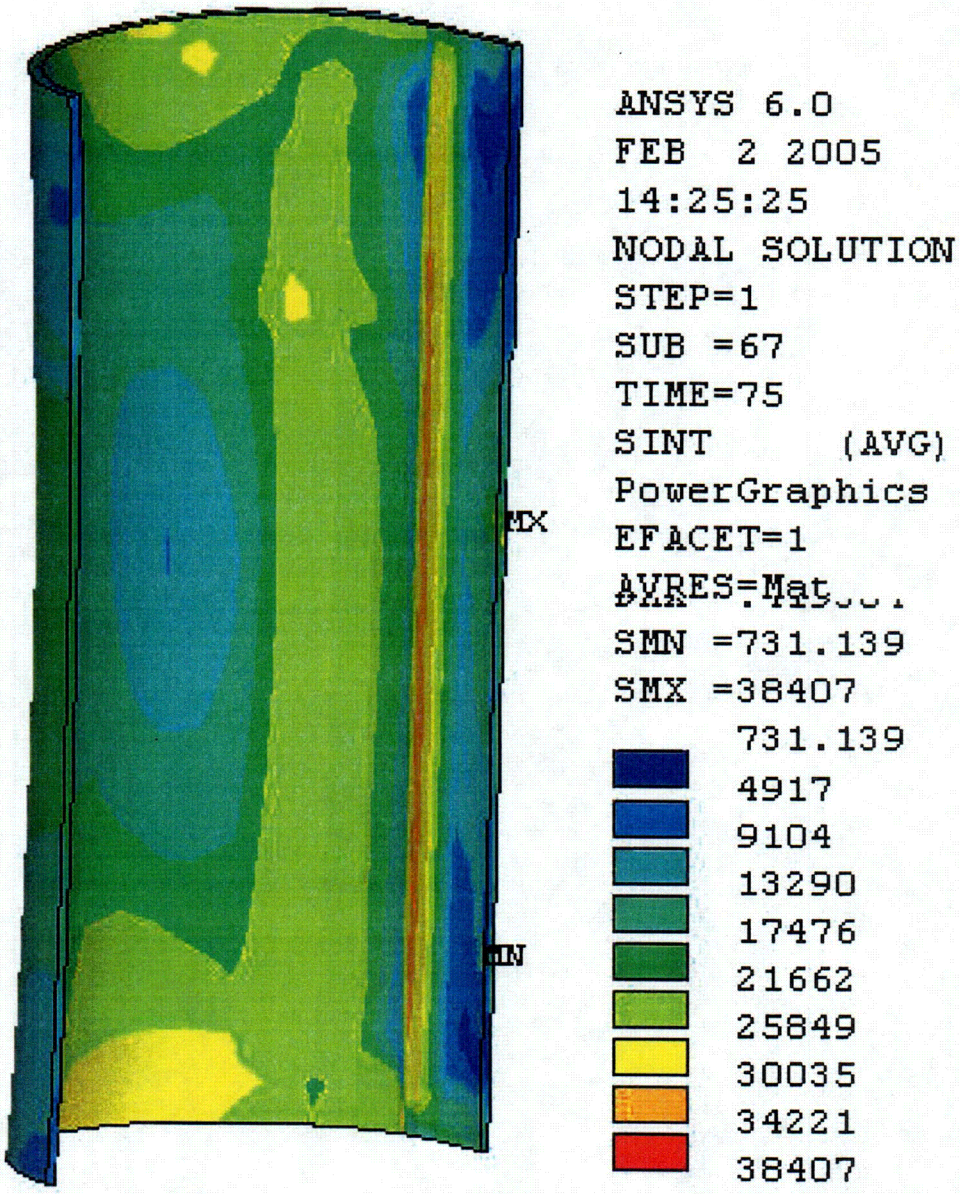

Figure 3-30
Outer Shell Stress Intensity Plot (Load Case 2)

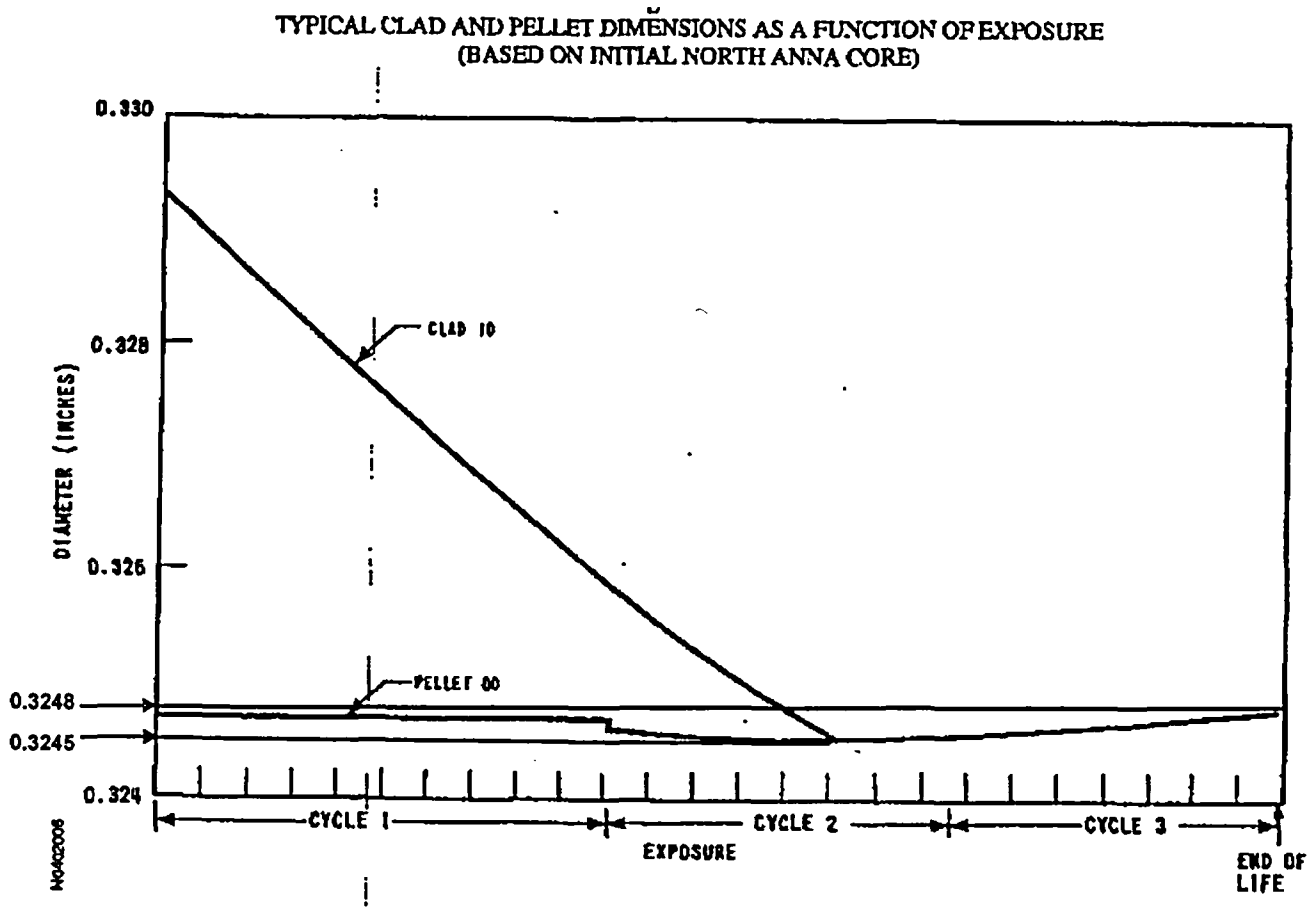

Figure 3-31
Typical Clad and Pellet Dimensions As A Function of Exposure

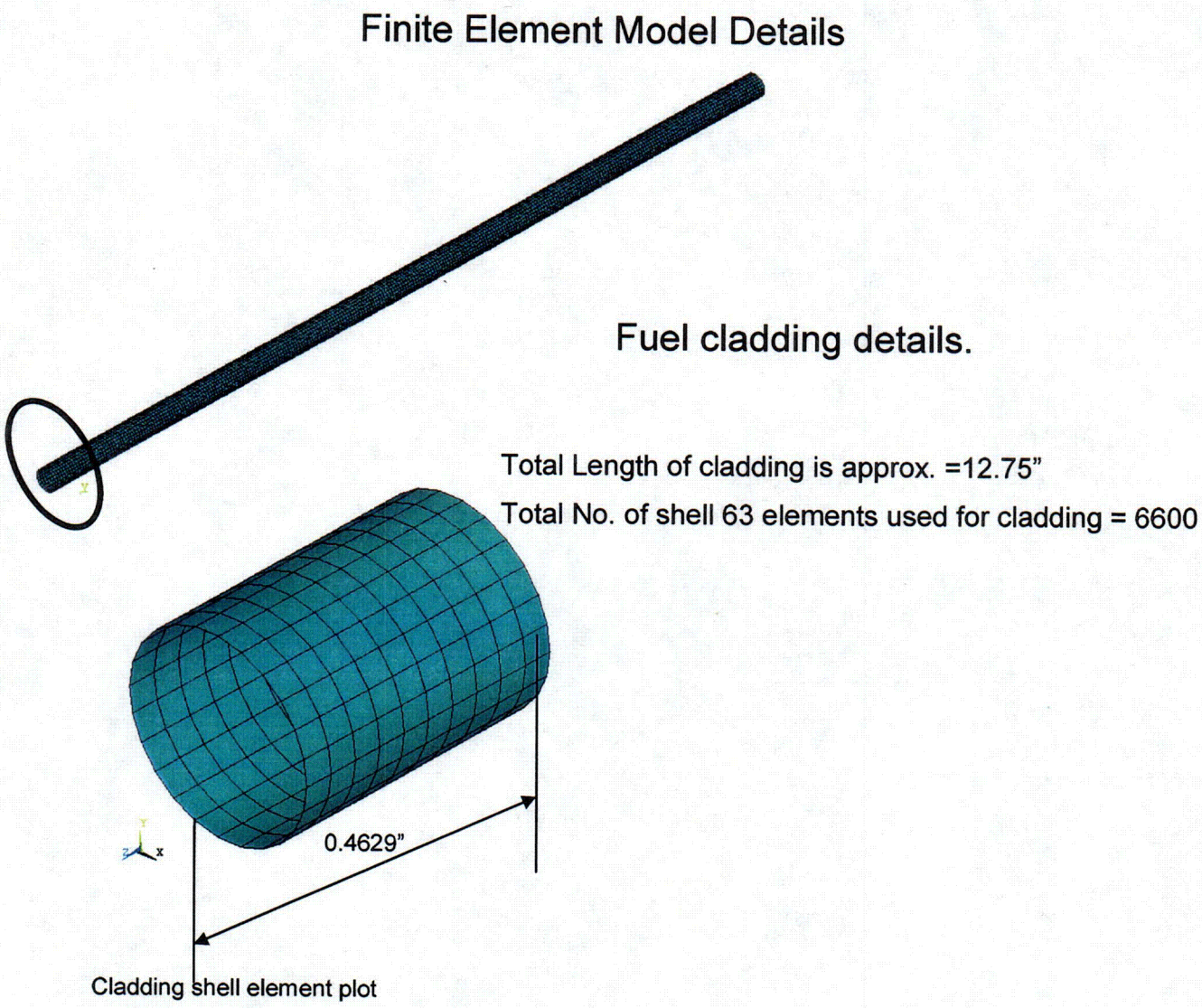

Figure 3-32
Finite Element Model of Cladding

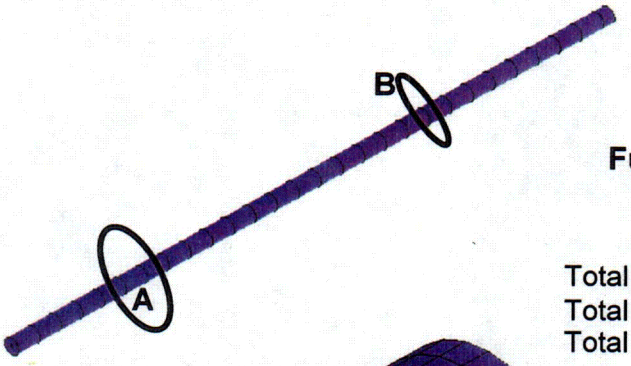

Fuel Pellet details.

Total no. of pellets =27.5
Total Length of pellets is approx. =12.75"
Total No. of solid 45 elements used for the Pellets= 33000

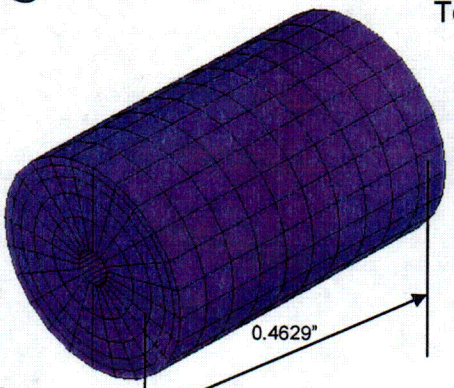

Pellet solid element plot for single pellet

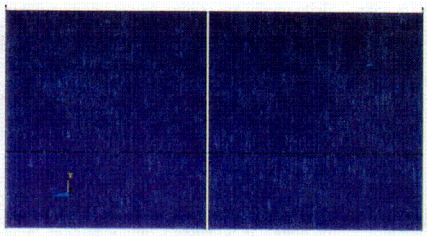

B

Total axial gap elements (Contact 52) used between the adjacent gaps in each pellet is 144.

Figure 3-33
Finite Element Model of Fuel Pellets

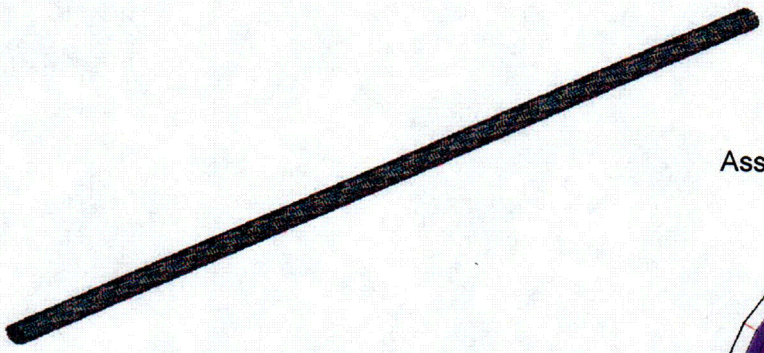

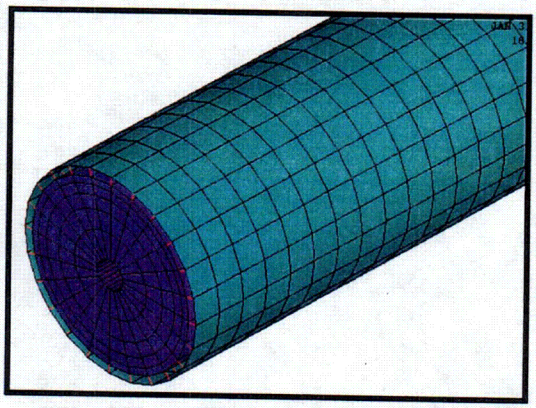

Assembly Details

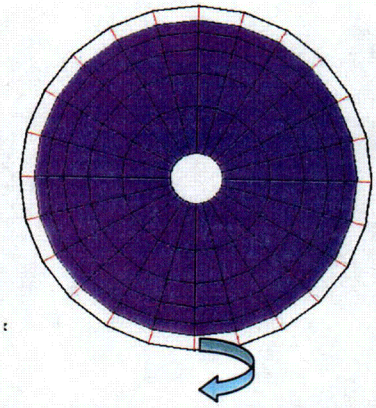

Total radial gap element (contact 52) used between the pellets and the cladding is 7272 for the entire length of approx 12.75" model.

Figure 3-34
Finite Element Model of Cladding and Pellets

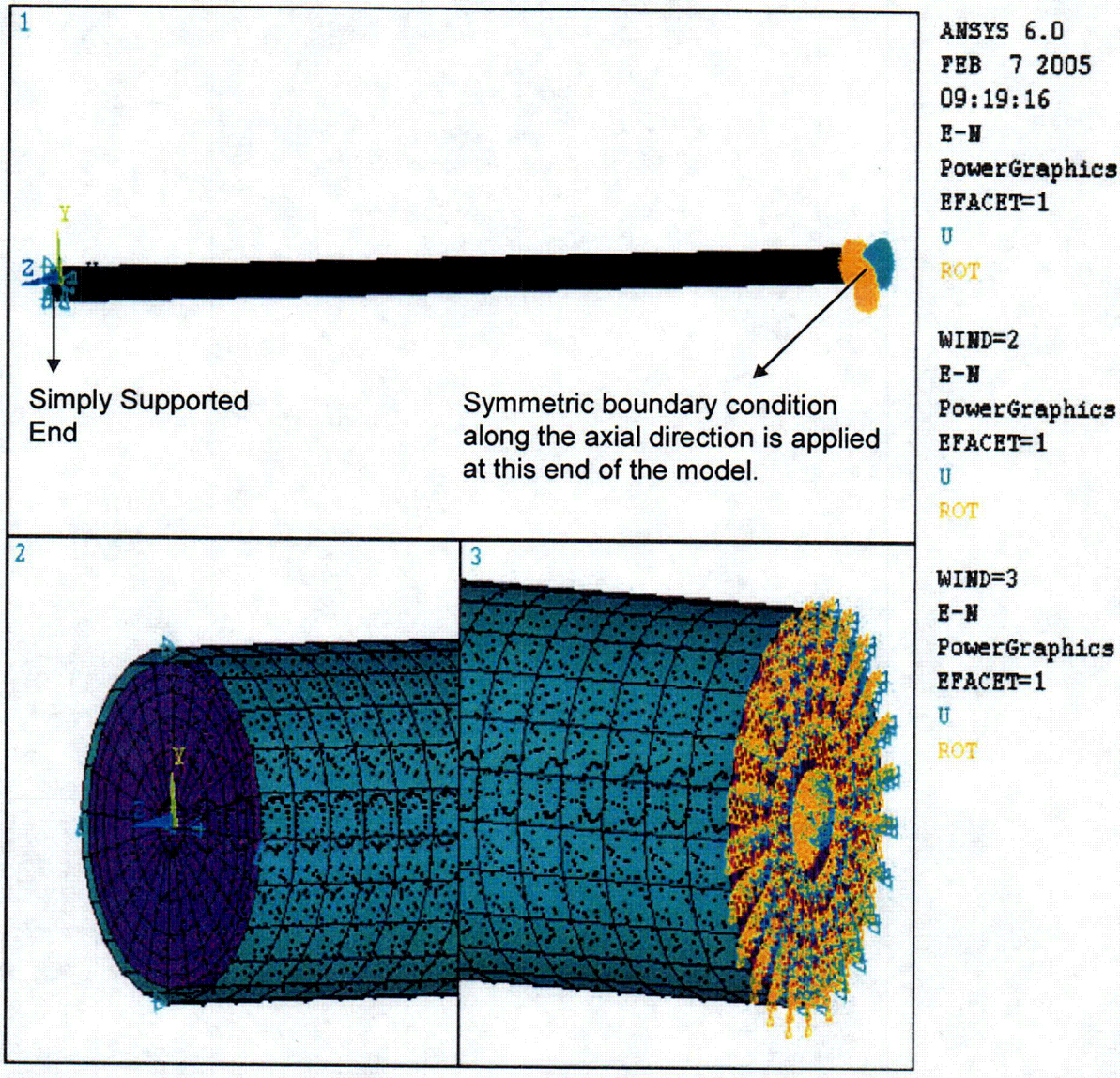

Figure 3-35
Boundary Conditions of Cladding/ Fuel Pellets Finite Element Model

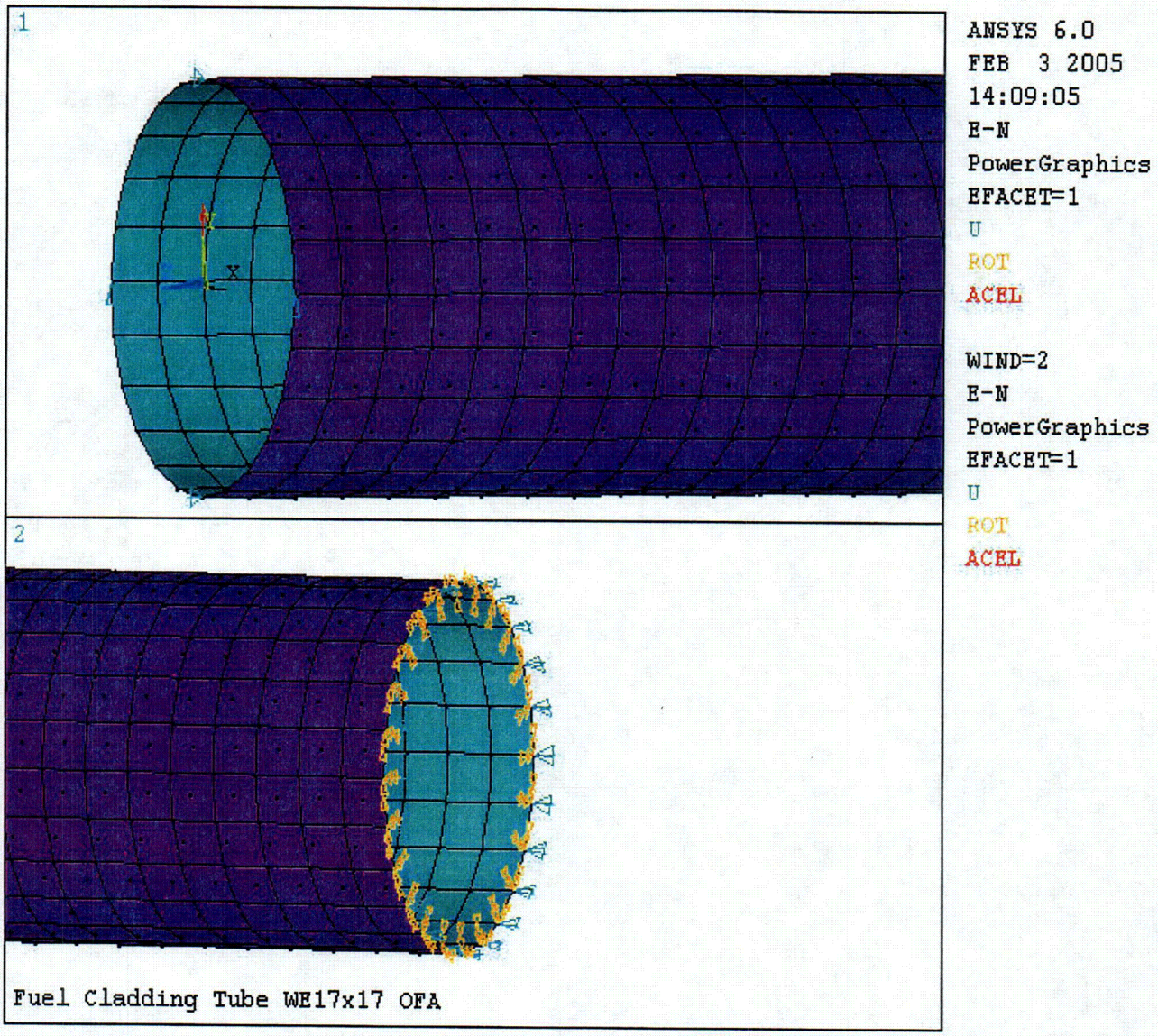

Figure 3-36
Boundary Conditions of Cladding Finite Element Model

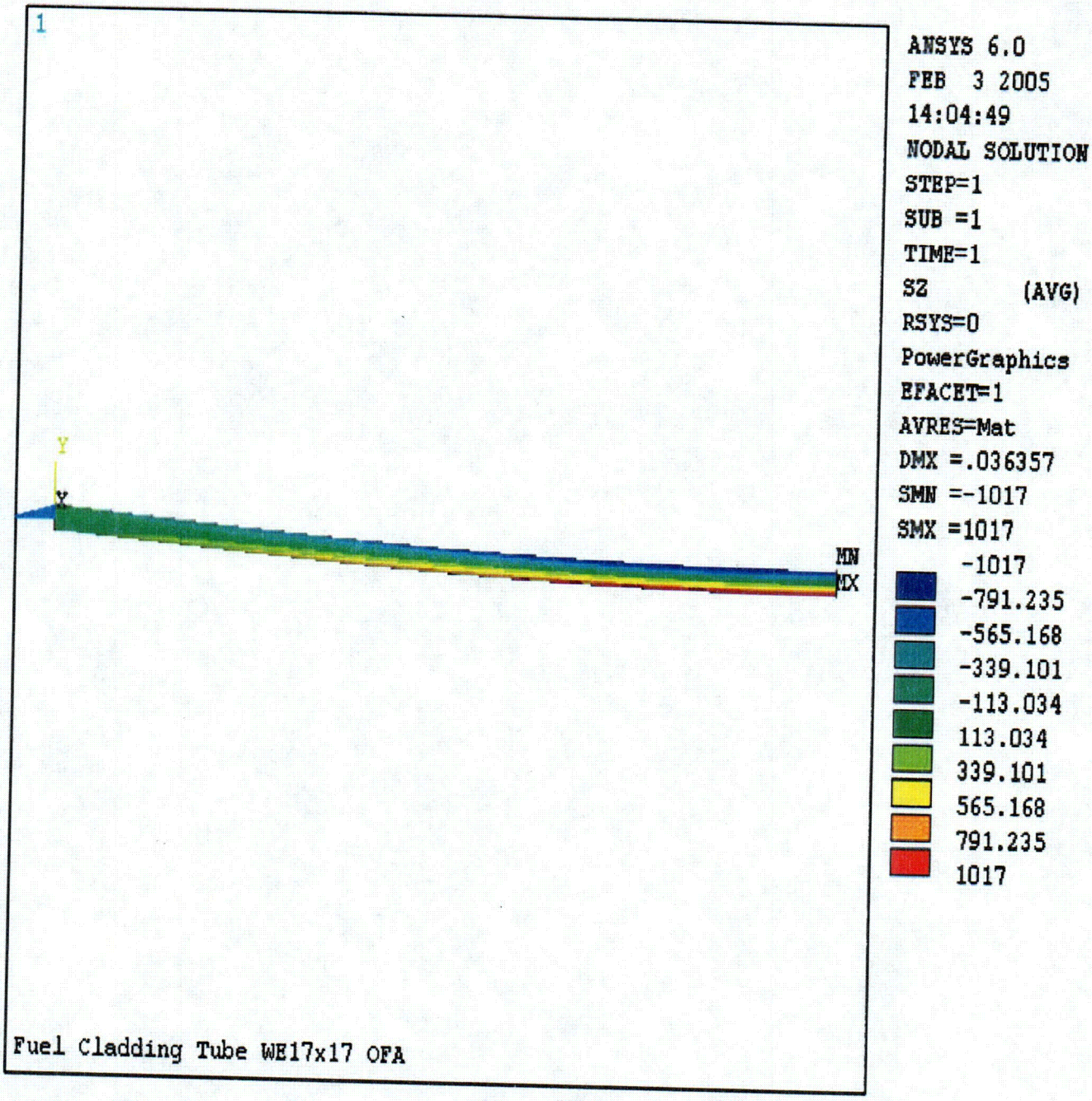

Figure 3-37
Cladding Stress Distribution
(Pellets are not Included in the Model)

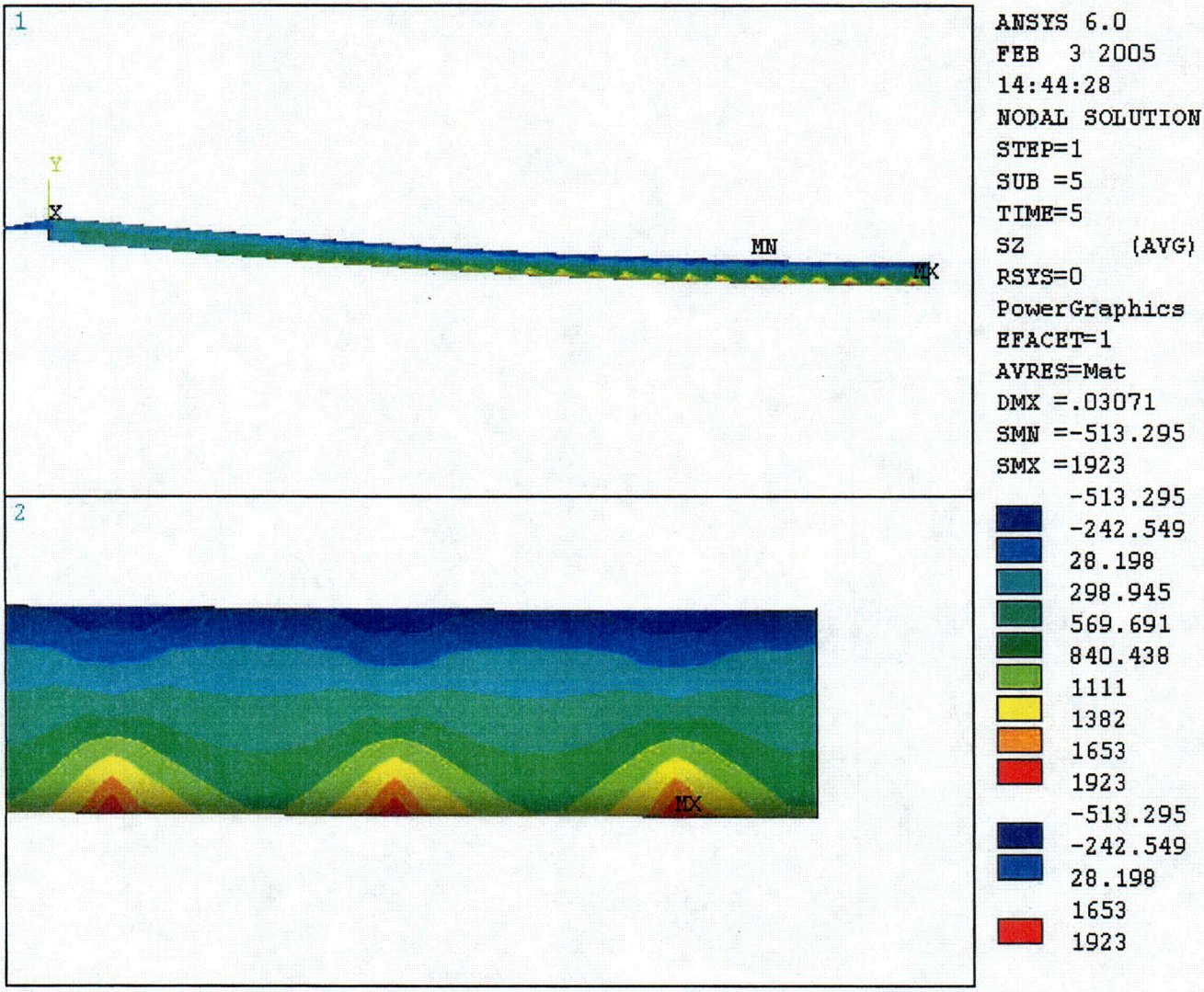

Figure 3-38
Cladding Stress Distribution-Including Pellets in the Model
(With Actual "E" of cladding and Actual "E" of Pellets)

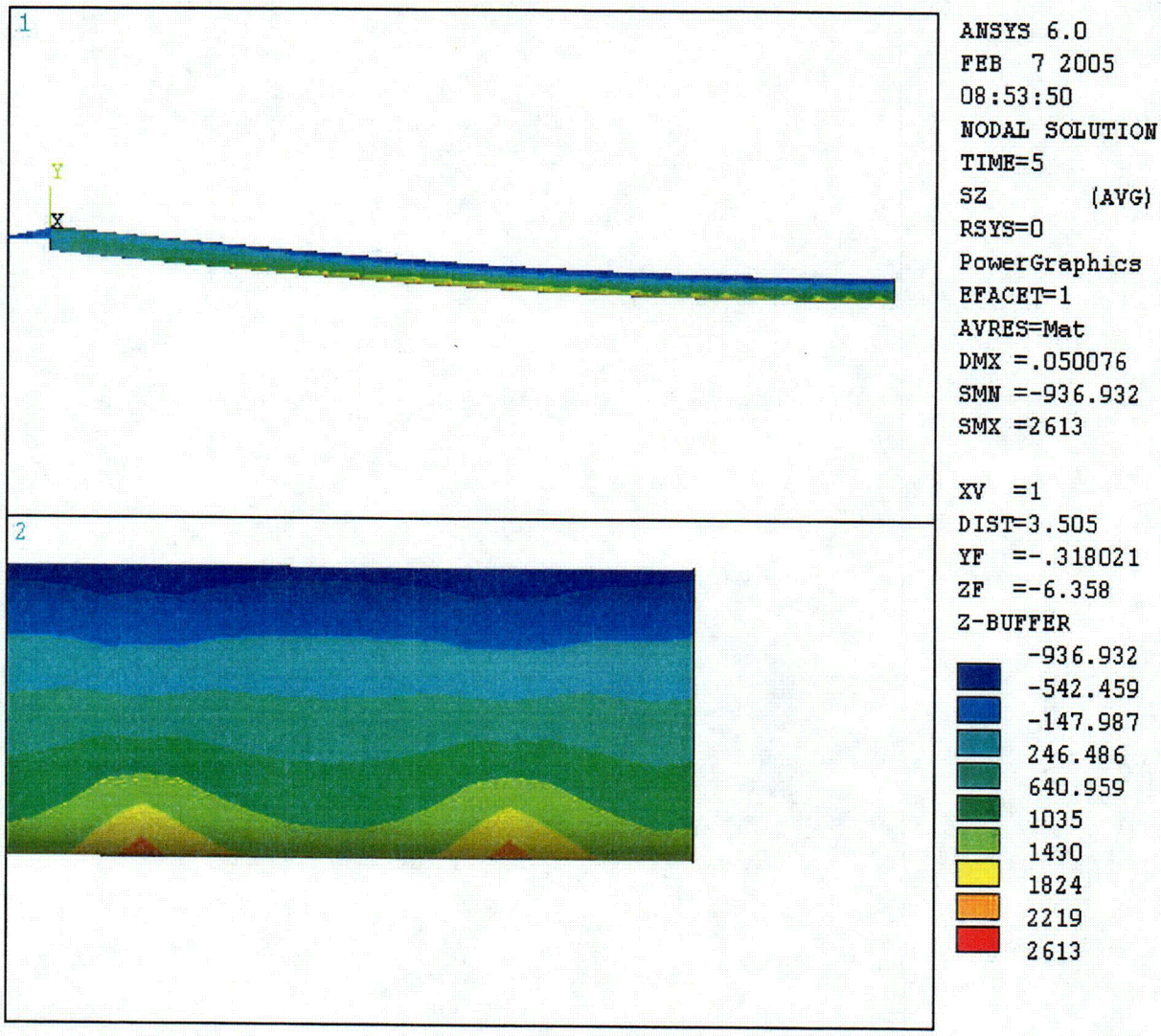

Figure 3-39
Cladding Stress Distribution-Including Pellets in the Model
(With Same "E" of cladding For Cladding & Pellets Material)

Fig. 26 Effect of tempering temperature on notch toughness

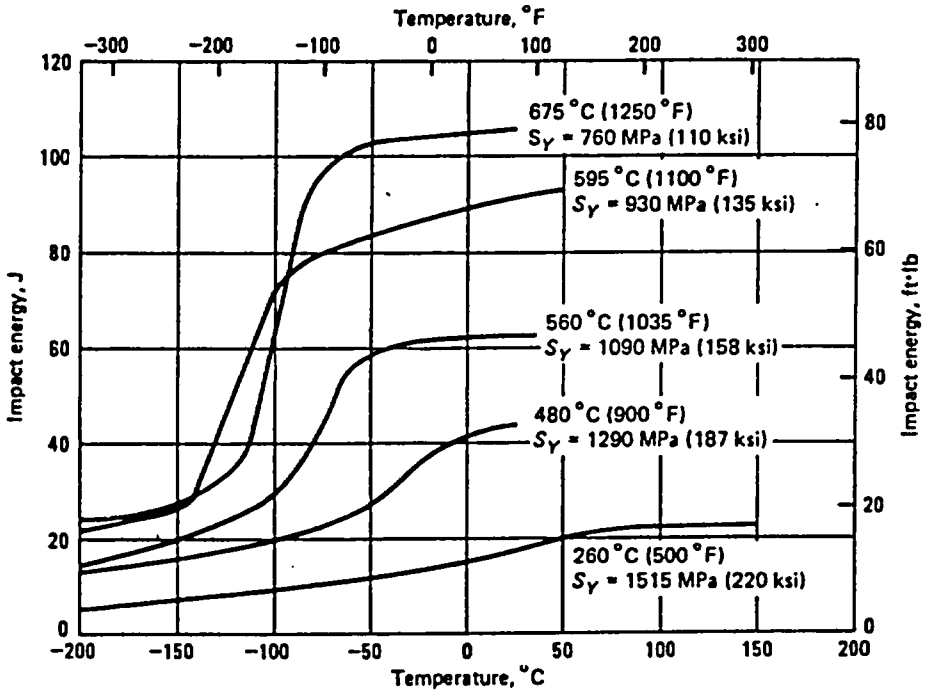

Variation of Charpy V-notch impact energy with temperature for various tempering temperatures. Specimens of 4340 steel were tempered 1.5 hr at the indicated temperatures. Yield strength obtained through each heat treatment also indicated. (Ref 15)

Figure 3-40
Effect of Tempering Temperature on Notch Toughness

Fig. 31 Correlation between notch toughness and yield strength

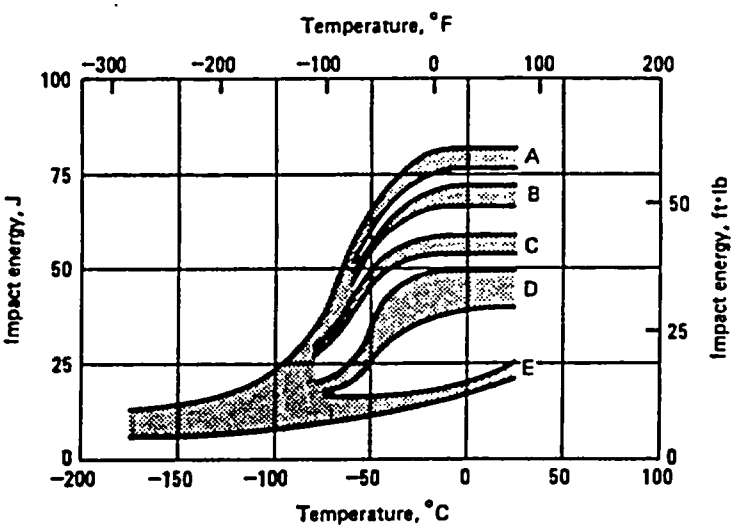

Yield strength	A	B	C	D	E
MPa	650	740	890	1025	1220
ksi	94	107	129	149	177

Variation in Charpy V-notch impact energy with temperature for a medium-carbon low-alloy steel tempered to various strength levels.

Figure 3-41
Correlation Between Notch Toughness and Yield Strength

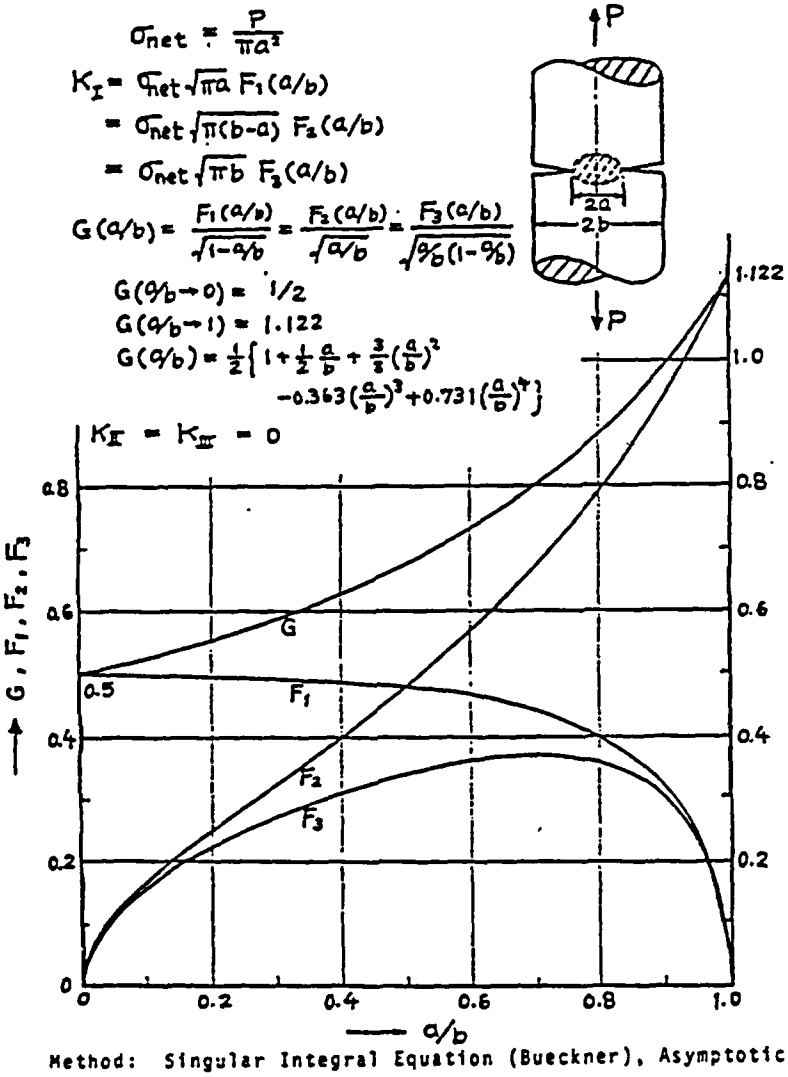

Method: Singular Integral Equation (Bueckner), Asymptotic Approximation (Benthem)

Accuracy: Better than 1%

Referencees: Bueckner 1965, 1972, Benthem 1972

Other References: Lubahn 1959, Wundt 1959, Irwin 1961, Paris 1965, Zahn 1965, Harris 1967

Figure 3-42

Singular Integral Equation and Asymptotic Approximation for Brittle Fracture Evaluation

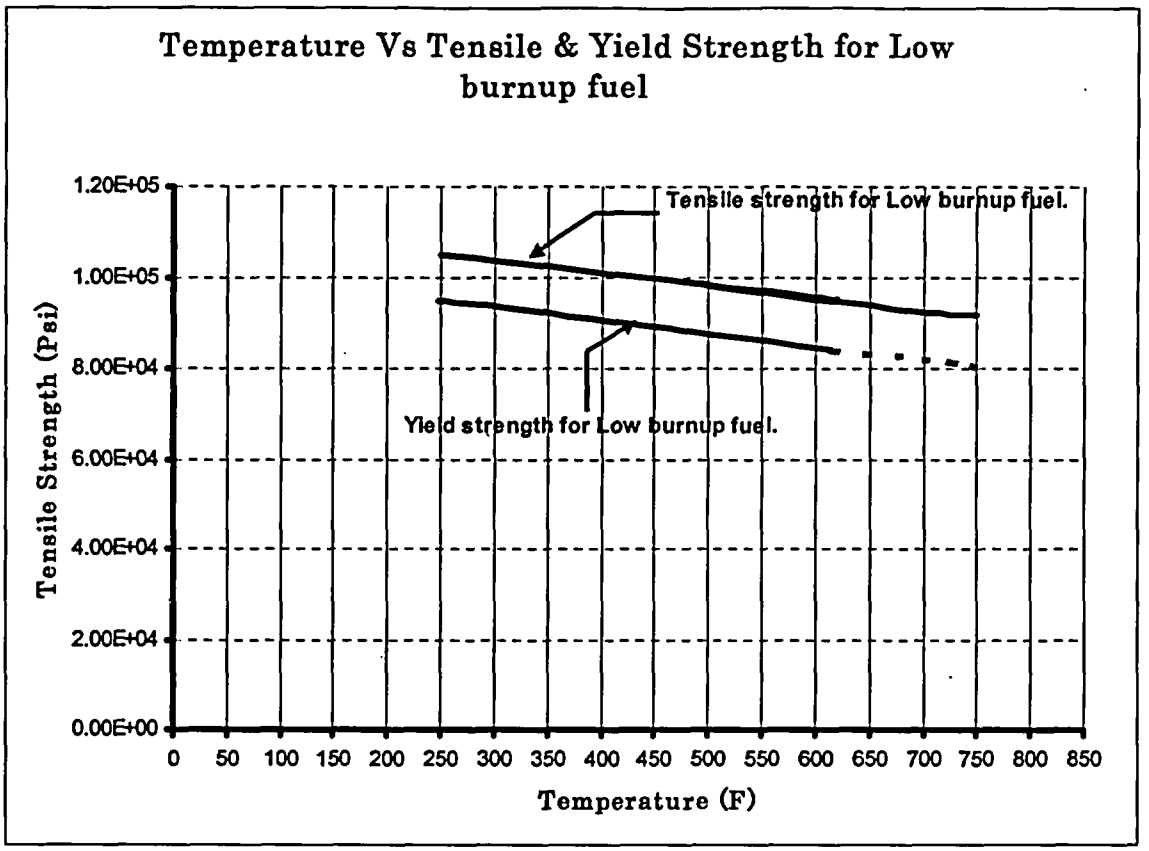

Yield Strength (Low Burn Up)	Temp F
9.49E+04	248
9.44E+04	264
9.39E+04	284
9.33E+04	304
9.24E+04	334
9.14E+04	369
9.01E+04	415
8.81E+04	486
8.44E+04	615
8.15E+04	725
8.05E+04	750

Tensile Strength (Low Burn Up)	Temp F
1.05E+05	250
9.52E+04	615
9.85E+04	486
9.20E+04	725
9.18E+04	750

Figure 3-43
Temperature Vs Tensile and Yield Strength for Low Burnup Fuel

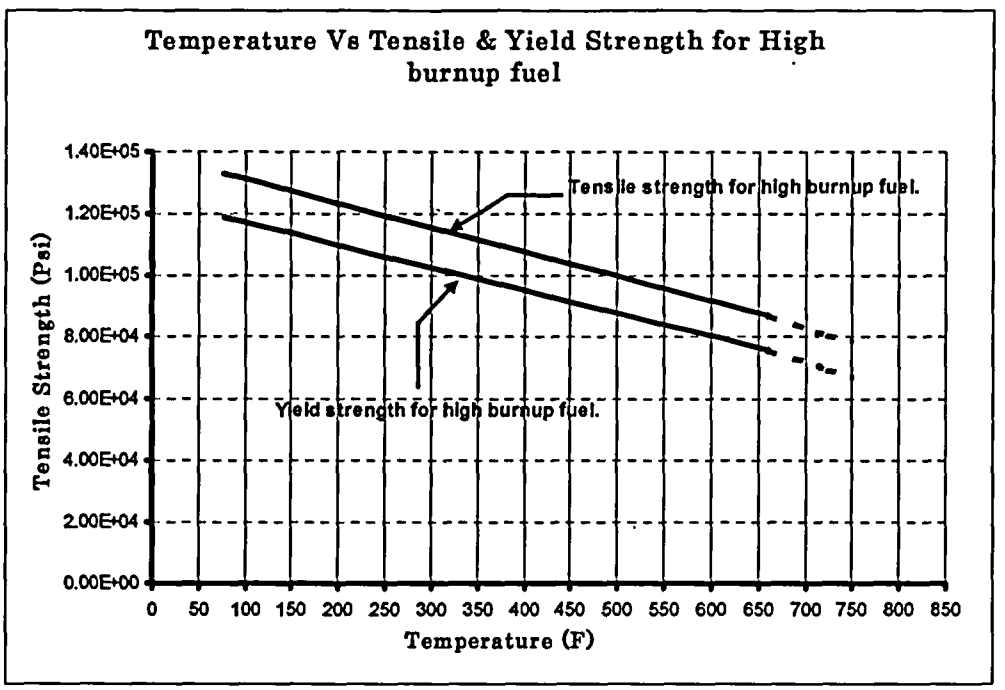

Tensile Strength (Psi) (High Burn Up)	Temp F
1.33E+05	77
8.73E+04	662
8.10E+04	725
7.90E+04	750

Yield Strength (Psi) (High Burn Up)	Temp F
1.19E+05	77
7.58E+04	662
6.95E+04	725
6.75E+04	750

Figure 3-44
Temperature Vs Tensile and Yield Strength for High Burnup Fuel

BEHAVIOR OF ZIRCALOY-4 AND ZIRCONIUM LINER ZIRCALOY-4 CLADDING AT HIGH BURNUP

L. F. Van Swam
Siemens Power Corporation
P. O. Box 130
Richland, Washington 99352-0130
(509) 375-8100

A. A. Strasser
Aquarius Services Corporation
17 Pokahoe Drive
North Tarrytown, NY 10591
(914) 366-8875

J. D. Cook
Rochester Gas and Electric Corporation
49 East Avenue
Rochester, NY 14609
(315) 524-4446

J. M. Burger
Empire State Electric Energy Research Corporation
1515 Broadway
New York, NY 10036-5701
(212) 302-1212

ABSTRACT

Fuel rods with different combinations of solid and annular pellets and through-wall and zirconium liner Zircaloy-4 cladding have been irradiated in the R. E. Ginna pressurized water reactor for four and five cycles, reaching burnups of approximately 57 MWd/kgU. Extensive poolside and hot cell examinations were performed to determine cladding oxidation, fuel rod diameter changes, cladding hydrogen pick-up and hydride distribution, and cladding strength and ductility at fast fluences (E > 1 MeV) of 7×10^{25} and 8.9×10^{25} n/m^2. Different behavior of the through-wall cladding compared to the liner cladding was observed and is discussed in the paper.

I. INTRODUCTION

The Empire State Electric Energy Research Corporation (ESEERCo), Rochester Gas and Electric Corporation (RG&E), and Siemens have carried out a program to fabricate, irradiate, and examine advanced PWR fuel rod designs containing annular fuel pellets, through-wall Zircaloy-4 cladding, and Zircaloy-4-zirconium liner cladding. Included for comparison were fuel rods with solid pellets and through-wall Zircaloy-4 cladding. The objectives of the program were to develop a fuel design with increased margin to failure and increased high burnup potential and to obtain performance data up to high burnup for use in fuel modeling.

Four demonstration test assemblies (DTAs) were designed and fabricated by Siemens. Irradiation and poolside examinations at RG&E's R.E. Ginna plant in New York State were completed after exposure of segmented fuel rods to 47 MWd/kgU after four cycles and to 57 MWd/kgU after five cycles. Hot cell examinations of four-cycle and five-cycle segmented fuel rods were carried out at the laboratories of Commissariat à l'Energie Atomique (CEA) in Grenoble, France.

This paper discusses the high-burnup behavior of standard through-wall Zircaloy-4 cladding and Zircaloy-4-zirconium liner cladding.

II. PROGRAM DESCRIPTION

A. Assembly and Fuel Rod Design

Each of the four 14x14 rod array assemblies fabricated for the program contained 179 fuel rods, 16 Zircaloy-4 guide tubes, and one instrument tube. The egg crate type spacers were of Zircaloy-4 with Inconel spacer springs. The assemblies had removable upper tie plates with Inconel leaf springs of standard design. The assemblies contained fuel rods 0.417 inch (10.59 mm) in diameter and 149 inches (3785 mm) long, with annular pellets and sponge zirconium liner-Zircaloy-4 cladding. Two of the DTAs contained 11 segmented rods each. The segmented rod consisted of four segments, the center two of which were characterized and examined in detail after irradiation. Figure 1 shows the axial locations of the characterized center two segments within the assembly. These segments are referred to in this paper as upper and lower segments, respectively. The characterized segments are approximately 25 inches (650 mm) long, with a 21.3 inch (540 mm) long fuel column and a 2.8 inch (71 mm) long plenum. Three combinations of pellet design (annular and solid) and cladding type (Zircaloy-4 with sponge zirconium liner and through-wall Zircaloy-4) were used in the fabrication of the segmented rodlets. The size of the diametral pellet-to-cladding gap, varying from 160

to 220 microns, was another test variable. Other dimensional data of the segmented rods are provided in Table 1. The chemical composition of the cladding is given in Table 2.

Table 1 Description of Segmented Fuel Rods

Feature	Dimension inches	mm
Segment Length	25.71	653.0
Cladding OD	0.417	10.59
Cladding Wall Thickness	0.0295	0.75
Active Fuel Length	21.33	541.8
Fuel Pellet Height	0.419	10.64
Nominal Fuel Pellet OD	0.3505	8.90
Fuel Pellet ID (Annular Pellet)	0.1108	2.81

Table 2 Fuel Cladding Chemical Analysis (Percent and ppm)

	Composition							
	Percent				ppm			
	Zr	Sn	Fe	Cr	O	Si	C	N
Through-wall Cladding, Zry-4	bal	1.50	0.21	0.11	1210	37	142	24
Liner Cladding, Zircaloy-4	bal	1.49	0.21	0.11	1265	82	130	41
Liner Cladding, Zr Liner*	bal	<10	440	<50	515	<25	40	14

* Sn, Fe, and Cr values are in ppm

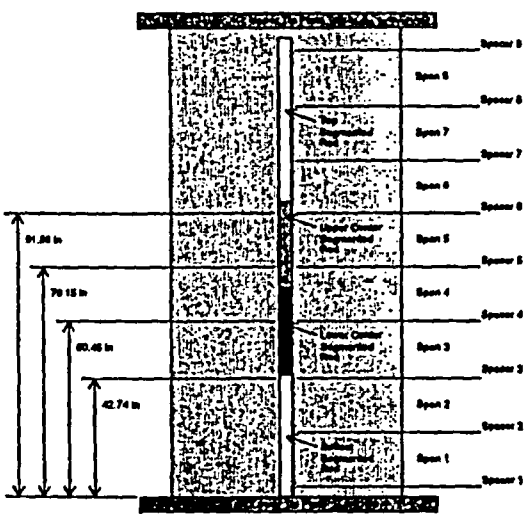

Figure 1 Axial Locations of Upper and Lower Segmented Rods within an Assembly

B. Irradiation and Power Histories

The demonstration test assemblies were irradiated for four yearly cycles to an assembly average burnup of 42.7 MWd/kgU. One of the DTAs containing segmented rods was irradiated for a fifth cycle to an average burnup of 52.1 MWd/kgU. The segmented rodlets with annular pellets reached average burnups of 47 and 57 MWd/kgU after four and five cycles of irradiation, respectively. The burnup of the solid pellet rodlets was somewhat lower due to their lower initial enrichment. The average linear heat generation rates (LHGRs) of the rodlets during the five consecutive cycles are provided in Table 3. There were no failures in any of the rods throughout the irradiation program. After five consecutive cycles of irradiation, the high-burnup assembly was still in excellent condition with no signs of bow, unusual rod-to-rod gap closure, or fuel rod fretting wear.

Table 3 Fuel Rodlet Power History, Cycle Length, and Burnup

	LHGR kW/ft (W/cm)		Cycle Length,	Effective Full-Power	Assembly Burnup,
Cycle	BOC	EOC	Days	Days	MWd/kgU
1	6.4 (210)	5.7 (185)	307	285	8.9
2	9.9 (325)	8.5 (280)	322	311	23.9
3	7.9 (255)	7.4 (240)	331	319	37.0
4	3.1 (100)	3.3 (105)	355	343	42.5
5	6.5 (210)	6.8 (225)	309	271	52.1

III. PROGRAM SCOPE OF WORK

A. Poolside Examinations

The fuel assemblies were inspected after each of the first three irradiation cycles. Comprehensive poolside examinations were carried out after the fourth and fifth irradiation cycles. Fuel rods were withdrawn from the assemblies in order to determine the fuel rod length, plenum length, diameter profile, and oxide thickness along the length of the rod. Fission gas release was measured nondestructively in full-length rods and in segmented rods during the final poolside examination. Segmented rods were separated at poolside for shipment to the hot cell laboratory.

B. Hot Cell Examinations

Seventeen segmented rodlets were shipped to the CEA hot cells in Grenoble, France. Three pairs of rods with four and five cycles of irradiation were examined in detail. Less extensive examinations were performed on some of the other rods. The rods that underwent detailed examinations were numbered 1 through 6. Table 4 lists the main characteristics of these rods.

Table 4 Main Characteristics of Segmented Rods Examined at Hot Cells

Rod	Pellet Design	Cladding Type	Number of Cycles Irradiated	Rod Burnup, MWd/kgU	Axial Location*
1	Solid	Zry-4	4	43	Lower
2	Solid	Zry-4	5	52	Lower
3	Annular	Zry-4	4	47	Upper
4	Annular	Zry-4	5	57	Upper
5	Annular	Liner	4	47	Upper
6	Annular	Liner	5	57	Upper

* See Figure 1 for axial locations of upper and lower segments.

IV. RESULTS AND DISCUSSION

The results of poolside and hot cell oxide thickness and profilometry measurements are presented and discussed. Hydrogen pick-up was measured at the hot cells; hydride distribution was determined by metallographic examination. Cladding tensile tests were performed at room temperature and at 350°C.

A. Oxide Thickness

Fuel cladding oxide thickness was measured at poolside with an eddy current probe by performing a single linear scan along the length of a rod after the rod had been withdrawn from the assembly. At end-of-life, at an assembly average burnup of 52 MWd/kgU, the maximum oxide thickness of full-length rods (all with liner cladding) averaged approximately 40 microns. The maximum oxide thickness always occurred in Span 7 of the assembly. A comparison of the oxide thickness of segmented rods with through-wall Zircaloy-4 cladding and liner Zircaloy-4 cladding indicated that the liner cladding had a lower corrosion rate than the through-wall cladding. This was confirmed by hot cell measurements.

In the hot cells, four linear scans 90 degrees apart were made along each of the six rods listed in Table 4. The circumferential average oxide thickness, determined from the four linear traces, is shown in Figure 2. Indicated on the plots are the positions of spacers, the location of the rods in relation to the assembly lower tie plate, and the nominal (core average) coolant temperature along the rods. The traces of Rods 1 and 3 and of Rods 2 and 4 have been combined in single plots because these pairs of rods have identical cladding and exposure times. The average oxide thickness in the fuel rod plenum areas, the areas where a rod passes through spacers, and the maximum oxide thickness in each span (region between spacers) are listed in Table 5.

Table 5 Average Oxide Thickness at Selected Locations

	Oxide Thickness, μm			
	Through-Wall Zry-4		Zr Liner-Zircaloy-4	
Location*	End of Cycle 4	End of Cycle 5	End of Cycle 4	End of Cycle 5
Plenum 4	6	12	—	—
Plenum 6	11	16	8	12
Spacer 4	10	15	—	—
Spacer 5	12	17	12	16
Spacer 6	14	19	13	17
Span 3	18	42	—	—
Span 5	38	40	17	23

* See Figures 1 and 2 for plenum, spacer, and span locations.

As indicated in Table 5, the measurements show that with increasing height in the assembly, and hence increasing coolant and cladding temperature, the oxide thickness in spacer areas increases by approximately 2 microns per span for the through-wall Zircaloy-4 cladding and approximately 1 micron per span for the liner cladding in both the four and five cycle rods. For the plenum areas of Zircaloy-4 cladding, the increase is 4 to 5 microns per rodlet length. There are no comparable plenum area data for rods with liner cladding.

Observed increases in oxide thickness with increasing cladding temperatures are in fair agreement with an activation temperature of 14,080 K for in-reactor Zircaloy-4 corrosion as given in MATPRO.[1] Depending on the initial oxide thickness in a given spacer area, increases of 1.7 to 2.5 microns between Spacers 4 and 5 and of 1.9 to 2.8 microns between Spacers 5 and 6 are calculated. The calculated increase of the oxide thickness in the plenum areas between lower and upper rods is 2.5 microns for four-cycle and 3.8 microns for five-cycle rods.

The corrosion rate of the through-wall cladding appears to be higher than the corrosion rate of the liner cladding. This is most clearly observed in the non-heat transfer plenum area, where there is no thermal feedback effect that could account for the differences in oxide thickness after four and after five cycles.

From End of Cycle (EOC) 4 to EOC 5 (i.e., during Cycle 5), the oxide thickness in the plenum areas and in the spacer areas increased approximately 4 to 6 microns. This is slightly higher than would be indicated by a post-transition corrosion rate that is linear with time. This indicates that there may have been an increase in the corrosion rate in the plenum areas (non-heat transfer surface) and the spacer regions during the last irradiation cycle.

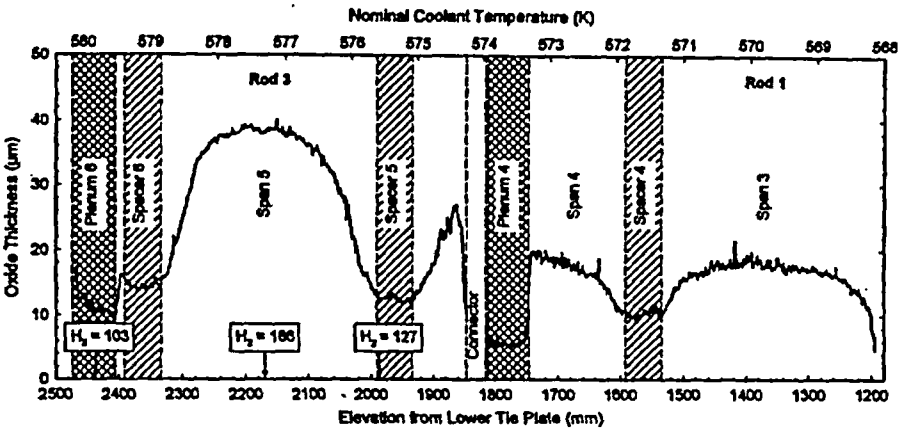

Rods No. 1 and 3, Through-Wall Zircaloy-4 Cladding, Four Cycles of Irradiation

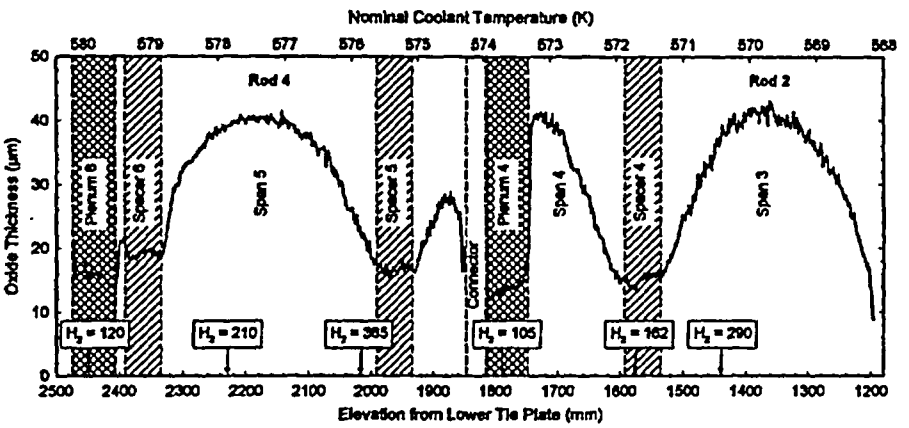

Rods No. 2 and 4, Through-Wall Zircaloy-4 Cladding, Five Cycles of Irradiation

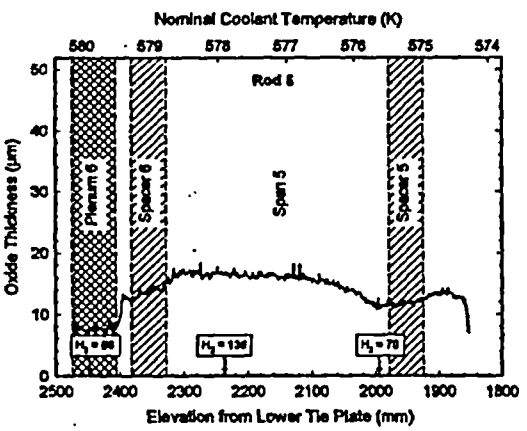

Rod No. 5, Liner Zircaloy-4 Cladding, Four Cycles of Irradiation

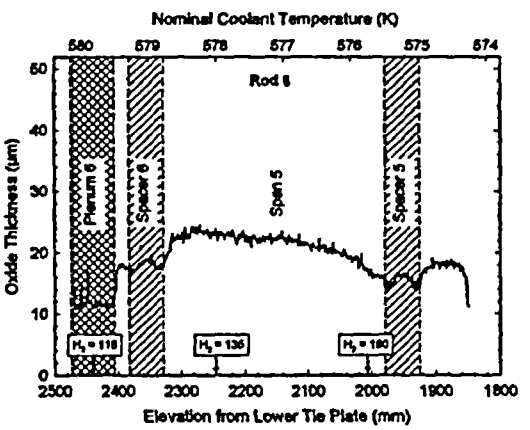

Rod No. 6, Liner Zircaloy-4 Cladding, Five Cycles of Irradiation

Figure 2 Oxide Thickness Profiles (Circumferential Average) of Four-Cycle and Five-Cycle Rods with Through-Wall and Liner Zircaloy-4 Cladding. Hydrogen concentrations at the positions indicated are ppm values.

The behavior of the cladding in the fueled sections outside the spacer areas depends on power history, which affects the cladding temperature, and cladding type. The through-wall Zircaloy-4 cladding had a larger oxide thickness accumulation at an equivalent in-reactor residence time than the Zircaloy-4 liner cladding. This is readily observed by comparing the oxide thickness of Rod 3 to Rod 5 (four cycles of irradiation, same axial location) and of Rod 4 to Rod 6 (five cycles each). This comparison is shown in Figures 3a and 3b. In both cases, the rods with the through-wall Zircaloy-4 cladding show significant corrosion whereas the liner cladding has much lower corrosion. A comparison of the oxide thickness of Rod 1 and Rod 2 (Figure 3c) indicates that for a lower segment with through-wall Zircaloy-4 cladding, a large part of the oxide growth occurred during the fifth cycle.

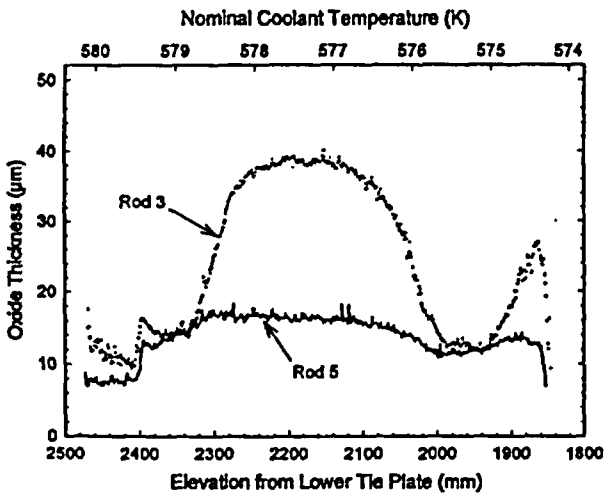

Figure 3a Oxide Thickness Profiles of Four-Cycle Rods 3 and 5 with Through-Wall (Rod 3) and Liner (Rod 5) Zircaloy-4 Cladding

Figure 3d compares the corrosion profiles of Rod 3 (four-cycle through-wall cladding) and Rod 6 (five-cycle liner cladding). In the plenum and spacer areas, the oxide thickness of the four-cycle through-wall cladding is, as expected, less than that of the five-cycle liner cladding. In the main span of the rod, however, the corrosion of the through-wall cladding is much higher than that of the liner cladding. This indicates that the corrosion rate of the through-wall cladding has accelerated whereas the corrosion rate of the liner cladding has remained constant or increased only slightly.

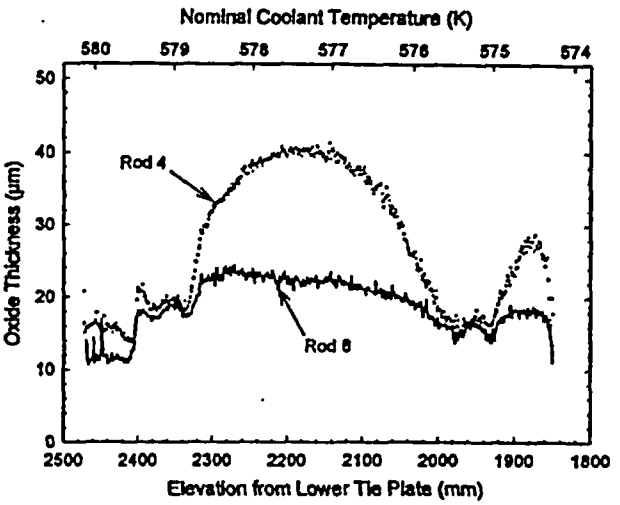

Figure 3b Oxide Thickness Profiles of Five-Cycle Rods 4 and 6 with Through-Wall (Rod 4) and Liner (Rod 6) Zircaloy-4 Cladding

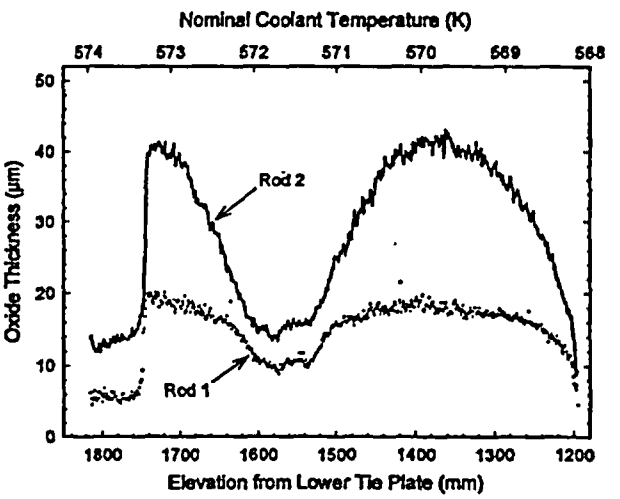

Figure 3c Oxide Thickness Profiles of Four-Cycle Rod 1 and Five-Cycle Rod 2 with Through-Wall Zircaloy-4 Cladding

In summary, it may be stated that the initial corrosion rate of the through-wall cladding appears to be higher than that of the liner cladding and that the through-wall cladding appears to be much more susceptible to accelerated corrosion at high burnup than the liner cladding. The acceleration seems to be influenced by temperature, occurring earlier and being more pronounced at higher temperature. The root cause of this difference in behavior has not been fully determined. Small differences in composition (silicon content), fabrication processes, or

differences in hydrogen pick-up and hydride distribution (see also below) could be possible causes.

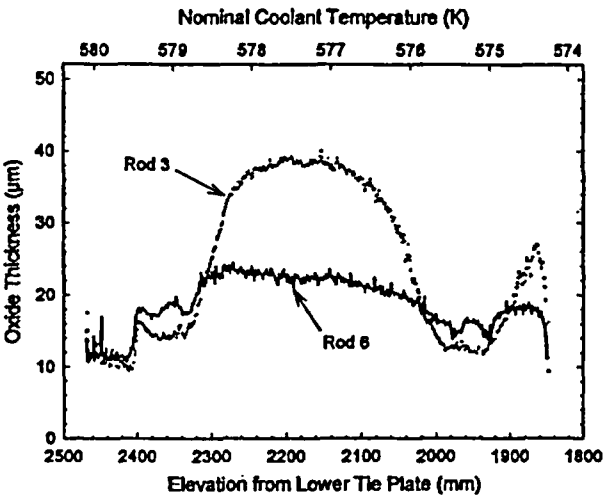

Figure 3d Oxide Thickness Profiles of Four-Cycle Rod 3 and Five-Cycle Rod 6 with Through-Wall (Rod 3) and Liner (Rod 6) Zircaloy-4 Cladding

B. Profilometry

Poolside measurements indicated that the fuel rods attained their maximum creepdown during the fourth cycle of irradiation. The amount of creepdown depended on the initial fuel-to-cladding gap size, rods with the largest gap showing the largest creepdown. Creepdown data, corrected for oxide accumulation, are shown in Figure 4. There was no noticeable difference in the creepdown behavior between rods with through-wall Zircaloy-4 cladding and rods with liner cladding. During the fifth cycle of irradiation, all rod diameters, regardless of initial gap size, increased by approximately 0.15%, indicating fuel-to-cladding contact during the last cycle and fuel pellet swelling of approximately 0.5 volume percent per 10 MWd/kgU burnup.

Six axial profilometry scans, each 30 degrees apart, were made in the hot cells on each of the six segmented rods listed in Table 4. Rod average diameter, rod ovality, and clad ridging were determined from the scans. All profilometry data were corrected for oxide accumulation. Figure 5 shows the rod average diameter before and after correction for oxide thickness. Uniform creepdown and a uniform diameter along the rod length are expected, since the fast fluence and pellet swelling along the length of the rod are close to uniform.

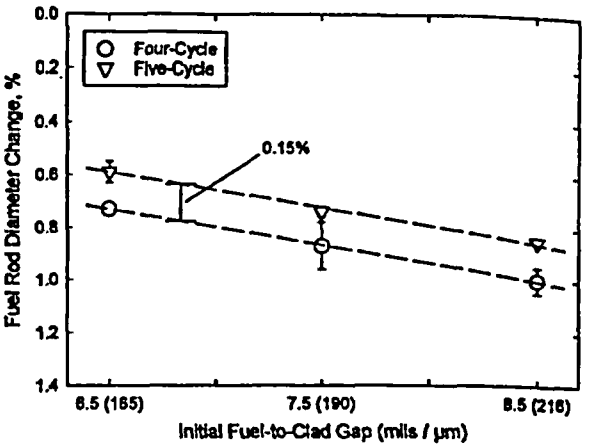

Figure 4 Fuel Rod Diameter Change from Beginning-of-Life Diameter as a Function of Initial Pellet-to-Cladding Gap Size

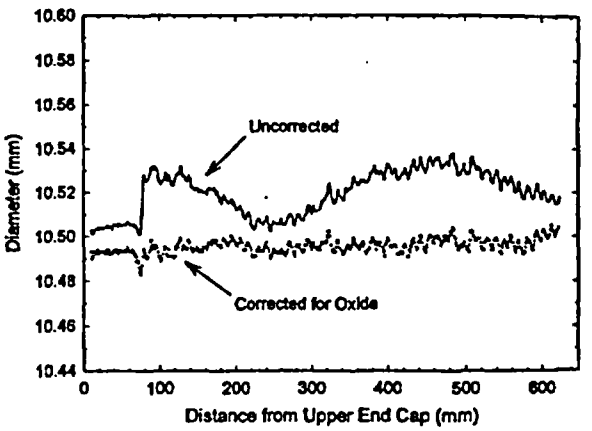

Figure 5 Diameter Profile of Rod 2 Before and After Correction for Oxide Accumulation

A Pilling-Bedworth factor of 1.75 was used to correct for oxide thickness accumulation; this resulted in uniform diameter profiles for all the rods measured. It indicates that the bulk oxide is approximately 89-90% dense. Metallographic observations also indicate that the oxide of the fuel rod cladding is not fully dense.

Figure 6 compares the oxide-thickness-corrected diameter traces of Rods 1 and 2. Whereas the cladding continues to creep down in the plenum area, the rod diameter has increased (outward creep) in the fueled section of the rod during the fifth (final) irradiation cycle. This was observed for other pairs of rods as well and

agrees with the findings from the poolside examination. The outward creep is due to fuel pellet swelling.

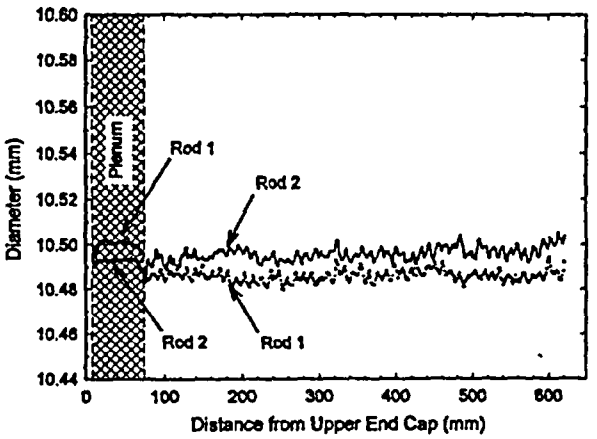

Figure 6 Diameter Profile of Four-Cycle Rod 1 Compared to Profile of Five-Cycle Rod 2. During Cycle 5, there was continued creepdown in the plenum area, whereas pellet swelling caused a diameter increase in the fueled section of the rod.

At 22 microns, cladding ovality (half the difference between smallest and largest diameter measured at any axial location) in the plenum area was typically much higher than in the fueled sections of the rods, where the cladding is supported by the fuel pellets, and where ovality averaged 5 microns.

Ridge height, at 2 to 3 microns, was small in all rods. There was no difference in ridge height between rods with solid pellets and rods with annular pellets. The presence of ridges is another indication of pellet-to-cladding contact.

C. Hydrogen Pick-up

The hydrogen concentration of the cladding was determined by vacuum extraction in the plenum region, the fuel region (at highest oxide thickness), and in the spacer region of the fuel rods. The data are shown in Figure 3 and are tabulated in Table 6. The hydrogen concentration reported includes the initial hydrogen level of the cladding, which was 10 to 15 ppm. Hydrogen pick-up ratios were calculated, taking into account the initial hydrogen level of the cladding. In the calculations, a Pilling-Bedworth ratio of 1.75 is assumed. The hydrogen pick-up fractions are given in Table 6. The pick-up ratio is plotted as a function of oxide thickness in Figure 7. No systematic differences between the pick-up ratios in different regions of the fuel rods (plenum region, spacer region, span region) were noted, nor were there significant differences between the through-wall Zircaloy-4 and the liner Zircaloy-4 cladding. At lower oxide thickness values, the pick-up ratio was higher than at higher oxide thickness values. The very high value observed near one of the spacer regions (Rod 4) may be due to a faulty measurement (perhaps moisture in the oxide) or could be due to migration of hydrogen to the cooler spacer region. The latter would result in a high apparent pick-up ratio.

Table 6 Hydrogen Concentration and Pick-up Fraction

	Hydrogen Concentration* (ppm)			Pick-up Fraction**		
Rod	Plenum	Spacer	Span	Plenum	Spacer	Span
2	105	162	290	0.213	0.275	0.181
3	103	127	186	0.230	0.244	0.125
4	120	385	210	0.185	0.512	0.135
5	68	70	138	0.198	0.137	0.207
6	116	190	135	0.243	0.310	0.149

* Includes 10-15 ppm hydrogen initially present in the cladding.

** Corrected for initial hydrogen in the cladding; assumes Pilling-Bedworth ratio of 1.75.

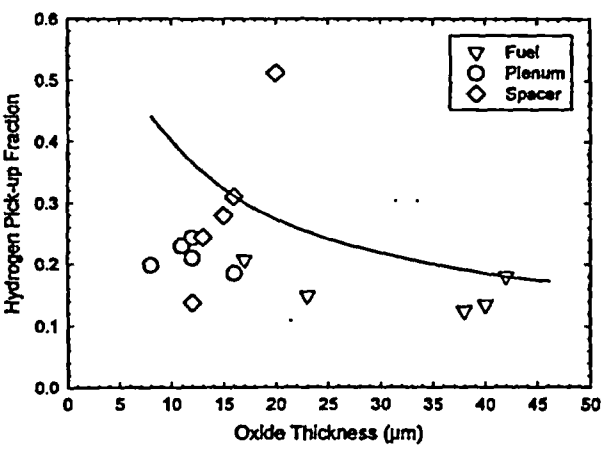

Figure 7 Hydrogen Pick-up Fraction as a Function of Oxide Thickness

D. Hydrogen/Hydride Distribution

Fuel rods were sectioned in the transverse and longitudinal directions. Metallographic specimens were polished and etched to reveal the zirconium hydrides. Representative photographs are shown in Figure 8.

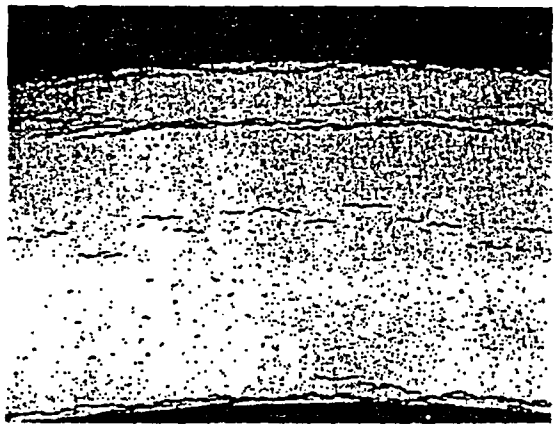

8a Through-Wall Zircaloy-4 Cladding (100X)

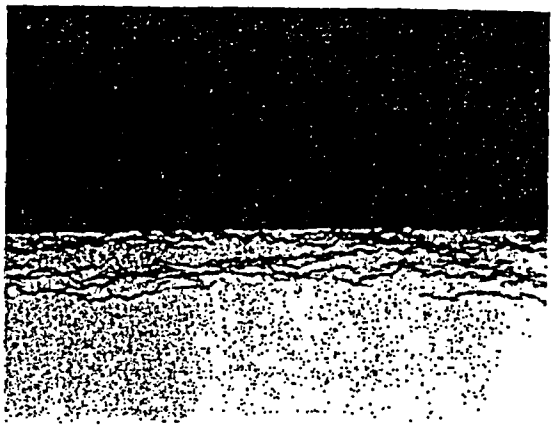

8b Outside Surface of Through-Wall Zircaloy-4 Cladding; Oxide Thickness: 42 μm (500X)

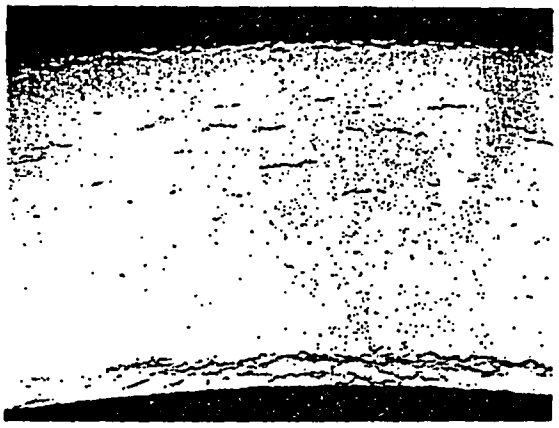

8c Zirconium Liner-Zircaloy-4 Cladding (100X)

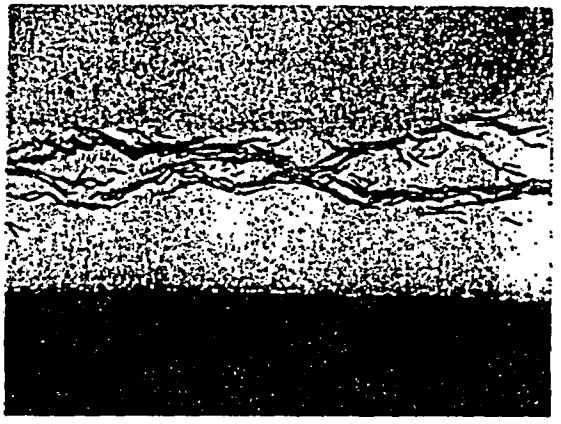

8d Inside Surface of Liner Zircaloy-4 Cladding; Liner Thickness: ~75 μm (500X)

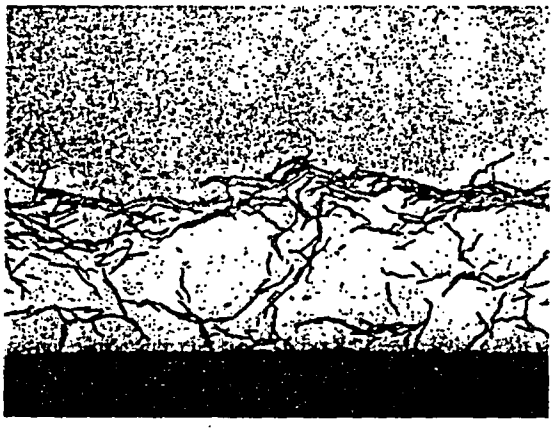

8e Inside Surface of Liner Zircaloy-4 Cladding; (500X)

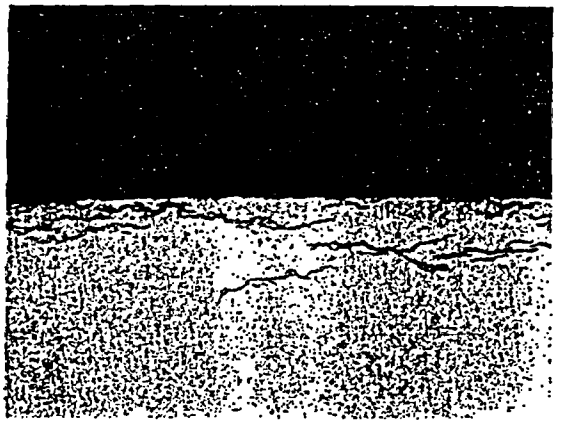

8f Outside Surface of Liner Zircaloy-4 Cladding; Oxide Thickness: 23 μm (500X)

Figure 8 Distribution of Hydrides in Zircaloy-4 and Zirconium Liner-Zircaloy-4 Cladding after Five Cycles of Irradiation

The hydride platelets are oriented in the tangential (and axial) direction of the cladding. This is shown for five-cycle through-wall cladding in Figure 8a. Figure 8b, at higher magnification, shows the hydrides in the vicinity of the cladding OD, where the hydride concentration is highest. Few of the hydrides are at the surface of the metal or appear to penetrate the surface. It appears unlikely that zirconium hydride near the cladding OD (shown in Figure 8b) could have been the cause of accelerated corrosion as observed in this specimen (oxide thickness 42 microns). Figures 8c through 8f show the distribution of hydrides in five-cycle irradiated liner cladding. The bulk of the Zircaloy-4 part of the liner cladding contains few hydrides. The total amount of hydrogen in the sample is approximately 135 ppm. In the liner cladding, the bulk of the hydrides precipitated in the zirconium liner close to, but not at, the interface with the Zircaloy. This is clearly shown in Figure 8d. In some cases, hydrides are present throughout the liner material and close to the ID. of the cladding. A representative view is shown in Figure 8e. There is a small concentration of hydride near the cladding OD, as shown in Figure 8f. These hydrides precipitated during fuel rod cool down.

The precipitation of hydrides in a temperature gradient in a cladding tube of uniform composition has been described by, among others, Asher and Trowse.[2] The zirconium hydrides precipitate preferentially near the relatively cooler cladding OD. At this location the concentration of hydrogen in solution is highest and the terminal solid solubility (t.s.s.) of hydrogen is lowest. Hydrides may precipitate at other locations away from the cladding OD due to other favorable conditions for precipitation.

The presence of zirconium liner at the cladding ID modifies the distribution of hydrogen and hydrides. The solubility of hydrogen in the lower-oxygen (400-600 ppm) zirconium liner is less than that in the higher-oxygen (1000-1400 ppm) Zircaloy.[3,4] At the prevailing temperatures and the small difference in oxygen concentration between Zircaloy-4 and liner, the difference is not large. The lower oxygen level in the liner compared to Zircaloy affects the terminal solid solubility more strongly. The terminal solid solubility of hydrogen in zirconium in Zircaloy-4 has recently been determined by Kodama and Anada[4] and earlier by Erickson and Hardie.[5] Kodama et al. found that upon cooling hydrogen-charged samples, when non-equilibrium gamma-phase hydride is formed, the t.s.s. in zirconium is lower than the t.s.s. in Zircaloy. At a temperature of approximately 350°C this difference is some 100 ppm. Upon heating, and the formation of stable delta-phase, the difference is smaller, probably on the order of 50 ppm at a temperature of approximately 350°C. This is also the temperature of the Zircaloy-zirconium interface temperature at an LHGR of approximately 6 kW/ft (~200 W/cm). At modest heat ratings, and hence moderate temperature gradients through the cladding wall thickness, zirconium hydride precipitates would, therefore, be expected to form in the liner near the Zircaloy-zirconium interface. This was observed in the fuel cladding examined here, and is schematically indicated in Figure 9a. At much higher heat ratings, and steeper temperature gradients, hydrides would be expected to precipitate near the cladding OD as is normally observed in single-composition through-wall cladding, and as indicated in Figure 9b.

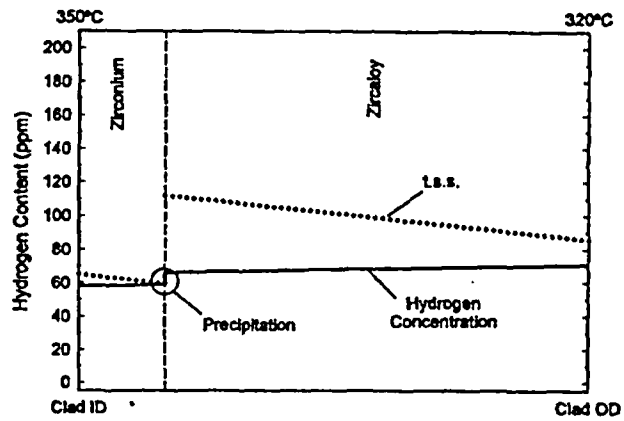

Figure 9a Schematic Illustration of Hydride Precipitation in the Liner at Moderate Heat Rating

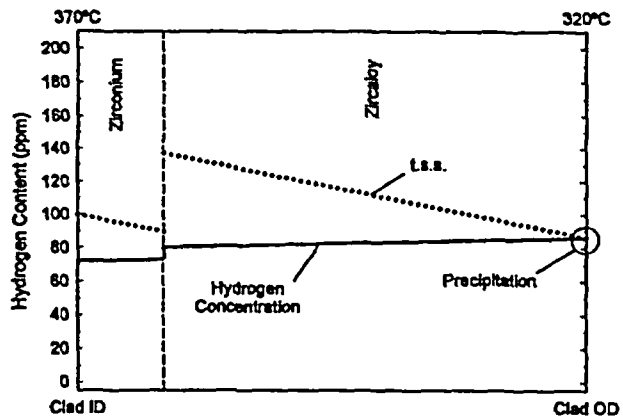

Figure 9b Schematic Illustration of Hydride Precipitation Near the Cladding OD at High Heat Rating and a Steep Temperature Gradient in the Cladding

The formation of a high concentration of hydrides in the liner could be expected to affect the effectiveness of the liner in preventing PCI failures. The tendency of hydrides to form in the liner rather than in the Zircaloy

part of the cladding may also play a role in secondary failure mechanisms and the formation of long cladding splits. The formation of hydrides near the cladding ID would, due to the volume increase, set up a tangential stress in the Zircaloy part of the cladding, which could lead to or aid in the formation of cracks.

E. Tensile Tests

Tensile tests at room temperature (RT) and at 350°C were performed on 5 mm wide rings cut from the plenum and fueled sections of the fuel rods. D-shaped specimen "grips" were used to load the rings in the circumferential direction. Due to the specimen width (5 mm) to gage length (~1-2 mm) ratio, quasi-plane strain conditions prevailed in the test section.

Unirradiated ring type specimens and conventional hourglass specimens (axial direction) were tested at room temperature. The values for ultimate tensile strength (u.t.s), uniform elongation (ε_u), and total elongation (ε_t) for the two types of specimens were compared. Hourglass specimens showed a higher u.t.s value (740 compared to 685 MPa) and a higher ε_u value (8% compared to approximately 4-6%) than the ring specimens. ε_t was approximately the same for both types of specimens. These differences are mainly due to the different test direction (axial versus circumferential) and the effects of texture.

Table 7 provides an overview of the data obtained along with a listing of the specimen oxide thickness and approximate hydrogen content. The difference in u.t.s. between through-wall cladding and liner cladding, which was approximately 50 MPa in the unirradiated condition of both RT and 350°C, was maintained for specimens from the plenum sections (low hydrogen concentration) of the rods but was largely absent for specimens from the fueled sections (higher hydrogen concentration in the through-wall cladding).

At room temperature, the u.t.s. increased by 180-200 MPa for four-cycle rods and 220-250 MPa for five-cycle rods for both types of cladding. At 350°C, the u.t.s. increased approximately 200-230 MPa for both four- and five-cycle rods of both cladding types. These increases appear to be mainly the result of irradiation hardening.

Table 7 Results of Ring Tensile Tests

Clad Type	Fluence 10^{25} n/m² E>1 MeV	Oxide μm	H_2 ppm	Room Temperature u.t.s.	ε_u	ε_t	350°C u.t.s.	ε_u	ε_t
Zry-4	0	0	11	710	5	25	417	4.5	24
Liner	0	0	13	660	4	27	376	4.5	30
Zry-4	7	14	104	910	1.5	1.5	666	4	21
Zry-4	7	36	186	883	2	2	611	4	5
Liner	7	7	68	857	5	15	591	4	19
Liner	7	16	138	840	6	12	586	4	19
Zry-4	8.9	13	105	956	4	6	652	4	17
Zry-4	8.9	40	290	775*	2	2	602	3	8
Liner	8.9	11	116	911	4	10	614	4	18
Liner	8.9	22	135	878	5	12	598	4	19

* Fractured before u.t.s. was reached.

Uniform elongation (plastic deformation at maximum specimen load) was affected by irradiation and hydrogen pick-up, but the effects appeared to be relatively small. At room temperature, it remained constant at about 5% (before and after irradiation) for the liner cladding (bulk of cladding free of hydrides) and was reduced from 5% to 2-4% for the through-wall cladding. At 350°C, the uniform elongation of all specimens went from 4.5% before irradiation to 4% after irradiation.

The most notable differences were observed in the values for total elongation. For through-wall cladding with high concentrations of hydrides, the total elongation decreased from 25% before irradiation to 2-4% after irradiation when tested at RT, and from 24% to 5-8% when tested at 350°C. At low hydrogen values the decrease in total elongation, when tested at 350°C, was much less pronounced: 24% before irradiation compared to 17-21% after irradiation. For liner cladding specimens with an absence of hydrides in the Zircaloy-4 part of the cladding, total elongation reductions were much smaller than those observed for through-wall cladding with hydrides. At RT, total elongation in the liner specimens was still 10-15% (27% before irradiation). At 350°C, the total elongation was 18-19% for the irradiated material, compared to 30% for the unirradiated cladding.

In summary, it may be concluded that the u.t.s. of the stress-relieved cladding, when tested in the circumferential direction, is increased mainly due to irradiation hardening; the total elongation, as measured in the ring type specimens, is decreased mainly due to the presence of hydrides. The uniform elongation was not strongly affected by either irradiation or hydrides.

V. CONCLUSIONS

Poolside and hot cell examinations of through-wall 1.5% Sn Zircaloy-4 cladding and zirconium liner-Zircaloy-4 cladding have led to the following conclusions:

The initial corrosion rate of the through-wall Zircaloy-4 cladding (~1.5% Sn) irradiated during the program appears to be higher than the corrosion rate of liner Zircaloy-4 cladding. The through-wall cladding also appears to be more susceptible to accelerated corrosion at high burnup than the liner cladding. Small differences in composition and/or fabrication processing or differences in hydrogen pick-up and hydride distribution could be possible causes.

The density of the oxide formed on the fuel rod cladding is approximately 89-90% of the theoretical density of zirconium oxide.

Hydrogen pick-up ratios for both types of cladding were similar. The pick-up ratio is found to be higher at low oxide thickness and approaches approximately 15% at an oxide thickness of 50 microns.

Hydrides preferentially precipitate near the cooler cladding outside surface in single-composition through-wall Zircaloy-4 cladding. In the pure zirconium liner-Zircaloy-4 cladding, hydrides accumulate in the liner.

The tensile strength of fuel rod cladding is increased due to irradiation, and total elongation at fracture is decreased, mainly due to hydrides that are present in the matrix. The uniform elongation was not as strongly affected by irradiation and hydride precipitation as the total elongation. The liner cladding maintained a high degree of ductility at room temperature due to the absence of hydrides in the Zircaloy-4 part of the cladding.

ACKNOWLEDGMENTS

The authors are grateful to ESEERCo, RG&E, and Siemens for permission to publish this paper. They are also indebted to Mr. C. Lemaignan and Mr. R. Gillet of the CEA laboratories in Grenoble, France for ably guiding all hot cell activities and to the hot cell laboratory personnel for performing the examinations.

REFERENCES

1. SCDAP/RELAPS/MOD 3.1 Code Manual Volume IV: MATPRO, P. T. Hagrman, editor, NUREG/CR-6150, EGG-2720.

2. R. C. Asher and F. W. Trowse, "The Distribution of Hydrogen in Zirconium Alloy Fuel Cladding: The Effects of Heat Flux," *Journal of Nuclear Materials*, 35 (1970), p. 115-121.

3. S. Yamanaka, T. Tanaka, M. Miyake, "Effect of Oxygen on Hydrogen Solubility in Zirconium," *Journal of Nuclear Materials*, 167 (1989), p. 231-237.

4. T. Kodama, H. Anada, "Study of Inhomogeneous Distribution of Hydrides in Zirc Liner Tubing," *Japanese Nuclear Society Proceedings*, October 23-26, 1984.

5. W. H Erickson and D. Hardie, "The Influence of Allowing Elements of the Terminal Solubility of Hydrogen in α-Zirconium," *Journal of Nuclear Materials*, 13 No. 2 (1964), p. 254.